INFN Istituto Nazionale di Fisica Nucleare
LABORATORI NAZIONALI DI FRASCATI
SIS – Pubblicazioni

LNF–07/17 (Thesis)
September 17, 2007

Sapienza Università di Roma

Scuola di Ingegneria Aerospaziale

Tesi di laurea specialistica in Ingeneria Astronautica

OPTICAL CHARACTERIZATION OF LARES CUBE CORNER REFLECTORS

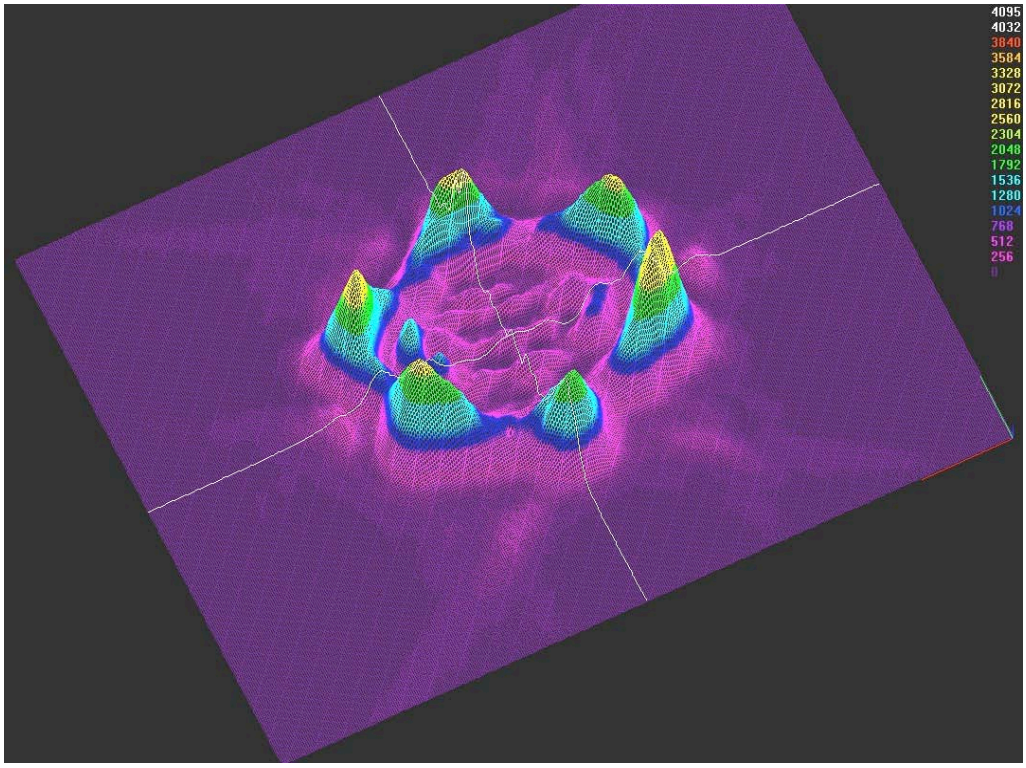

Thesis Advisor
Prof. Antonio Paolozzi

Graduate
Alessandro Lucantoni

Thesis Co-advisor
Dr. Simone Dell'Agnello

Academic Year 2006/2007

Optical Characterization of LARES Cube Corner Reflectors

Candidate: Alessandro Lucantoni
Advisor: Prof. Antonio Paolozzi
Co-advisor: Dr. Simone Dell'Agnello

1 The LARES space mission

1.1 The LAGEOS Satellite

LAGEOS (Laser Geodynamics Satellite), developed by NASA, was launched in 1976 with a Delta-2 rocket, while LAGEOS II, built by ASI (see Figure1.1), was launched in 1992 with the Space Shuttle.

LAGEOS is a passive satellite. It carries no electronic equipment or moving parts. Mounted on the spherical satellite are 426 corner cube reflectors (CCR) that give LAGEOS its golf ball-appearance. The CCR carried by LAGEOS are three-dimensional prisms that reflect light back to its source regardless of the angle the light is received by the satellite. The aim of the two LAGEOS satellite is to measure the "frame dragging" which should cause for a satellite with an orbital semi-major axis of 12000 km, like LAGEOS, a tiny shift of its node of about 33 milliarcsec in a year, that is nearly 1.9 m a year [1].

Figure 1.1 -The LAGEOS II satellite, built in Italy in the early 1990's-

Using the technique of laser ranging with CCRs to send back the short laser pulses, it is possible to measure distances to a point of the moon with a precision of few centimeters, and distances to a small artificial satellite with a precision of a few millimeters. Furthermore, the instantaneous

position of the two satellites can be measured with a precision of few millimeters and their orbits, with semi-major axes of 12270 km for LAGEOS and 12210 km for LAGEOS II, can be predicted, over 15 day periods, with a root mean-square-error of a few centimeters. The Lense-Thirring (LT) effect has been measured for the first time in 1998 [2] and the value obtained was in agreement with general relativity, with an error much larger than the laser ranging resolution, arising from:

- the deviation of the geo-potential from the perfect 1/r behaviour;
- the following non gravitational perturbations (NGPs): the thermal thrusts (TTs) due to solar radiation pressure, the Earth albedo and the Earth infrared radiation.

In year 2004 the preliminary 2002 EGM from GRACE data and a re-analysis of 11 years of LAGEOS and LAGEOS II data [3], see fig 1.2, allowed a decrease of the LT uncertainty to 10% (including also underestimated and unknown sources of error) [4]. This is to be compared to the uncertainty of the 1998 result, based on older geo-potential models, which is generally considered to be in the range 20-40%.

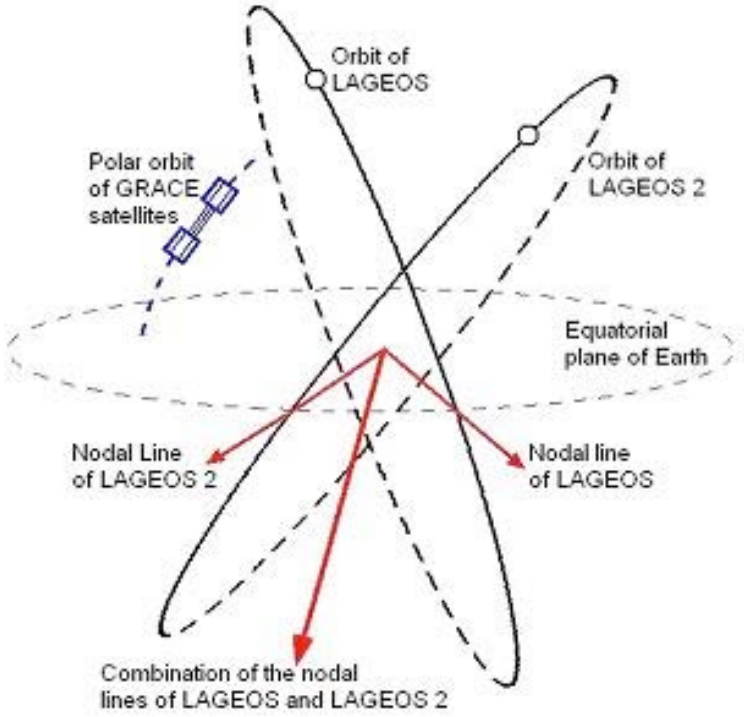

Figure 1.2 -The two LAGEOS and the two GRACE satellites-

1.1.1 Mechanical Structure

The LAGEOS spacecraft structure is the sphere formed from two separate aluminium hemispherical pieces which meet at the LAGEOS equatorial plane. The hemispheres surround a cylindrical

beryllium-copper core with little space between components; this gives a spacecraft interior filled with solid material to minimize the area-to-mass ratio. The core cylindrical axis is coincident with the polar axis. Each hemisphere contains 213 CCRs embedded in the surface.

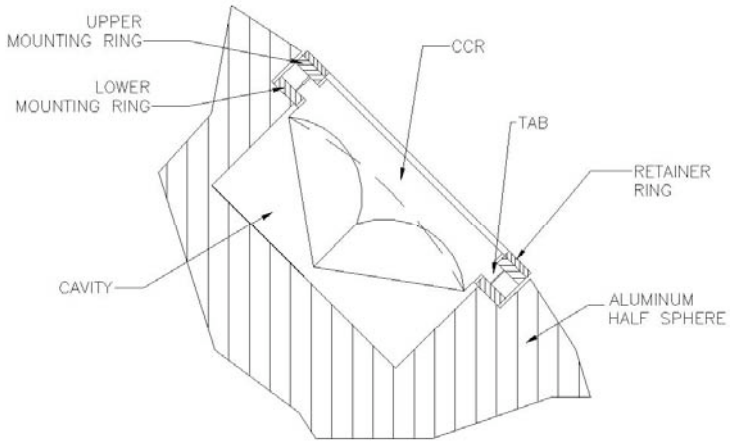

Figure 1.3 -CCR assembly-

422 CCRs are made of fused silica and four are made of germanium. Each CCR is held by a ring assembly within a cylindrical cavity bored radially into the hemisphere. Two mounting rings machined from clear, transparent KEL-F fluoroplastic encircle the CCR. An aluminium retainer ring on the top of the upper mounting rings covers the open space between the cavity wall and the CCR and shields the plastic mounting rings from direct outside radiation (see fig.1.3). Three Al machined screws pass through holes in all the three rings to press the ring assembly against the Al shoulder of the cavity.

1.1.2 The "International Laser Ranging Service"

The satellite laser ranging (SLR) experiments, like LAGEOS, carry on board numerous CCRs which are used for tracking (ranging) their position along their orbits. CCRs are special mirrors which, in an angle range, reflect an incoming light beam back in the direction it came from. The satellite ranging is achieved by shining from Earth multiple laser beams (each associated with a telescope for aiming at the satellite) managed by the International Laser Ranging Service (ILRS). The reflected laser beam is also observed with a telescope, providing a measurement of the round trip distance between Earth and the satellite. A number of ranging experiments during the past three decades have provided important geodesy measurements, including the Earth Gravity Model (EGM) and its time variations.

The ancestor of the SLR technique was the Lunar Ranging Retro Reflector (LRRR) experiment deployed by the Apollo 11, 14 and 15 missions to the moon. This is the only Apollo experiment that is still returning data from the moon. The laser beam has a 7 km diameter when it reaches the moon and about 20 km back to the Earth. The moon distance has been determined with an accuracy of 3 cm (the average distance is 384400 km).

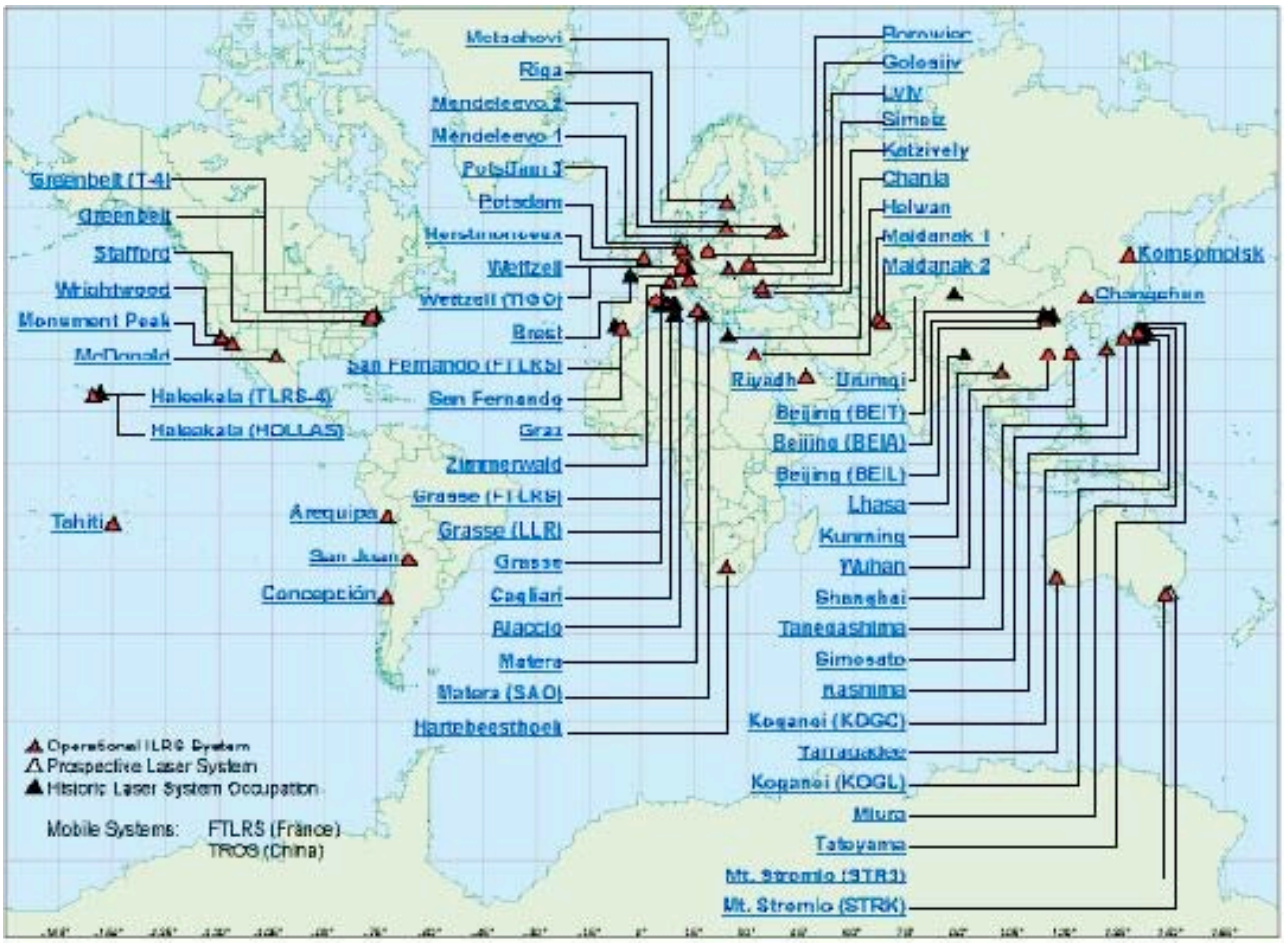

Figure 1.4 – ILRS stations –

Fig.1.4 shows the ILRS stations on the Earth surface.

1.1.3 Measurements of Space Geodesy

SLR has been until recently the most important tracking data type for the mapping of the terrestrial gravity field with space techniques. SLR data are not only of high quality and unambiguous nature, they are also highly sensitive to any change in the location of mass of Earth and orientation of the terrestrial figure axis, as well as the positions and motions of the tracking sites. These unique attributes make SRL the clear choice for systems that provides the reference frame information within the gravity model solutions.

The recent increase of interest in the climate change processes on Earth has highlighted the unique contribution of SRL targets, and in particular of the two LAGEOS' in that area: the determination

of tiny variations in the very-very low multipoles of the terrestrial gravity field. These variations are directly related to mass redistribution in the terrestrial system (land, oceans, atmosphere). The international geophysical community has identified that as one of the present research areas of utmost importance. The media coverage of the worldwide devastation caused by El Nino underlined its importance to all and resulted in an unprecedented increase in public awareness of the problem as well as the efforts to better understand it and forecast it in the future. To better accomplish that, the international community is continuously striving to improve both the space segment as well as the ground segment of systems observing global climate change. Some of the most important "weapons" are the recently launched dedicated gravity mapping CHAMP and GRACE. They have already delivered new global models for the gravitational field of Earth with unprecedented accuracy. Grace in particular, is now delivering multiple models covering monthly periods with half wavelength of about 250 km. This therefore has in part launched the era of temporal gravity monitoring at a previously unheard-of spatio-temporal resolution.

The data collected from LAGEOS and LAGEOS II with the laser ranging technique need to be processed. First, the orbit position and speed $\{x.y,z,\dot{x},\dot{y},\dot{z}\}$ as function of time is determined. This task is accomplished using a software called GEODYN II, developed at NASA Goddard Space Flight Center in the past 30 years. The software allows fitting the range data with a suitable set of models, accounting for the various forces acting on the satellite, together with all the information useful for correct data processing (such as a model for atmospheric delay of laser pulses). During the fitting procedure, it is usually necessary to estimate a number of parameters in order to achieve the best accuracy possible. The process of extracting the set {state vectors, other parameters} is called data reduction. This is done by GEODYN for each arc (and analysis period), employing a numerical integration of the orbit and consequent adjusting of related parameters. The complexity inherent in the accurate description of satellite's orbit requires the use of numerical models to take into account the following physics contributions:

- Gravitational perturbations (geo-potential, tides, De Sitter effect);
- Non gravitational perturbations;
- Reference frame;
- Observation conditions and corrections.

Each of the previous points specializes into a number of separate models and parameter specifications.

1.2 Measurement of the Lense-Thirring Effect

This is the precession of the satellite orbit due to the rotation of the central attracting body, Earth, which drags the space-time around with it. This effect is different from General Relativity (GR, 1916) phenomena like the precession of Mercury's orbit around the Sun or the deflection of the path of photons passing nearby the Sun, which are due to the presence of a large static mass, which curves the space-time. On the contrary, the Earth angular momentum generates additional space-time curvature and "drags" around nearby gyroscopes (spins) and satellite orbits (orbital angular momentum). If the angular momentum of Earth (J_{Earth}) were zero, than no frame dragging would be observed. The Lense-Thirring rate for the node orbital element, Ω , is:

$$\dot{\Omega} = \frac{2G\,J_{Earth}}{c^2 a^3 (1-e^2)^{3/2}}$$

where, G is the gravitational constant, "a" and "e" are the orbit semi-major axis and eccentricity; the node is the intersection of the Earth's equatorial plane with the satellite's orbit.

The amount of this precession is tiny: about 2 meters per year (33 milliarcsec/year) for the semi-major axis of 12000 Km of the LAGEOS satellites. This value is more than a factor of ten smaller than the precession of Mercury's perihelion, which is 430 milliarcsec/year. The Lense-Thirring effect is formally similar to the precession induced by a central sphere of rotating electric charge on a discrete dipole moment or on the dipole moment of a closed electric current loop. For this reason, it is also referred to as "gravitomagnetism".

Einstein's general theory of relativity predicts the occurrence of peculiar phenomena in the vicinity of a spinning body, caused by its rotation. When a clock that co-rotates very slowly around a spinning body returns to its starting point, it finds itself advanced relative to a clock kept there at rest (with respect to a distant star).

In fact, synchronization of clocks all around a closed path near a spinning body is not possible, and light co-rotating around a spinning body will take less time to return to a fixed point than light rotating in the opposite direction. Similarly, the orbital period of a particle co-rotating around a spinning body would be longer than the orbital period of a particle counter-rotating on the same orbit. Furthermore, an orbiting particle around a spinning body will have its orbital plane "dragged" around the spinning body in the same sense of the rotation of the body, and small gyroscopes that determine the axes of a local, freely falling, inertial frame, will rotate with respect to "distant stars" because of the rotation of the body. This phenomenon, called "frame dragging", is also known as Lense-Thirring (LT) effect.

In GR, all these phenomena are the result of the rotation of the central mass. Until now two different methods have been planned to measure the Lense-Thirring effect according to the effect it has on gyroscopes and on orbital angular momentum.

Gravity Probe B (GP-B) [5] was developed by NASA and Stanford University and launched on April 20, 2004 after a few decades of planning (the total cost was several hundred million US$). It contains four, almost perfectly spherical, spinning gyroscopes suspended in a vacuum. Indeed according to Newtonian physics, a perfect gyroscope, which experiences no external forces will not drift. In GP-B this would mean that once a gyroscope is spinning in alignment with the guide star, it would stay aligned with that star forever. GP-B has been built to measure two distinct effects of general relativity.

The first, the geodesic effect, should cause the spin axis orientation of a gyroscope, cycling the Earth in a polar orbit, to change by a tiny angle of 6.6 arcsec (0.0018 degrees) in a year, relative to a distant guide star. The second effect, the LT, should cause the gyroscope axis to change orientation in the plane of Earth's rotation (orthogonal to the orbit plane) by a minuscule angle of 0.041 arcsec (0.000011 degrees) in a year. Conceptually the GPB experiment is quite simple. An optical telescope faithfully points to its guide star, 6th-magnitude IM Pegasi. Initially the gyroscopes spin axes are aligned through the bore side of the telescope to this guide star. A set of superconducting readout systems detect minute changes in each gyroscope's spin axis orientation. Changes in the spin axis alignment of the gyroscopes are a direct measurement of the geodetic and/or frame dragging effects of general relativity. GP-B gyroscopes limit any drift resulting from electrical and mechanical imperfection or forces acting on them. The GP-B instrument is designed to measure changes in gyroscopes spin axes orientation to better than 0.5 milliarcsec over a one year period.

1.2 New Mechanical Design of LARES

With its 30 centimeter diameter, 100 kg weight and 102 CCRs placed on the aluminum outer surface, LARES is a new generation satellite for a measurement of the Lense-Thirring effect within an error $\leq$ 1% (the same measurement with LAGEOS is 10 %).

In order to make such a precise measurement, two different approach have been developed. In a first approach, LARES has the same structure as the two LAGEOS satellites and the improvement in the measurement will be achieved by an accurate characterization of the spacecraft before the launch. The thermo-optical and the mechanical properties as well as their variation in space along the years will be input to Thermal Desktop [6], a specialized thermal software for satellites, and, ultimately also inserted into GEODYN to reduce associated errors. The main goal of this work is to

accurately estimate thermal thrusts (TTs) on the LARES satellite. Thermal trust results from an anisotropic emission of thermal radiation by the satellite surface: on LAGEOS, this arises from a non-uniform temperature distribution over the surface [7].

Also the surface-mass (S/M) ratio has been considered in the first approach: indeed this is the same for LARES (0.3m/100 kg) and LAGEOS (0.6m/400kg): the non-gravitational perturbation are proportional to this ratio.

In the second approach the main goal is to decrease the S/M ratio by making LARES a single sphere of tungsten alloy with a machined cavity to house the CCRs thanks to the high density of tungsten. For a diameter of 300 mm the weight is about 255 kg (vs. 100 kg using aluminum alloy).

We can see the CCR assembly and its mechanical design in the figure 1.5 and 1.6.

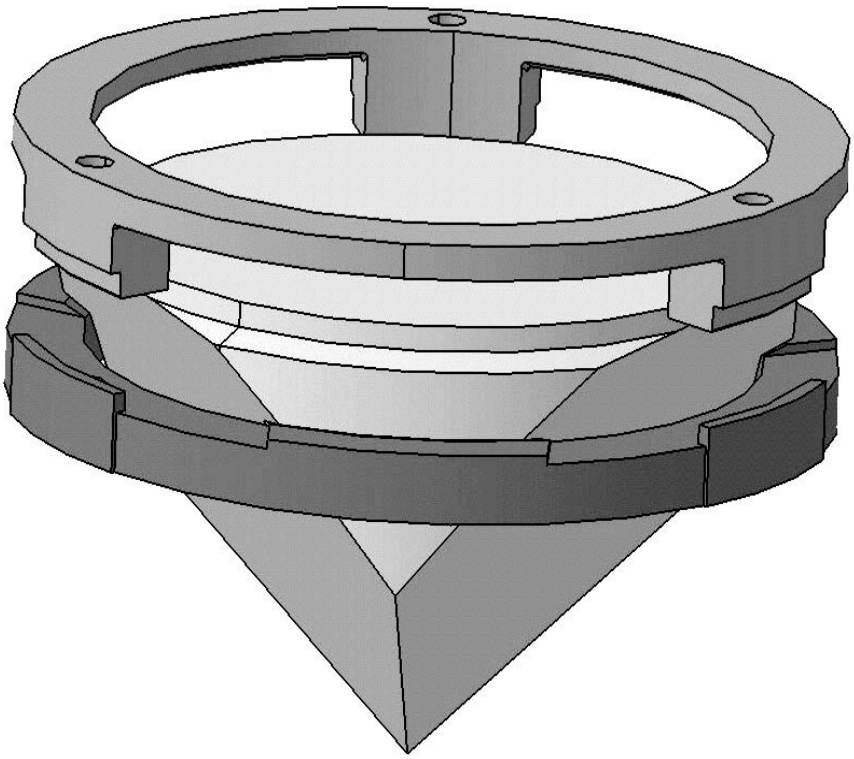

Figure 1.5 – LARES CCR assembly -

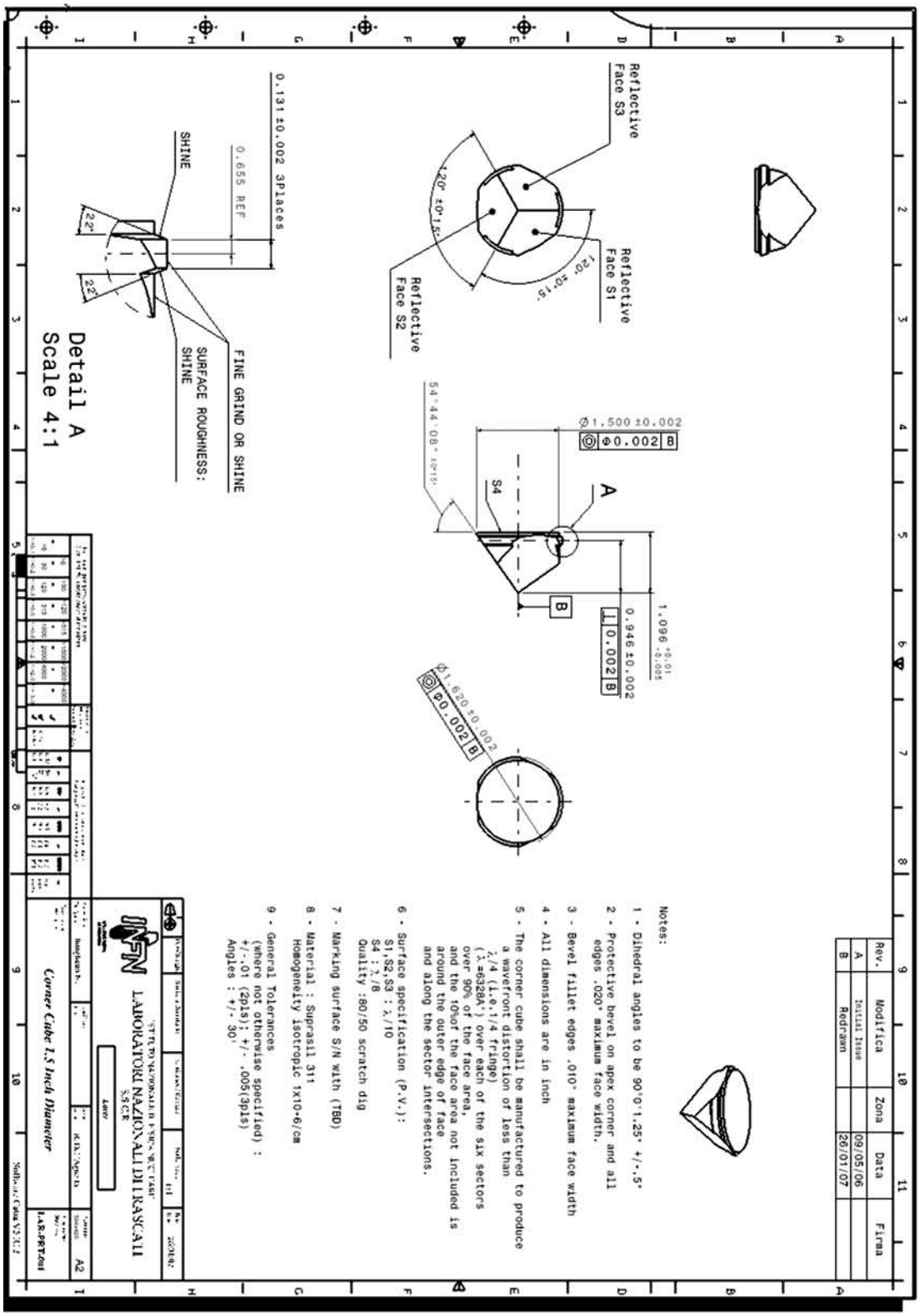

Figure 1.6 – LARES CCR mechanical design –

2 The LARES Retro-Reflectors

2.1 CCR Working Principle

The CCRs are special mirrors with the property of reflecting laser pulses in the same direction of the impinging light (only within an acceptance angle of about 30 degrees). They have to be manufactured very accurately in order to be able to reflect the laser pulses back to the station.
The retro-reflectors used for satellite laser ranging are generally around 1.5 inches in diameter. In LEO orbit, the diffraction pattern is too narrow to account for velocity aberration. In order to widen the pattern, dihedral angle offsets are used even if this creates a complicated lumpy diffraction pattern.
The width of the diffraction pattern is proportional to the wavelength divided by the diameter of the retro-reflector. For a perfect circular cube corner the position of the first zero in the diffraction pattern is:

$$\alpha = 1.22\frac{\lambda}{D}$$

where λ is the wavelength and D is the diameter of the cube corner.
An alternative to using dihedral angle offsets is to decrease the size of the cube corner. In order to maintain the same signal strength a larger number of retro-reflectors is needed. Since the cost per cube is about the same regardless of size this has a cost impact. The reason for using such large cubes in LEO appears to be financial (not technical) since smaller cubes are better in every way for LEO. Even if the working principle is the same, various retro-reflectors design exist each with its characteristics; for thermal reasons, uncoated cubes corners will be used (as LAGEOS).

Uncoated cubes with no dihedral angle offset

In an uncoated cube polarization effects due to total internal reflection create 6 spots around the central peak in a cube with no dihedral angle offset. These six peaks are smoother than the peaks created by using a dihedral angle offset. The size of the cube can be chosen to put the receiver on these six peaks. No dihedral angle offset is needed. The cubes can also be installed at 0 and 30 deg orientation to create a smoother ring. If there is no dihedral angle offset in an uncoated cube the diffraction pattern is nearly the same for circular and linear polarization. As mentioned this configuration raises the cost [8].

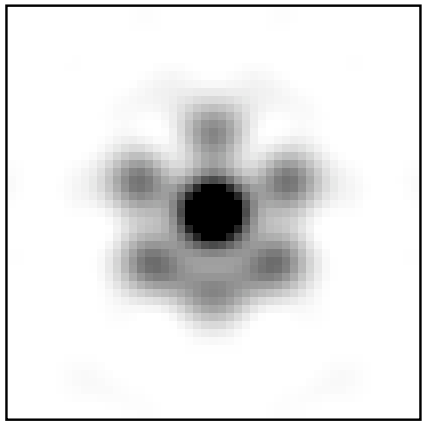

Figure 2.1 -No dihedral angle-

Uncoated cubes with dihedral angle offset

In an uncoated cube using a dihedral angle offset will not make the six spots any brighter. It is possible to put energy at a larger radius than the six spots, but the diffraction pattern becomes complicated and very lumpy. It will be different for each input polarization state.

For example if there is a dihedral angle offset in an uncoated cube and circular polarization is used there is no polarization bias since there is no preferred direction for the electric field [9].

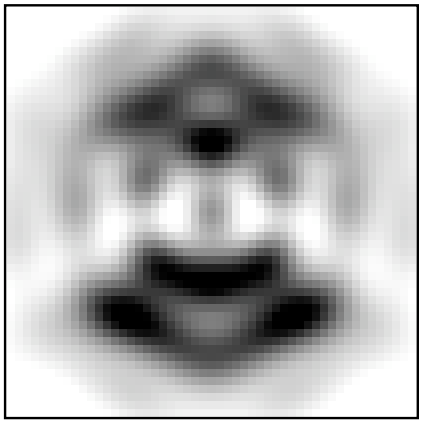

Figure 2.2 -Dihedral angle offset-

Dihedral angle offset

The dihedral angle offset is necessary so that part of the energy pattern is distributed in the area where the receiving station is present. Therefore the offset Dihedral angle depends on satellite speed and altitude.

The normal manufacturing accuracy of the dihedral angle offset in a retroreflector is about 0.5 arcsec. If the angle is specified as 1.5 arcsec +/- .5 arcsec, the angle can vary from 1.0 to 2.0 arcsec. This has a significant effect on the diffraction pattern. The spreading of the pattern is about the same for a positive and negative dihedral angle offset.

2.2 LASER

A laser is a device that emits light through a specific mechanism for which the term laser is an acronym: **l**ight **a**mplification by **s**timulated **e**mission of **r**adiation. This is a combined quantum-mechanical and thermodynamical process.

As a light source, a laser can have various properties, depending on the purpose for which it is designed. A typical laser emits light in a narrow and well defined beam and with a well defined wavelength (or color). This is in contrast to a light source such as the incandescent light bulb, which emits in almost all directions and over a wide spectrum of wavelength. These properties can be summarized in the term coherence.

Coherence is the property of wave like states that enables them to exhibit interference. It is also the parameter that quantifies the quality of the interference (also known as the degree of coherence). In interference, at least two electromagnetic wave are combined and, depending on the relative phase between them, they can add constructively or subtract destructively. The degree of coherence is equal to the interference visibility, a measure of how perfectly the waves can cancel due to destructive interference.

Light of a specific wavelength that passes through the gain medium is amplified (increases in intensity); the surrounding mirrors ensure that most of the light makes many passes through the gain medium. Part of the light that is between the mirrors (i.e., is in the cavity) passes through the partially transparent mirror and appears as a beam of light. The process of supplying the energy required for the amplification is called pumping and the energy is typically supplied as an electrical current or as light at a different wavelength. In the latter case, the light source can be a flash lamp or another laser. Most practical lasers contain additional elements that affect properties such as the wavelength of the emitted light and the shape of the beam. A helium-neon laser, usually called a

He/Ne laser, is a type of small gas laser. He/Ne lasers have many industrial and scientific uses, and are often used in laboratory demonstrations of optics. Its usual operation wavelength is 632.8 nm, in the red portion of the visible spectrum.

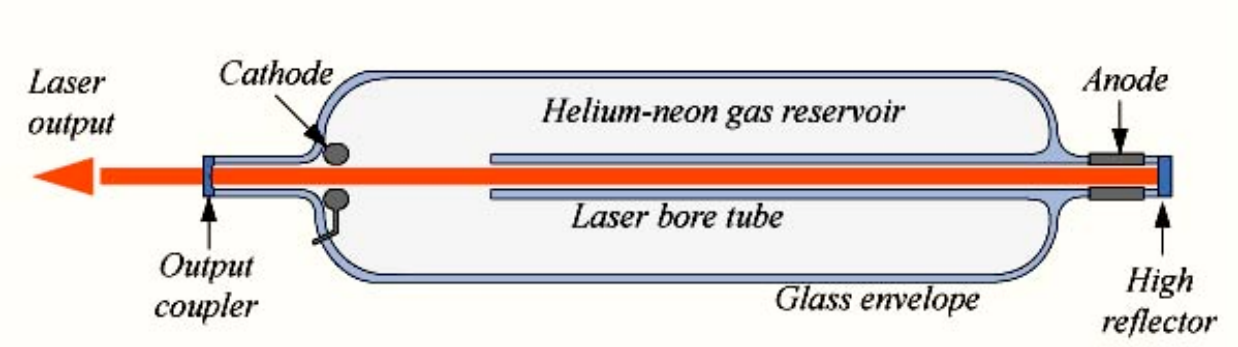

Figure 2.3 -schematic diagram of a He/Ne laser-

The gain medium of the laser, as suggested by its name, is a mixture of helium and neon gases, in a 5:1 to 20:1 ratio, contained at low pressure in a glass envelope. The energy or pump source of the laser is provided by an electrical discharge of around 1000 V through an anode and cathode at each end of the glass tube. A current of 5 to 100 mA is typical for CW operation. The optical cavity of the laser typically consists of a plane, high-reflecting mirror at one end of the laser tube, and a concave output coupler mirror of approximately 1% transmission at the other end.

He/Ne lasers are typically small, with cavity lengths of around 15 cm up to 50 cm, and optical output powers ranging from 1 mW to 100 mW. The red He/Ne laser wavelength is usually reported as 632nm. However, the true wavelength in air is 632.816 nm, so 633nm is actually closer to the true value.

2.2.1 Polarization

In electrodynamics, polarization is the property of electromagnetic waves, such as light, that describes the direction of the transverse electric field. More generally, the polarization of a transverse wave describes the direction of oscillation in the plane perpendicular to the direction of travel. Longitudinal waves such as sound waves do not exhibit polarization, because for these waves the direction of oscillation is along the direction of travel.

The simplest manifestation of polarization to visualize is that of a plane wave, which is a good approximation to most light waves (a plane wave is a wave with infinitely long and wide wave-fronts). All electromagnetic waves propagating in free space or in a uniform material of infinite extent have electric and magnetic fields perpendicular to the direction of propagation. Conventionally, when considering polarization, the electric field vector is described and the magnetic field is ignored since it is perpendicular to the electric field and proportional to it.

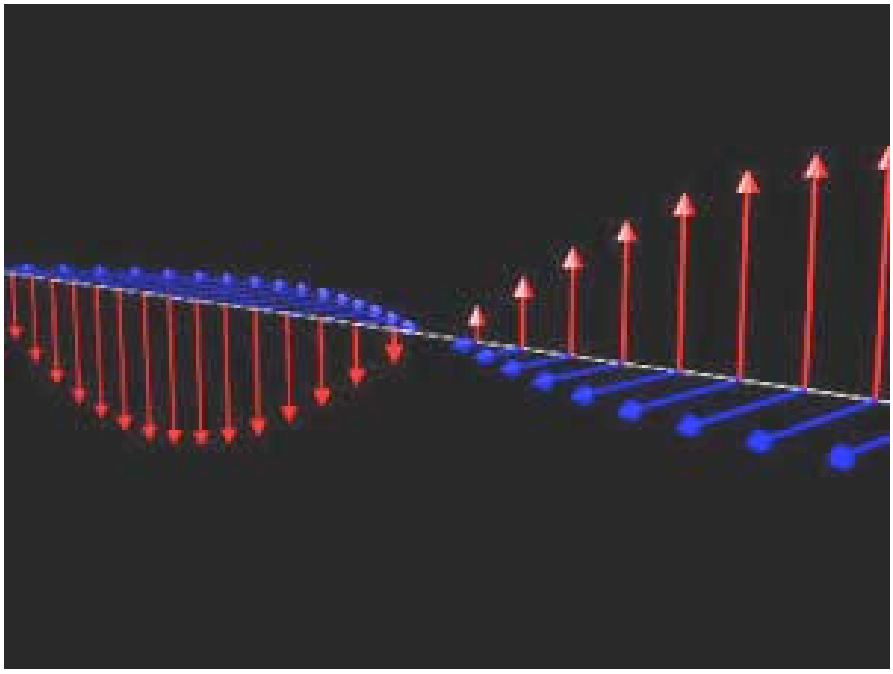

Figure 2.4 – Linear polarization.

The electric field vector may be arbitrarily divided into two perpendicular components labeled *x* and *y* (with z indicating the direction of travel). For a simple harmonic wave, where the amplitude of the electric vector varies in a sinusoidal manner, the two components have exactly the same frequency. The shape traced out in a fixed plane by the electric vector as such a plane wave passes over it, is a description of the polarization state. The following figures show some examples of the evolution of the electric field vector (blue) with time (the vertical axes), along with its *x* and *y* components (red/left and green/right), and the path traced by the tip of the vector in the plane (purple)[10]:

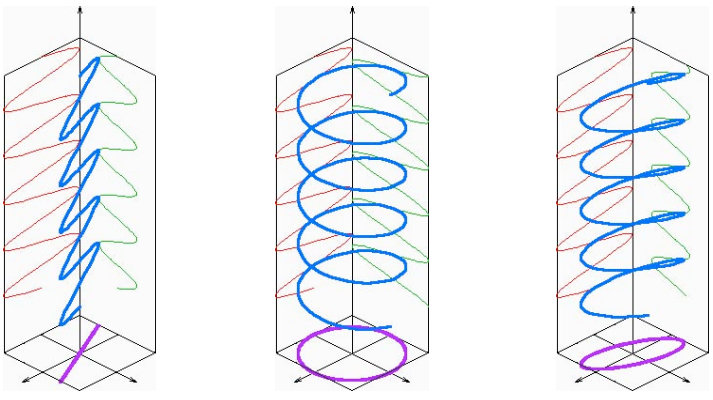

Linear circular elliptical

Figure 2.5 – Polarization state.

2.3 Satellite Velocity Aberration

In the inertial coordinate system of a retroreflector a beam of light entering the retroreflector will be returned along the same line that it entered. If there is a difference in velocity between the retroreflector and the transmitter, the beam will not be returned to the source (fig. 2.6). The analysis is easiest in the inertial coordinate system of the retro-reflector.

The usual situation is that the retroreflector is in orbit and the transmitter is on the ground. We will consider the retroreflector to be stationary and the transmitter to be moving at the velocity V_{rel}.

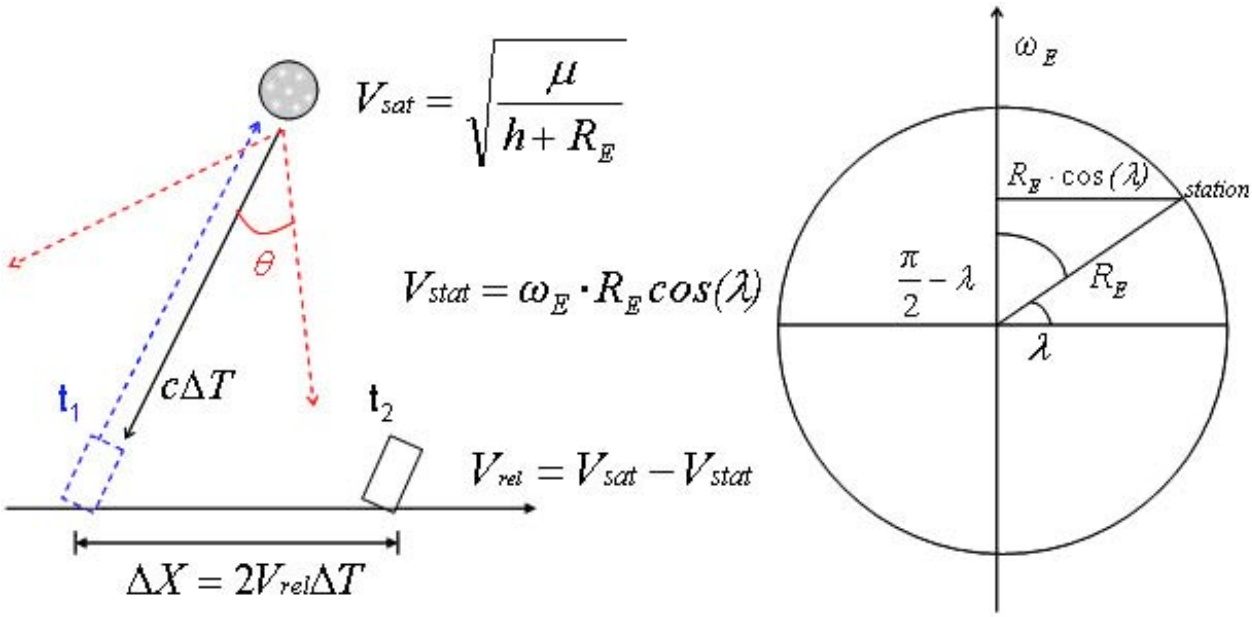

Figure 2.6 – Satellite and station movements -

In the diagram below (fig.2.7), a transmitter emits a pulse of light at point A which travels in time Δt at velocity *c* to a retroreflector. The center of the reflected beam returns to point A after another time interval Δt. In time 2Δt, the transmitter moving at velocity *v* at an angle ϕ from a line perpendicular to the line of sight moves to point B.

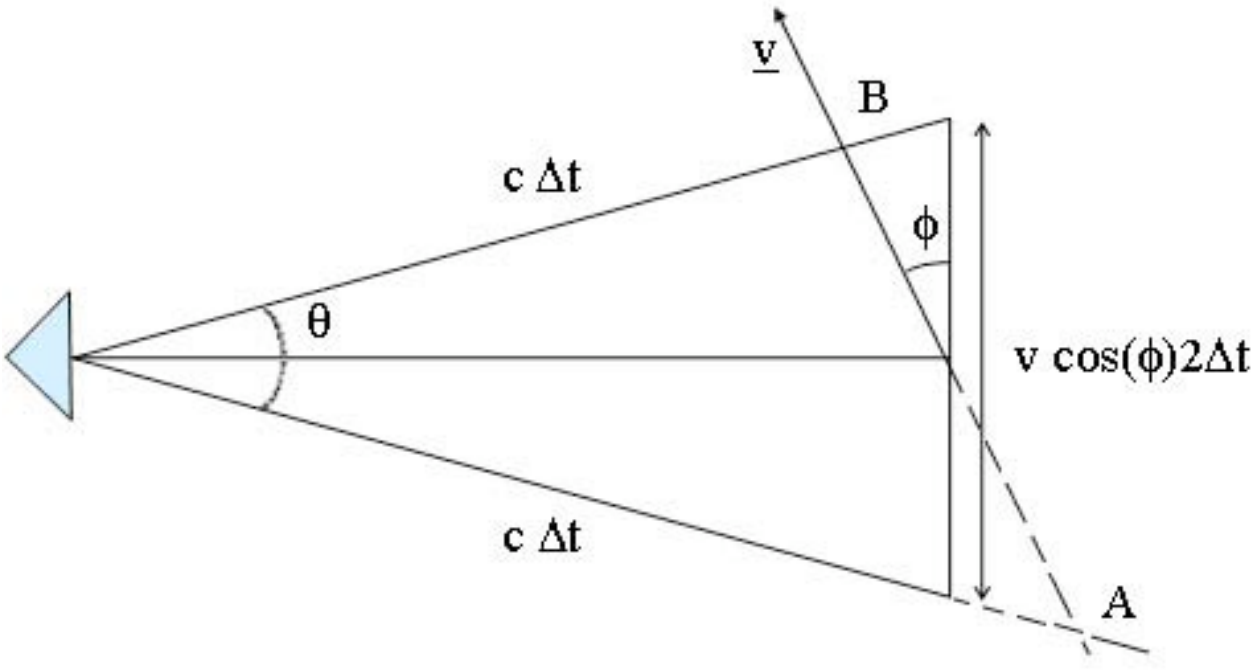

Figure 2.7 – Velocity aberration -

since $[\vartheta << 1]$ we have :

$$c \cdot \Delta t \cdot \vartheta \cong v \cdot \cos\phi \cdot 2\Delta t$$

$$\Rightarrow \vartheta = 2\frac{v}{c}\cos\phi$$

where

- v is the relative velocity between station and CCR
- ϑ is the velocity aberration.

In order for the transmitter to receive any of the reflected light at point B, the angular radius of the reflected beam must be at least equal to ϑ.

The velocity aberration is a function of satellite altitude and station latitude: in fact changing these two parameters, changes the relative velocity.

2.4 CCR "Far Field Diffraction Pattern" (FFDP)

In optics, the far field diffraction pattern or Fraunhofer diffraction (fig.2.8) is a form of wave diffraction, which occurs when field waves are passed through an aperture or slit.

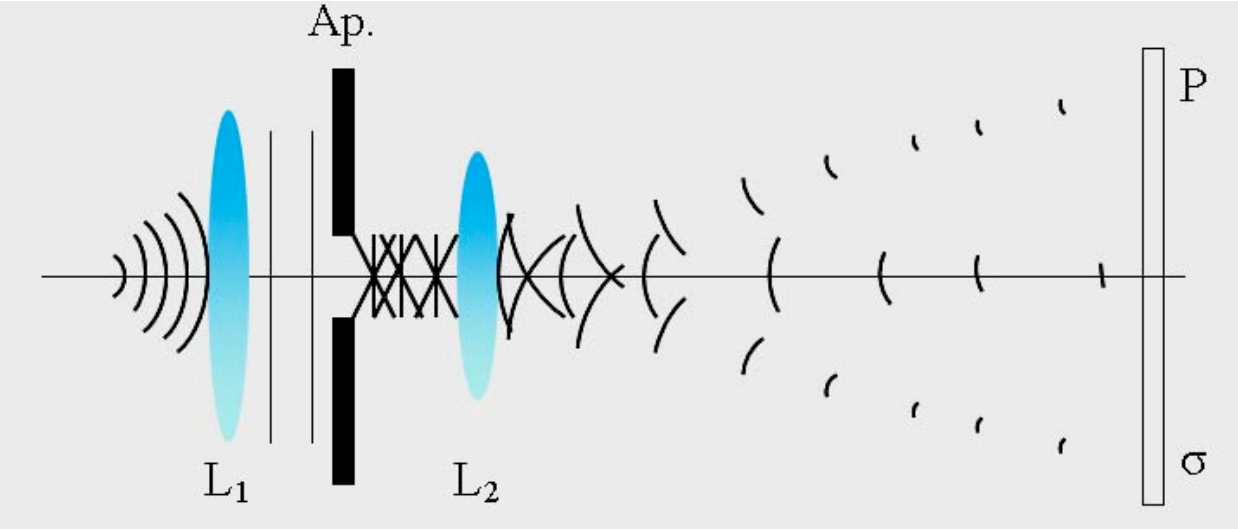

Figure 2.8 – Fraunhofer diffraction –

The far field begins at a distance, *z*, defined by

$$z = \frac{a_0{}^2}{\lambda}$$

where a_0 is the beam diameter at the exit aperture and λ is the wavelength of light emitted by the laser.

The laser beam diameter is commonly defined as the value at which the intensity has fallen to 13.5 % of its peak value (2σ). Applying this equation to an He/Ne laser emitting a 0.8 mm waist diameter beam at a wavelength of 633 nm, the far field begins at approximately 100 cm from the exit aperture.

The angular radius (or beam divergence angle), designated by θ (in radians), of a Gaussian beam in the far field is approximated by the expression**:**

$$\theta = \frac{\lambda}{\pi \cdot r_0}$$

where r_0 is the beam waist radius at the laser exit aperture.

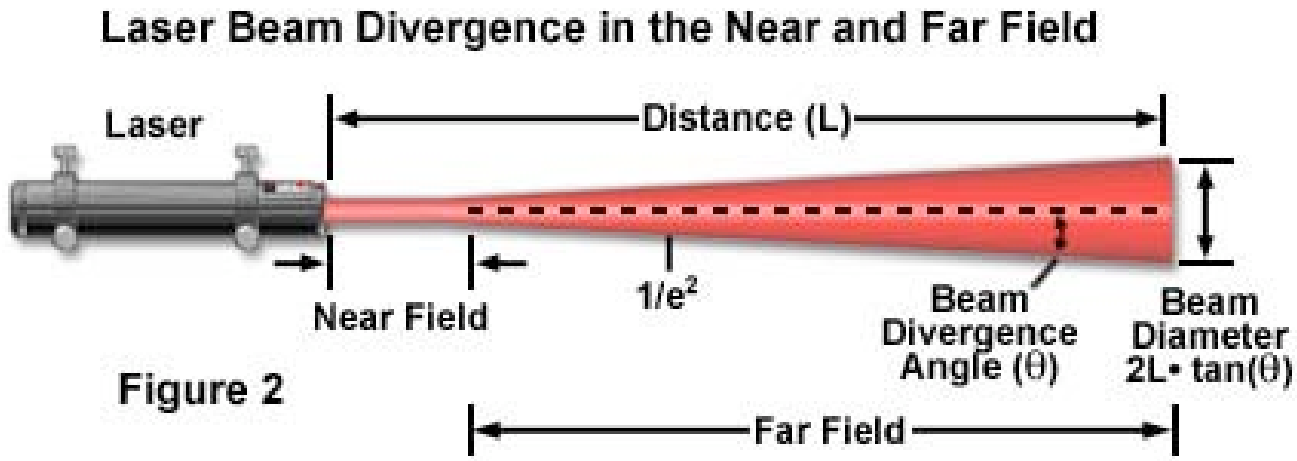

Figure 2.9 – Laser Divergence –

Also in this case, applying this equation to a He/Ne laser emitting a 0.4 mm waist diameter beam at a wavelength of 633 nm, the beam divergence is 500 μrad: since we have an expander / reducer system this high divergence is not important because with them, we make the beam collimated. In laser ranging, the laser used by station has a diameter about 200 mm and consequently the beam divergence is very low (2 μrad).

Fraunhofer diffraction goes from the idea of a wave being diffracted in to several outgoing waves when passed through an aperture, slit or opening, and is usually described through the use of observational experiments using lenses to purposefully diffract light. When waves pass through, the wave is split into two diffracted waves traveling at parallel angles to each other along with the continuing incoming wave, and are often used in methods of observation by placing a screen in its path in order to view the image-pattern observed.

In the CCR case FFDP the aperture is the circular clean aperture of the CCR. If this were a flat mirror we would have an Airy pattern (fig.2.10): indeed, the diffraction pattern resulting from a uniformly illuminated circular aperture, has a bright region in the center, known as the Airy disc which together with a series of concentric rings is called the Airy pattern (both named after George Airy). The diameter of this disc is related to the wavelength of the illuminating light and the size of the circular aperture [11]:

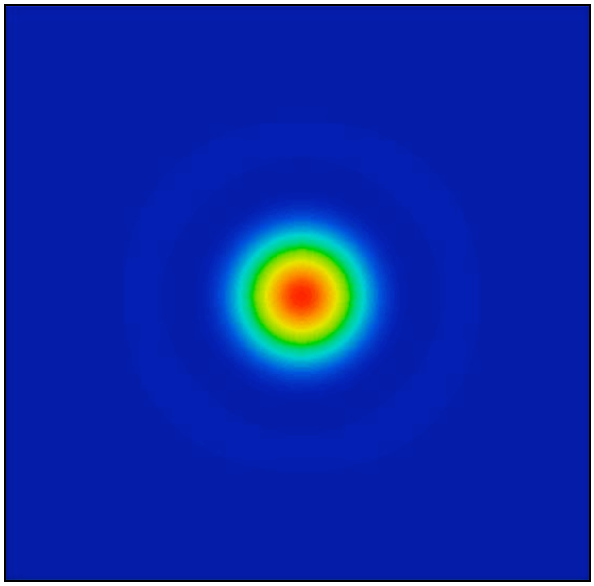

Figure 2.10 – Theoretical Airy pattern –

In the following figure (2.11) we see the Airy pattern obtained experimentally on the optical table using a mask, with a circular aperture, positioned over the flat mirror:

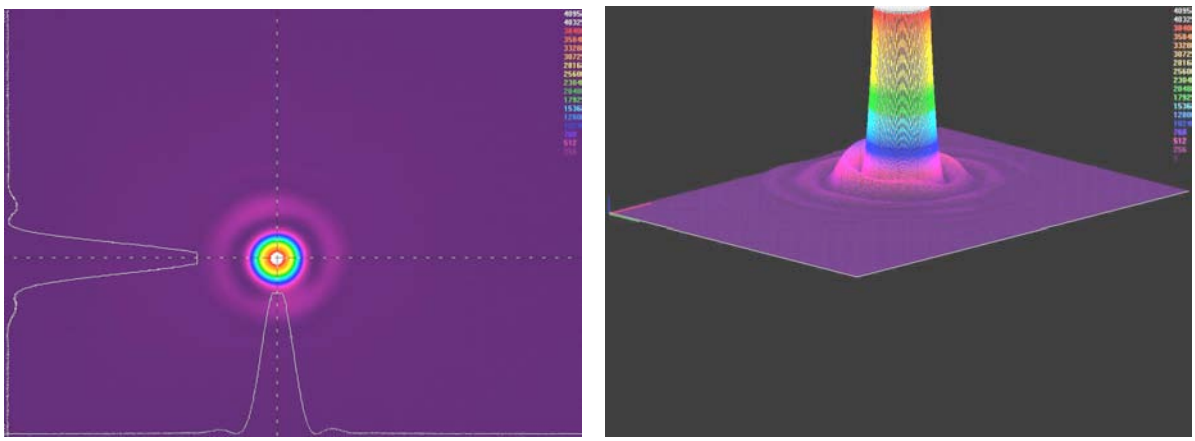

Figure 2.11 – Experimental Airy pattern –

Far away from the aperture, the angle at which the first minimum occurs, measured from the direction of incoming light, is given by:

$$\sin\theta = 1.22\frac{\lambda}{d}$$

where _ is the wavelength of the light and *d* is the diameter of the aperture.

Because we don't have a simple flat mirror but a CCR, the internal reflections make the interference pattern much more complicated: the FFDP figure for a CCR with dihedral angle offset has six main lobes as shown in the following experimental 3D figure (2.9):

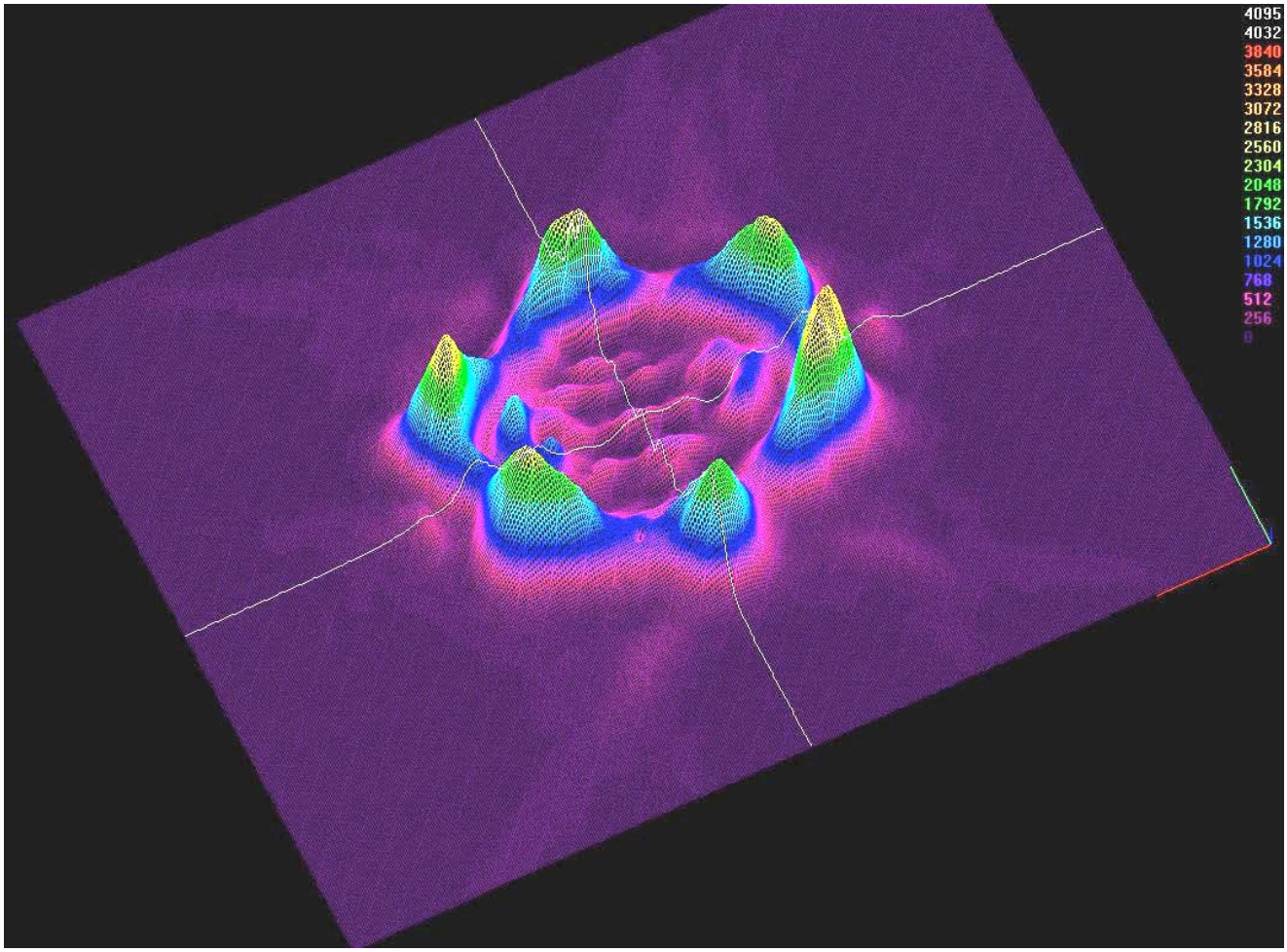

Figure 2.12 -3D FFDP of CCR-

Moreover, the shape of the FFDP is a strong function of the polarization state in an uncoated CCR.

2.5 LAGEOS Optical Design

Both LAGEOS and LAGEOS II have on their external surface (radius = 30 cm, weight = 411 kg) 426 retro-reflectors (422 quartz and 4 germanium for infrared laser). In figure 2.10 we see the LAGEOS cap we have at LNF.

During laser-ranging, on average, from 1.5 to 2 CCRs are active at a time to provide adequate signal. In fact if the laser hits a single retroreflector and considering even the velocity aberration (36 μrad) effect, the pattern would come back to the ground with an energy distribution that could not be seen by the receiver. The reason is that using a dihedral angle offset (1.25 arcsec) concentrates the energy of the pattern in a ring of radius 36 μrad.

Figure 2.13 – LAGEOS cap at LNF –

Loss of total internal reflection depends on the orientation of the cube corner, to avoid having all the cubes lose total internal reflection at the same time each cube is rotated 26° from the next cube corner.

2.5.1 Range Correction

The center of mass distance of spherical satellites such as LARES and LAGEOS is calculated as $\Delta T/2$ times the light speed (corrected for the atmosphere propagation) and adding RC, the "range correction". RC is a calibration constant that describes the distance between the satellite center of

mass and the effective retro-reflected beam surface. Therefore RC is the same order of magnitude as the LARES radius. Such effective surface is computed as a convolution of the CCR optical response with the detector response that measures the retro-reflected beam arrival and with the response of the electronics used to measure ΔT.

The RC for LAGEOS has been measured by NASA-Goddard Space Flight Center in 1975 (LAGEOS I) and 1992 (LAGEOS II) [12], in air and STP conditions (Standard Temperature and Pressure). The ILRS explicitly requires RC measurement.

In the future RC will be measured for LARES under realistic climatic conditions as regards vacuum, temperature and electromagnetic radiation: this has never been done before.

This measurement will be made with LARES inside the LNF Space Climatic Facility (SCF), including a certified solar simulator AM0 (Air Mass at zero pressure) and a Earth infrared radiation simulator. The ILRS experience with LAGEOS indicates that, in space, the real RC constant is modified with respect to the measurements on the ground.

For the RC measurements the typical requested accuracies from ILRS are a few tens of *psec*.

The lasers have pulse lengths down to 10 *psec* (equivalent to 3mm for a single pulse) and 2Khz repetition rates. If the RC is not known and is approximated for example using the LARES radius, this causes a systematic error for distance measurements. A careful RC measurements is necessary for avoiding systematic biases and contributing to the goal of reaching one millimeter accuracy.

2.6 LARES Optical Configuration and Comparison with LAGEOS

The specifications of the LARES CCRs are very similar to the specifications for LAGEOS and LAGEOS II. Unlike LAGEOS, the LARES satellite has a 15 cm radius and mounts about 100 CCR. The reasons for this type of configuration are tight budgets: the result is a reduction by a factor 4 both on the number of retro-reflectors and the final weight.

LARES will have about a 1200 km operating altitude (4800 less than LAGEOS) with about 7.2 km/s orbital velocity (1.5 km/s more than LAGEOS). This increases the velocity aberration from 38 μrad to 46 μrad and consequently increase of the CCR dihedral angle offset. The flat mirror pattern (Airy pattern) would have a diameter of 140 m for LAGEOS and 30 m for LARES.

Being smaller than LAGEOS, LARES has a smaller bending radius, so the average number of spotlighted CCR decreases from 1.5/2 to 1/1.5: the range correction decreases but its error (range variation) is the same between the 2 satellite.

The range variation turns out to be the same for the two satellites; in fact this is proportional to the satellite radius (r) and inversely proportional to the square root of the number of cube corners (N):

$$f_{RV}(N,r) \propto \frac{r}{\sqrt{N}}$$

Since there are about 4 times as many cubes on LAGEOS the averaging is better by about a factor of 2.

Because the radius of LARES is about half the size of LAGEOS the range correction is smaller and the variations would be smaller by about a factor of 2 if there were the same number of cubes. Since LARES has fewer cubes the two effects cancel each other so that the variation in the range correction is about the same for both satellites [13].

$$f_{RV}^{LARES}(N,r) \propto \frac{r_{LARES}}{\sqrt{N_{LARES}}} = \frac{1/2\, r_{LAGEOS}}{\sqrt{N_{LAGEOS}/4}} = \frac{r_{LAGEOS}}{\sqrt{N_{LAGEOS}}} = f_{RV}^{LAGEOS}(N,r)$$

3 FFDP Optical simulations

3.1 Simulation Software: Code V by ORA Inc.

Since the very beginning we decided, concurrently with the measurements on the optical bench, to carry on simulations of the FFDP patterns of the CCRs. Among the various choices of software we chose Code V ® provided by Optical Research Associates (ORA ®) http://www.opticalres.com/ , industry's leading supplier of imaging and illumination design/analysis software. Code V is a program used for the optimization, analysis and tolerating of image-forming optical systems and free-space photonic devices. Some of its applications are:

- **Digital camera lenses**: tolerance and fabrication analysis features
- **LCD projection systems**: polarization ray tracing
- **Telescopes & other visual systems**: polarization ray tracing
- **Space-borne systems**: environmental analysis
- **Laser scanning systems**: diffraction beam propagation analysis

One of its most famous application in aerospace has been the lens correction of the Hubble Space Telescope.

The program can accept commands either with a graphical user interface or typing commands directly from an apposite command window. It's possible to use a wizard program to introduce lenses from a data-base or, as in our case, particular objects, called Non-Sequential-Surfaces, by defining each surface. Once all the geometrical characteristics are introduced such as, laser beam wavelengths and polarization, many analyses are possible, such as diffraction, beam propagation, environmental, energy dispersion etc. An optimization tool is also available to optimize the system performances.

3.2 Description of the CCR Model

Code V has a suitable command to create the CCR by introducing its height, material, diameter of entrance surface, reflection characteristics and dihedral angle offsets. We generated the CCR with the same geometrical parameters as the LAGEOS CCRs (height of 27.330 mm, made with Fused Silica and radius of 19.05 mm) except the dihedral angle offsets; for those we started from 0 arcsec

and we made simulations at different values to compare them with measurements on the optical bench.

The command is:

CCR S_1 27.33 SILICA TIR 0 0 0

The command TIR stands for Total Internal Reflection, which is the main optical characteristic of the CCR. S_1 is the first surface of the CCR. After that has to be entered the dimension and optic characteristic of the entrance surface:

CIR S_1 CLR 19.05

The entrance surface is circular with a clear aperture (only rays inside the surface pass) of 19.05 mm.

After that all the optical system parameters are introduced such as the laser beam diameter, its wavelength, the polarization and the inclination with respect to the entrance surface. The CCR is a system whose light in image space is approximately collimated; in Code V this can be done specifying that the system is treated in True Afocal Mode. In this mode the dimensions of the FFDP patterns have been set to μrad. In the following figures are reported 3D models of the CCR.

The scale is normalized to peak intensity in any given FFDP.

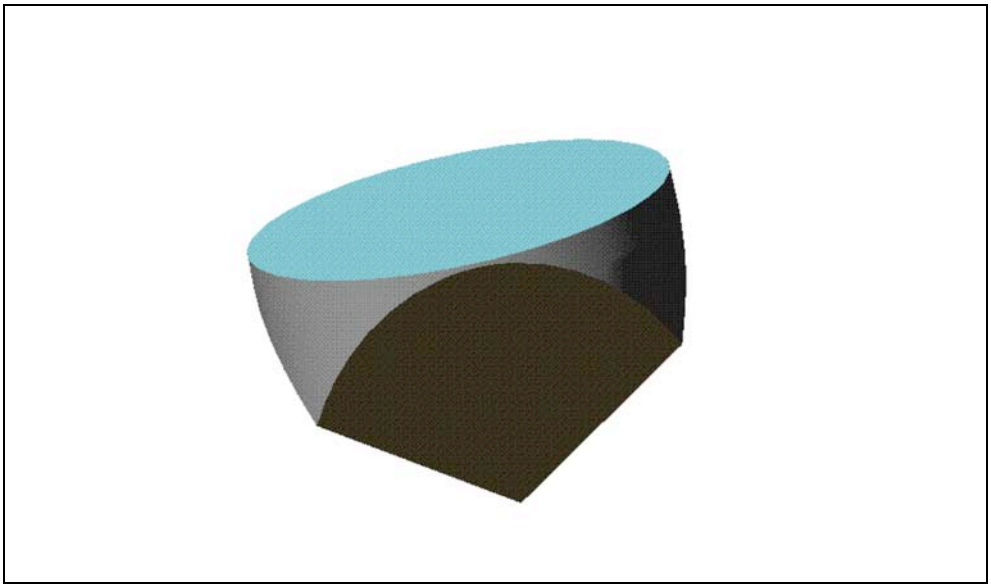

Figure 3.1 – 3D CCR model -

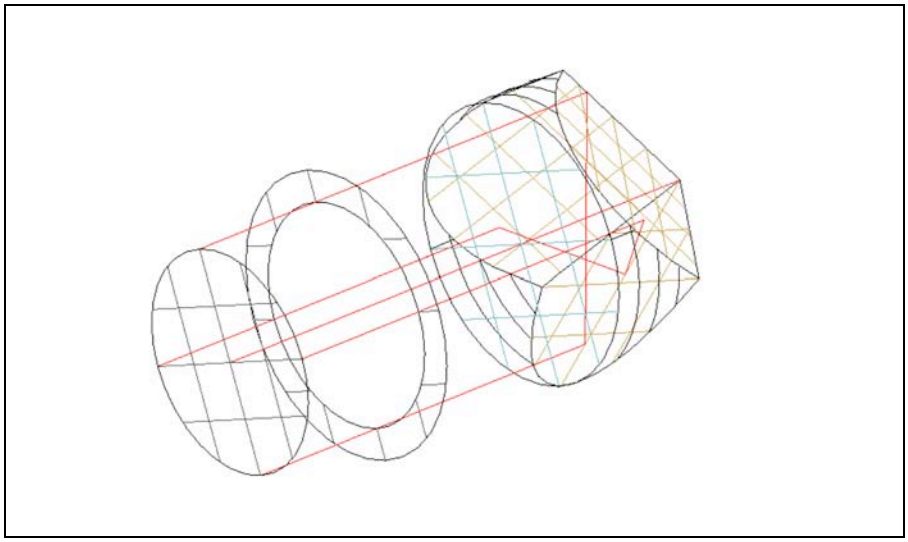

Figure 3.2 - 3D ray tracing inside the CCR –

3.3 Simulation Results

In Code V the analysis of the diffraction pattern is made with the command PSF which computes the wave aberration of the system, and, by Fast Fourier Transform (FFT), the diffraction image shape in the designated focal plane integrated over the wavelengths according to the weights assigned to the system. This image patch is represented in the computer by intensity values in a grid across the image with the chief ray as the center point of the grid. Grid dimensions and spacing are controlled to have an image with the suitable resolution and dimension. First of all we made a simple simulation of a diffraction pattern of a flat mirror, which should have a classic Airy peak pattern, just to understand the characteristics of the PSF command. Moreover this simulation, as in the optical bench measurements, could be a useful reference for the CCR FFDPs.

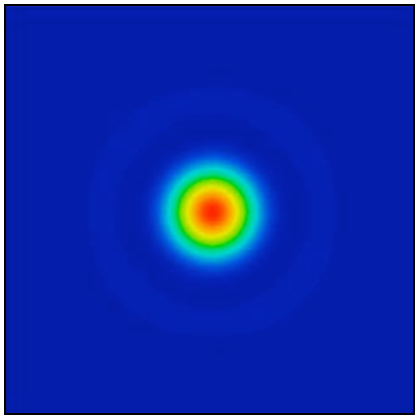

Figure 3.3 - Diffraction pattern (Airy pattern) of a flat mirror. Grid dimensions ± 50 μrad -

Positioning the CCR as in Figure 3.4, defined with 0 arcsec of dihedral offset and dimensions as previously mentioned, its FFDP pattern, for a vertical polarized beam, is as in Figure 3.5.

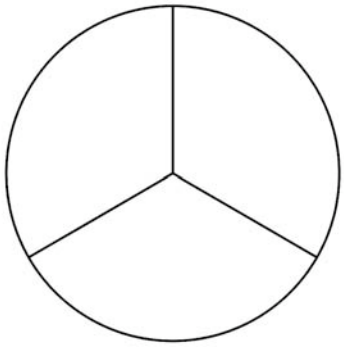

Figure 3.4 - View of the CCR from the top –

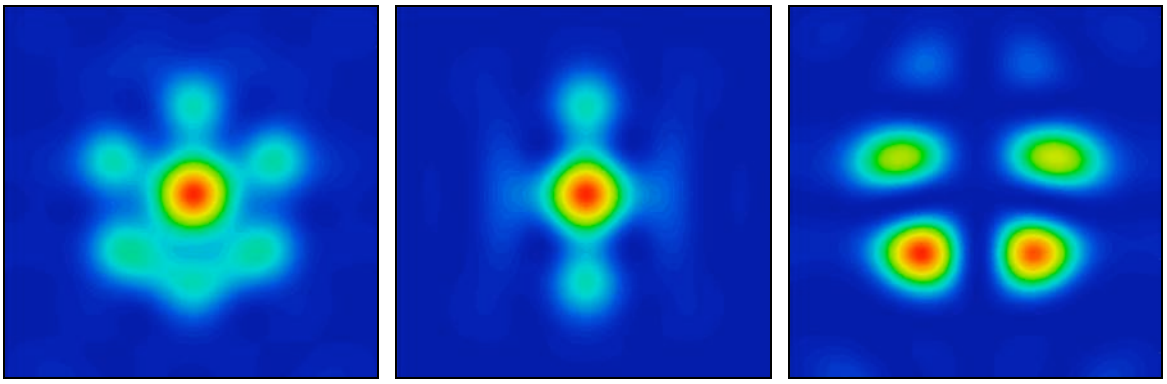

Total Energy Parallel component Orthogonal component

Figure 3.5 - Diffraction pattern of an uncoated CCR with 0 arcsec dihedral offset and Vertical Polarized laser beam. Grid dimensions ± 50 μrad -

The pattern shows a central peak, in which is concentrated most of the reflected energy, with smaller spots of less intensity. Since the CCR is symmetric with respect to the vertical axis (i.e. Y axis in the simulations), see Figure 3.4, we expect the patterns to be left-right symmetric. Both the total energy and the two components have this symmetry.

Polarization in the case of the CCR affects the shape of the pattern, and will be explained later; from now on the simulations will be presented with horizontal polarization as in the measurements taken in the optical bench. Figure 3.6 shows how a rotation of 90º of the polarization rotates the diffraction pattern of the CCR by 180º.

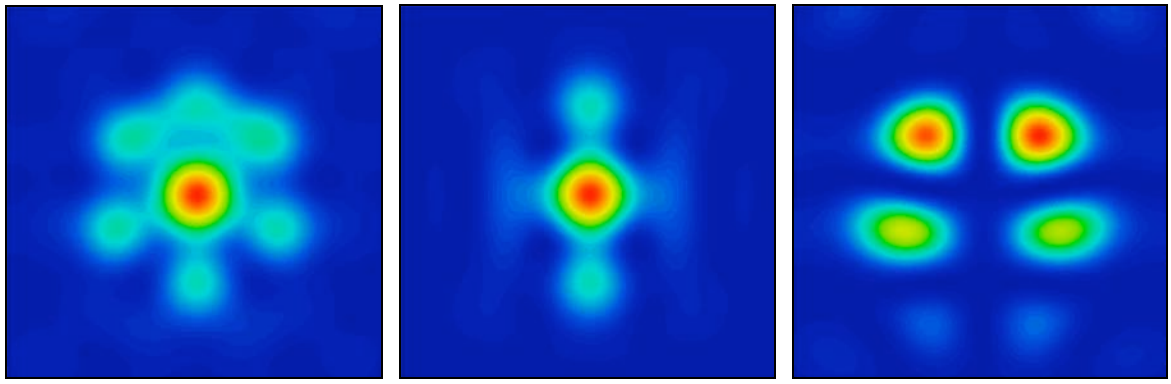

Total Energy Parallel component Orthogonal component

Figure 3.6 - Diffraction pattern of an uncoated CCR with 0 arcsec dihedral offset and Horizontal Polarized laser beam. Grid dimensions ± 50 μrad -

3.3.1 FFDP Dependence on CCR Dihedral Angle Offsets

Studies made on the two LAGEOS satellites showed a problem: the relative motion between the satellite and the ground station prevents the retro-reflected laser beam from coming back to the source. This effect is called Velocity Aberration. A perfect CCR, 0 arcsec of offset, has the main energy concentrated in the central peak, see Figure 3.5, and due to the velocity aberration this peak won't be seen by the ground station. For the LAGEOS satellites the velocity aberration has been calculated to be ~36 μrad. For the ground station to receive enough energy from the CCR, the maximum energy needs to move to larger radii; this is possible by increasing the dihedral angle offsets. The CCR won't have anymore an angle of 90º between the back planes, but more. So given a certain velocity aberration, with simulations the correct angle offset will be chosen for the satellite; this is what will be done with the LARES satellite. The next figures show the change of the pattern by increasing of the offset angle, for a laser beam vertically polarized.

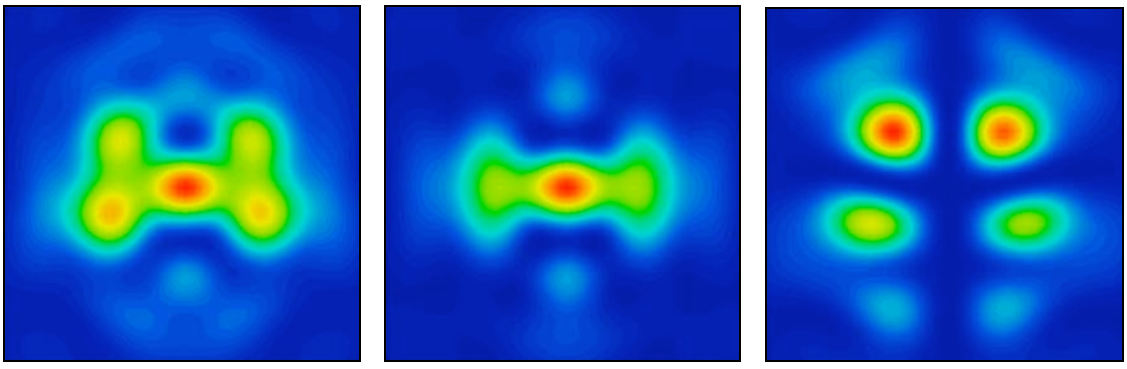

Total Energy Parallel component Orthogonal component

Figure 3.7 -Diffraction pattern of an uncoated CCR with **0.75 arcsec** dihedral offset and Horizontal Polarized laser beam. Grid dimensions ± 50 μrad –

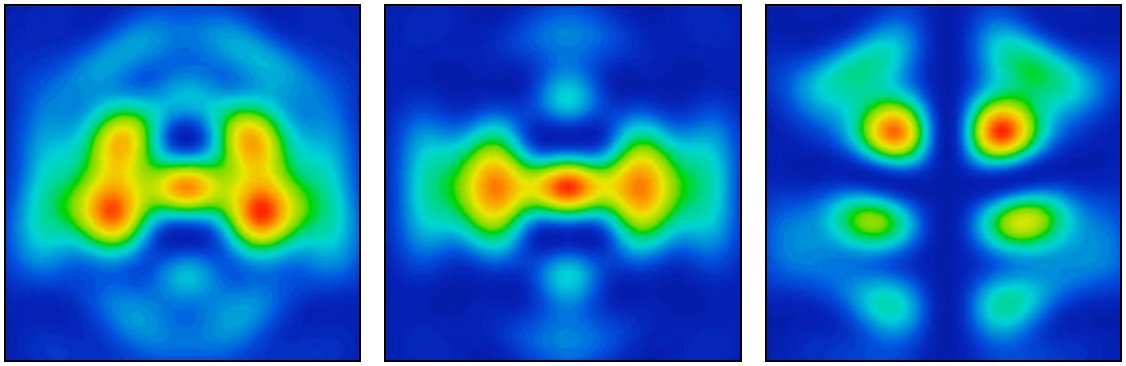

Total Energy Parallel component Orthogonal component

Figure 3.8 - Diffraction pattern of an uncoated CCR with **1.00 arcsec** dihedral offset and Horizontal Polarized. Grid dimensions ± 50 μrad –

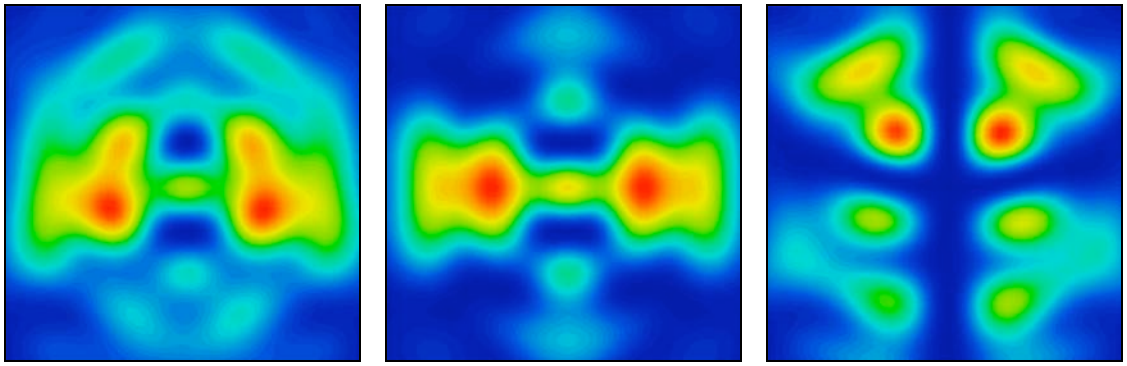

Total Energy Parallel component Orthogonal component

Figure 3.9 **-** Diffraction pattern of an uncoated CCR with **1.25 arcsec** dihedral offset and Horizontal Polarized. Grid dimensions ± 50 μrad –

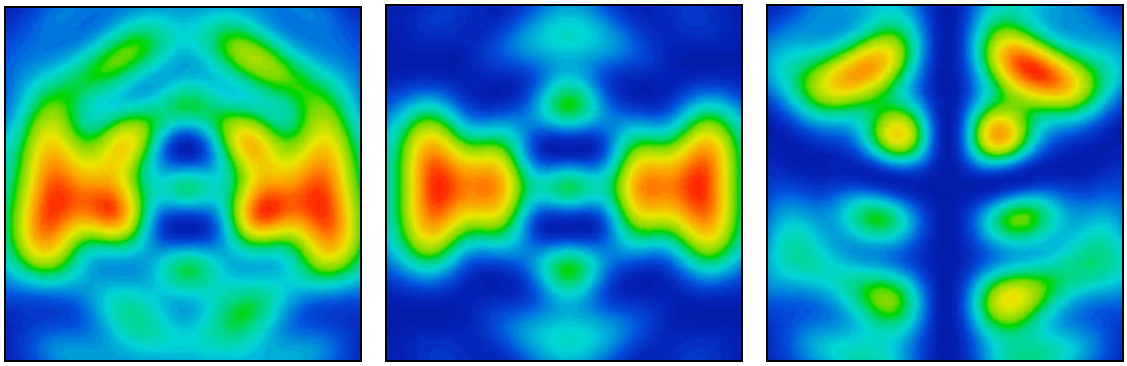

Total Energy Parallel component Orthogonal component

Figure 3.10 **-** Diffraction pattern of an uncoated CCR with **1.50 arcsec** dihedral offset and Horizontal Polarized .Grid dimensions ± 50 μrad –

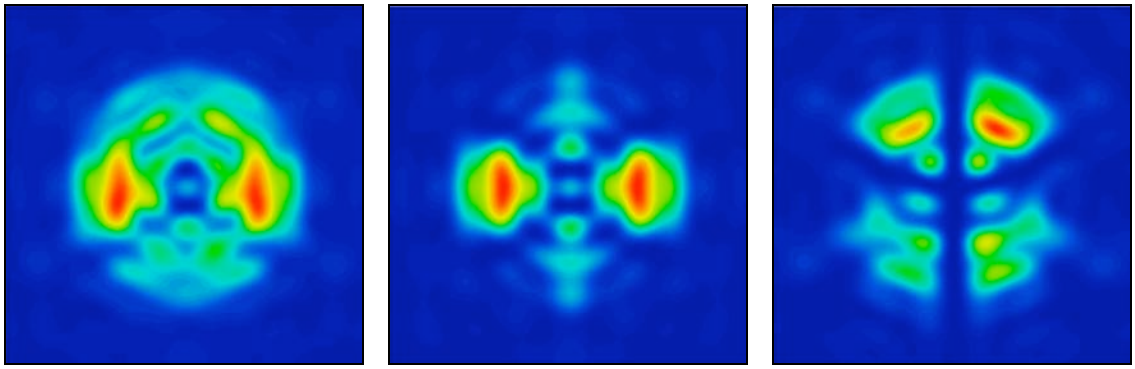

Total Energy Parallel component Orthogonal component

Figure 3.11 - Diffraction pattern of an uncoated CCR with **1.75 arcsec** dihedral offset and Horizontal Polarized. Grid dimensions ± 100 μrad –

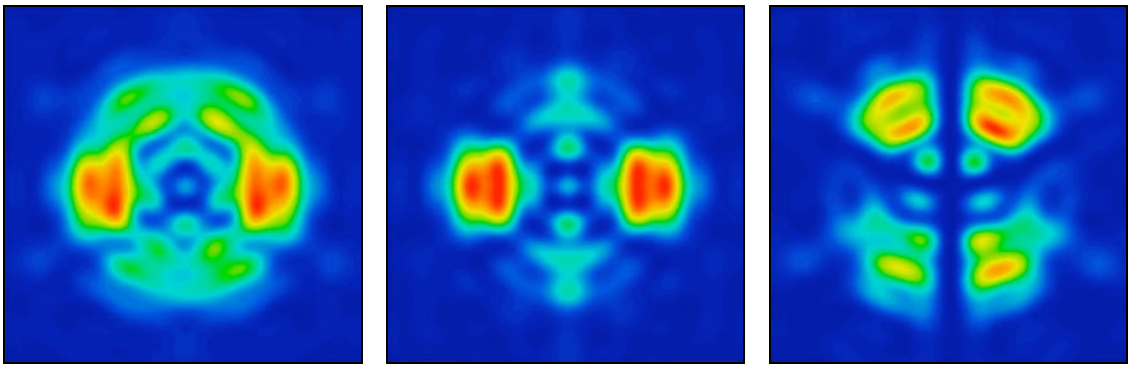

Total Energy Parallel component Orthogonal component

Figure 3.12 - Diffraction pattern of an uncoated CCR with **2.00 arcsec** dihedral offset and Horizontal Polarized. Grid dimensions ± 100 μrad -

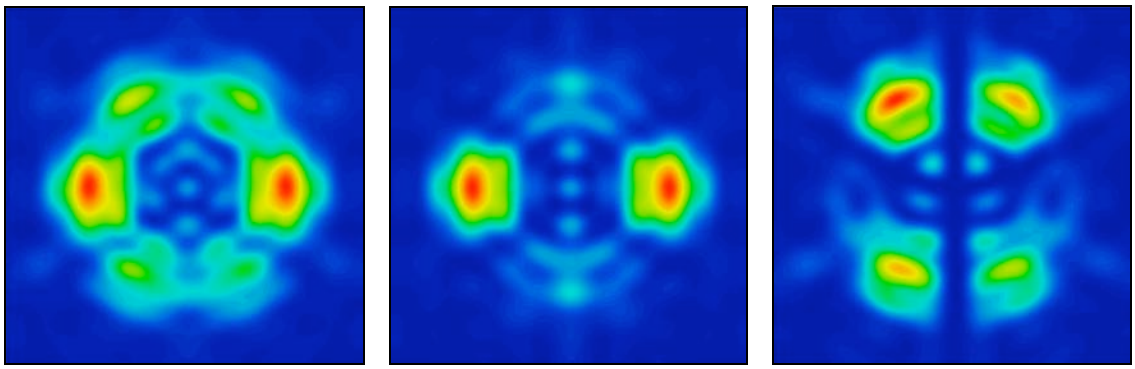

Total Energy Parallel component Orthogonal component

Figure 3.13 - Diffraction pattern of an uncoated CCR with **2.25 arcsec** dihedral offset and Horizontal Polarized. Grid dimensions ± 100 μrad –

3.3.2 Influence of the Polarization Orientation on the Diffraction Pattern

Till now we have considered patterns generated from an input laser beam vertically polarized. The orientation of the polarization or a rotation in azimuth of the CCR has a great influence on the pattern. The main effect is the rotation of the pattern with a slight change of it. A rotation of 90º in the polarization instead, changes completely the pattern. The next figures show the patterns of an uncoated CCR with a 1.25 arcsec dihedral offset, for rotations of the polarization from -45º to 90º. 0º is a vertical polarization.

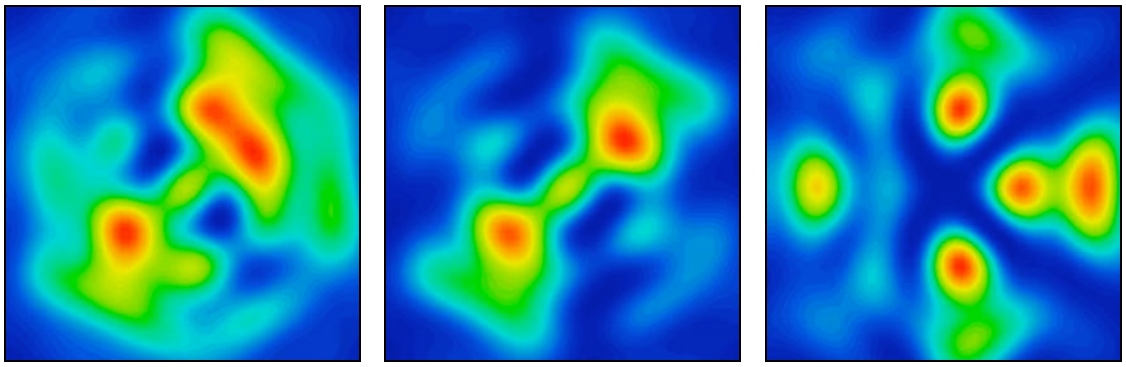

Total Energy Parallel component Orthogonal component

Figure 3.14 - Diffraction pattern with **-45º** polarized beam -

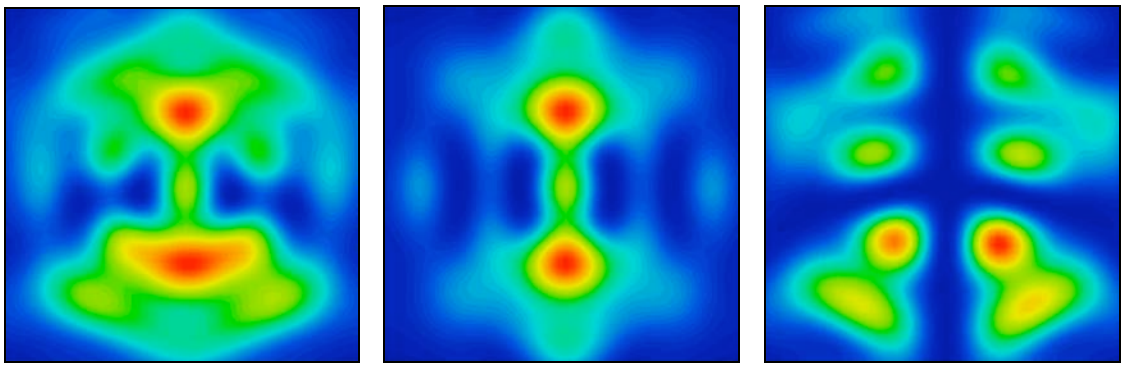

Total Energy Parallel component Orthogonal component

Figure 3.15 - Diffraction pattern with **0º** polarized beam -

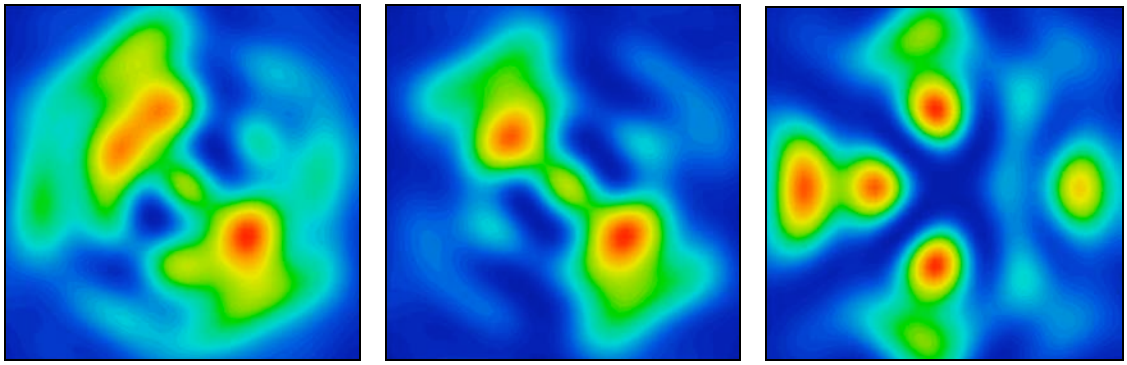

Total Energy Parallel component Orthogonal component

Figure 3.16 - Diffraction pattern with **45º** polarized beam -

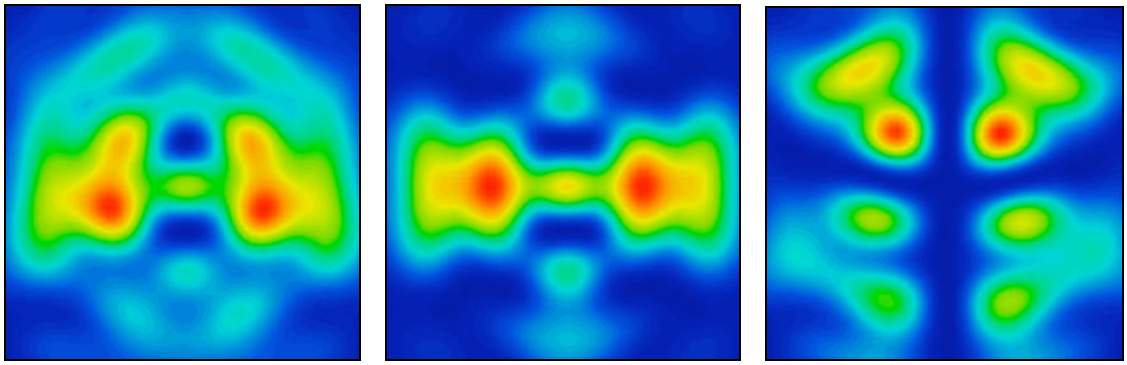

Total Energy Parallel component Orthogonal component

Figure 3.17 - Diffraction pattern with **90º** polarized beam -

3.3.3 Influence of the laser beam incidence angle on the pattern

All the simulations presented have been made for a laser beam orthogonal to the CCR; although this is not the common situation. The LAGEOS satellites are spherical and in the luckiest case only one CCR receives the laser beam orthogonal. The rest of the CCRs receive a beam with a certain inclination. At a certain incidence angle there is a loss of total internal reflection and a reduction in energy. For this reason the CCRs' patterns must be studied at different incidences of the laser beam, to check the limits of total internal reflection. The following figures show the patterns of an uncoated CCR with 0 arcsec dihedral angle offset with a laser beam vertically polarized. The CCR is in the configuration shown in Figure 3.4; the incidence angles are positive when the beam is tilted up (the beam is always in the Y-Z plane), negative in the opposite case.

A positive inclination causes an early loss in total internal reflection (the patterns are computed until the loss of total internal reflection) while with a negative one the patterns can be seen up to higher inclinations. This is a common behaviour with the CCRs when the plane of incidence passes through the three back edges.

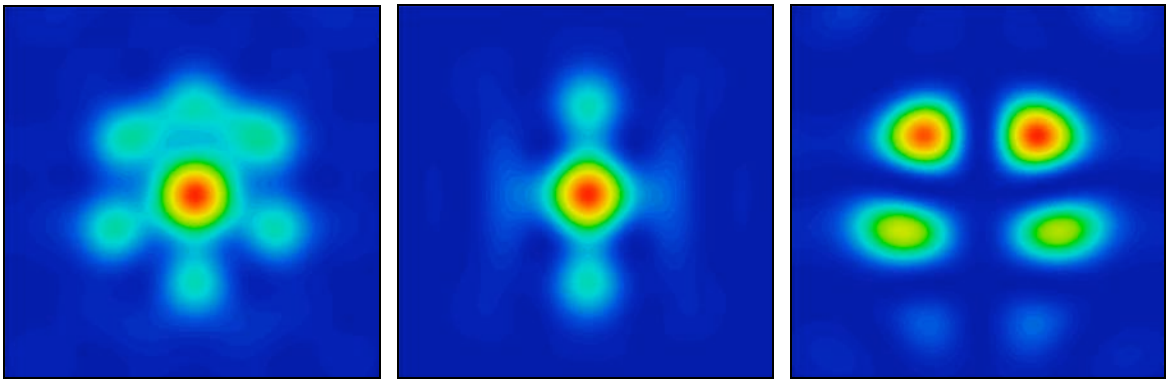

Total Energy Parallel component Orthogonal component

Figure 3.18 - Diffraction pattern with **0º** of inclination -

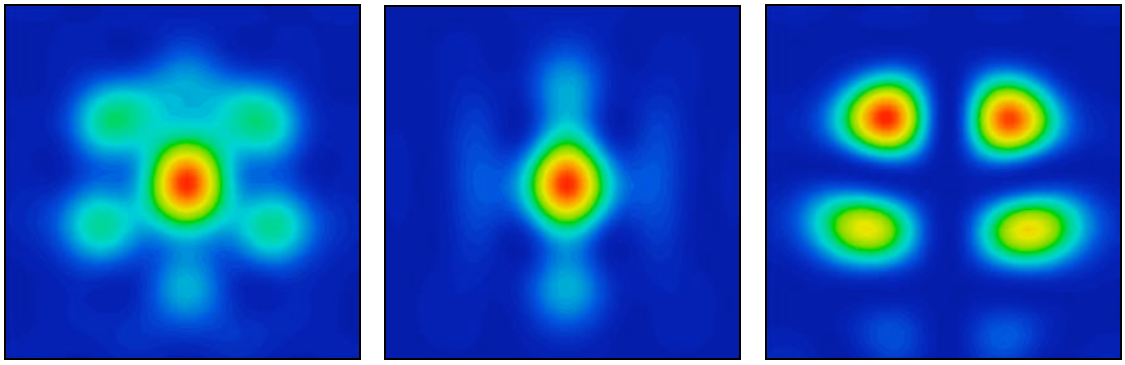

Total Energy Parallel component Orthogonal component

Figure 3.19 - Diffraction pattern with **-5º** of inclination -

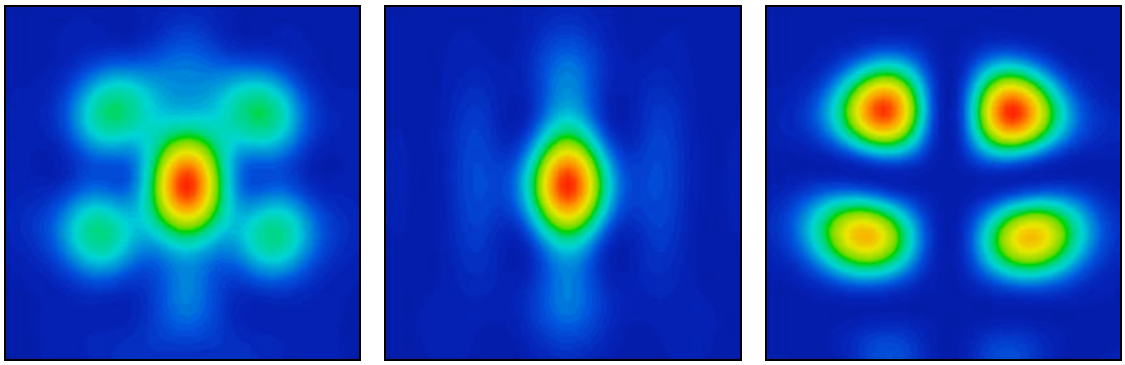

Total Energy Parallel component Orthogonal component

Figure 3.20 - Diffraction pattern with **-10º** of inclination –

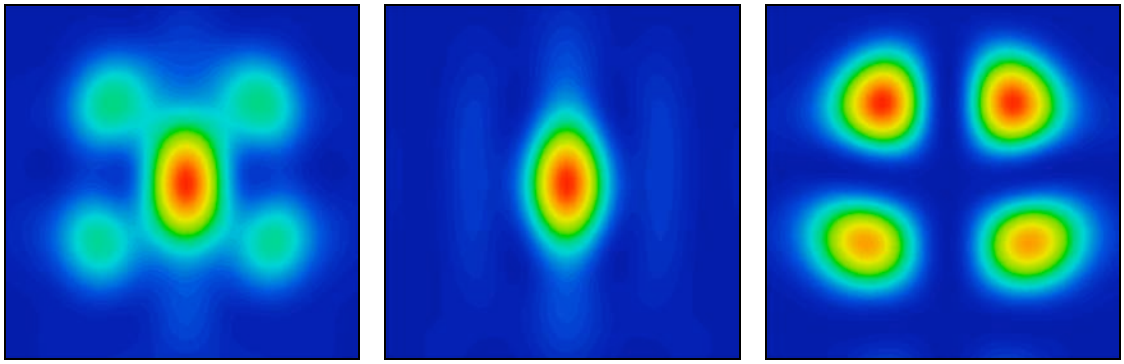

Total Energy Parallel component Orthogonal component

Figure 3.21 - Diffraction pattern with **-15º** of inclination -

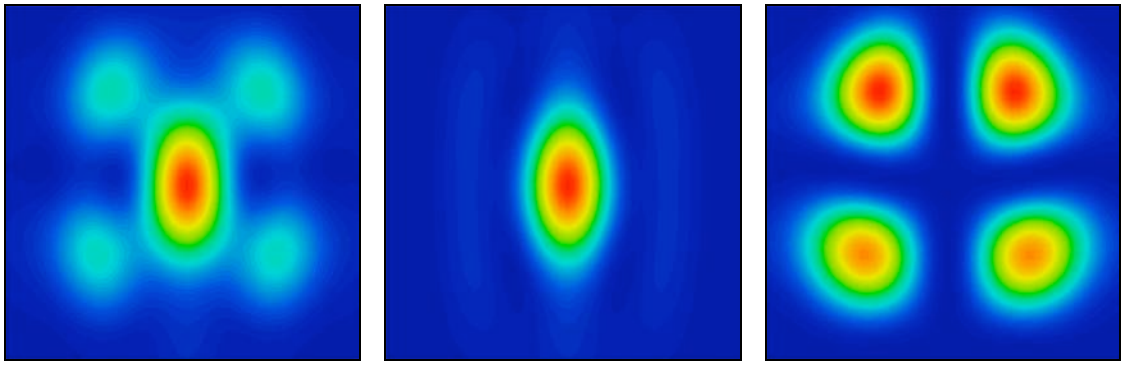

Total Energy Parallel component Orthogonal component

Figure 3.22 - Diffraction pattern with **-20º** of inclination –

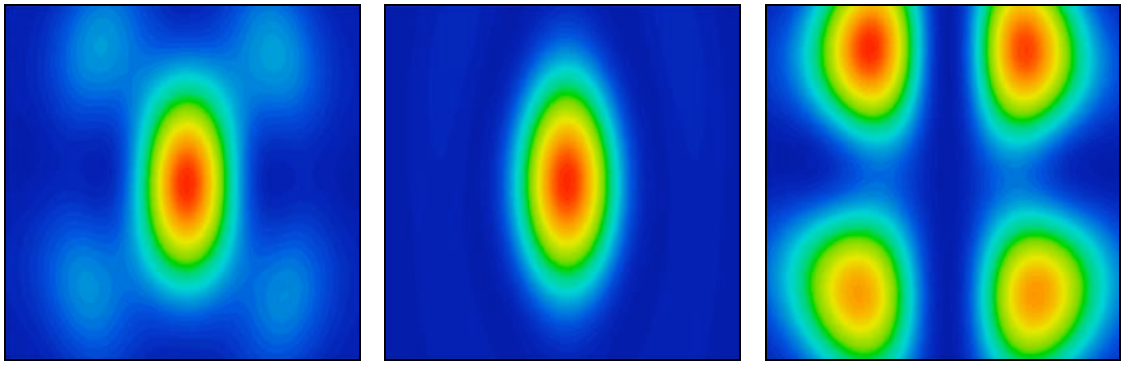

Total Energy Parallel component Orthogonal component

Figure 3.23 - Diffraction pattern with **-28º** of inclination –

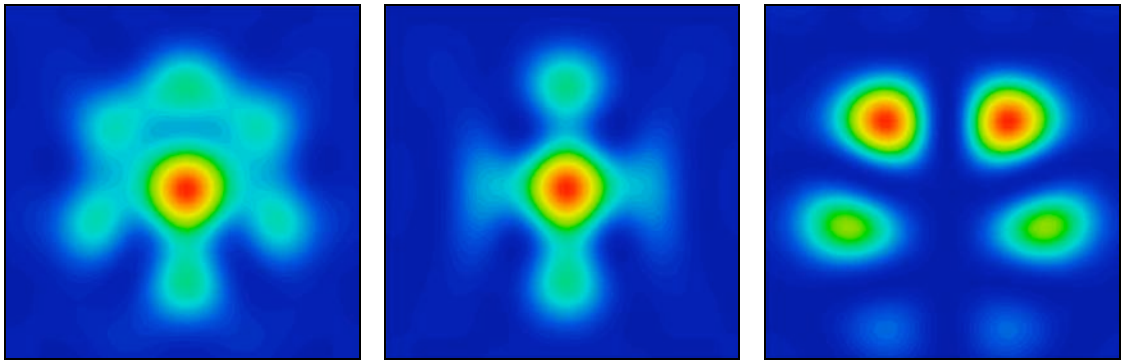

Total Energy Parallel component Orthogonal component

Figure 3.24 - Diffraction pattern with **5º** of inclination -

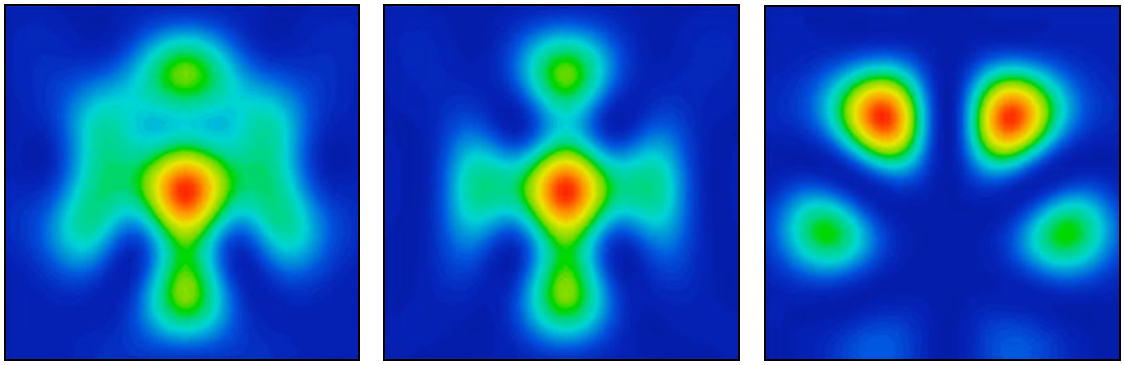

Total Energy Parallel component Orthogonal component

Figure 3.25 - Diffraction pattern with **10º** of inclination -

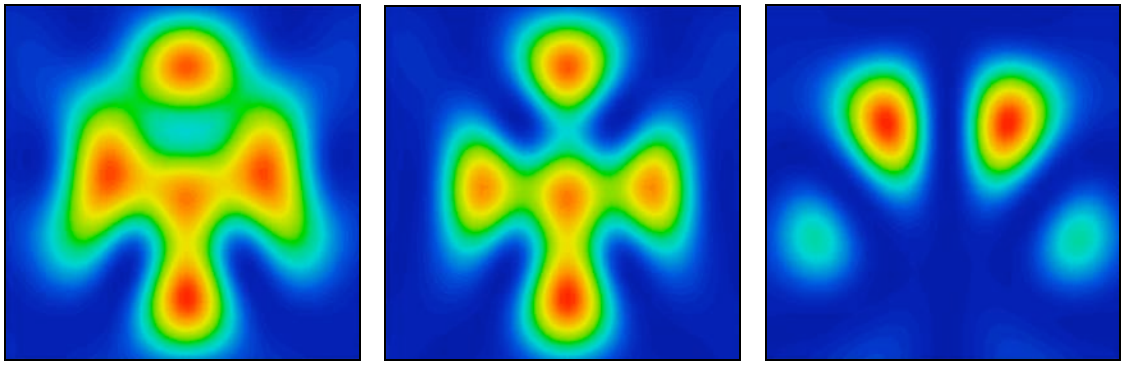

Total Energy Parallel component Orthogonal component

Figure 3.26 - Diffraction pattern with **15º** of inclination –

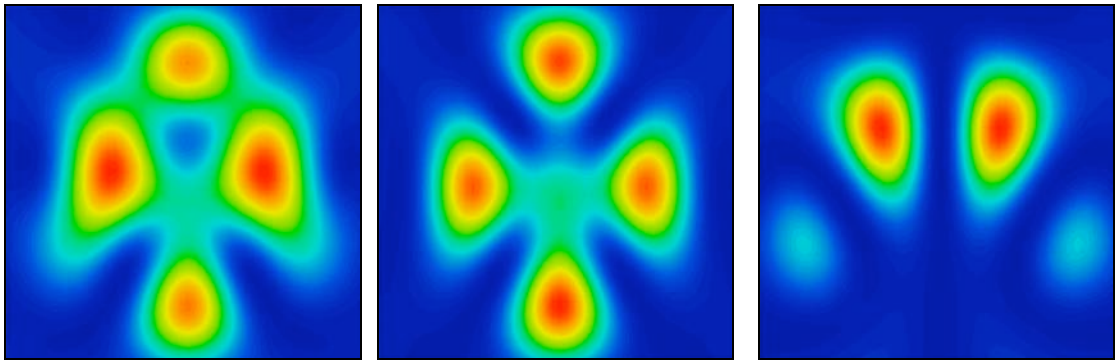

Total Energy Parallel component Orthogonal component

Figure 3.27 - Diffraction pattern with **16.5º** of inclination -

4 The FFDP Experimental Measurements

4.1 Optical Circuit

The optical circuit will be realized in order to measure the Far Field Diffraction Pattern (FFDP) of the CCR and to analyze and validate the nominal shape characteristics.
Setting up the optical circuit the most critical part is the alignment of the beam exiting from every optical component.
Therefore the optical circuit will be realized step by step, starting from simple configuration (without lenses). Only in a second phase we will add lens and objectives in order to have the FFDP.

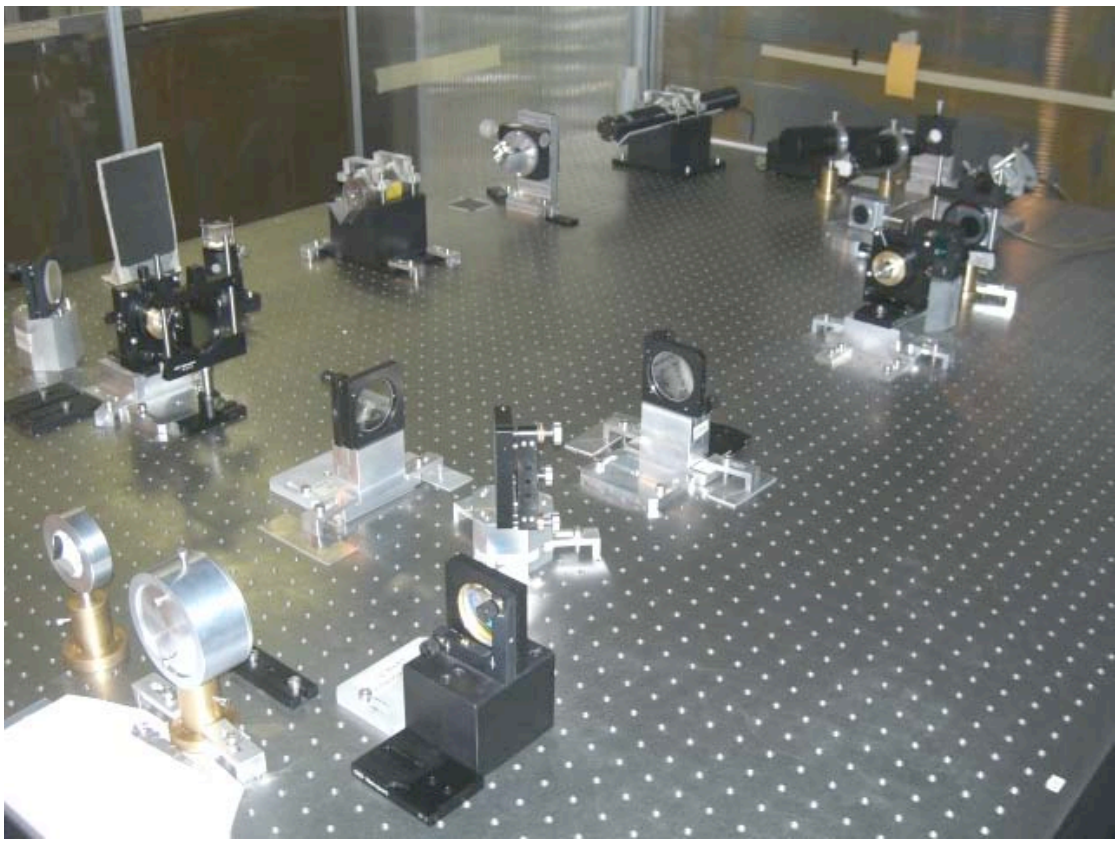

Figure 4.1 – Optical circuit at INFN-LNF -

4.1.1 Optical Axis

We define as “optical axis” the laser light path with constant diameter and height from the bench.
First we will work on a simplified aligned circuit, without beam expander and reducer.

Defining an optical axis is very convenient making up the circuit: in fact as we add critical components for the alignment (as lens and objective) the optical axis reference will make the task easier: when we add each one of those components to the circuit we will check for the beam to come back on the same path.
The circuit in its first configuration is constituted by the following components:

- 1 laser He/Ne low power (7mW approximately)
- 2 beam polarizer
- 1 Faraday rotator
- 1 mirror at 45° with respect to optical axis
- 1 CCR
- 1 beam splitter
- 1 filter
- 1 CCD camera

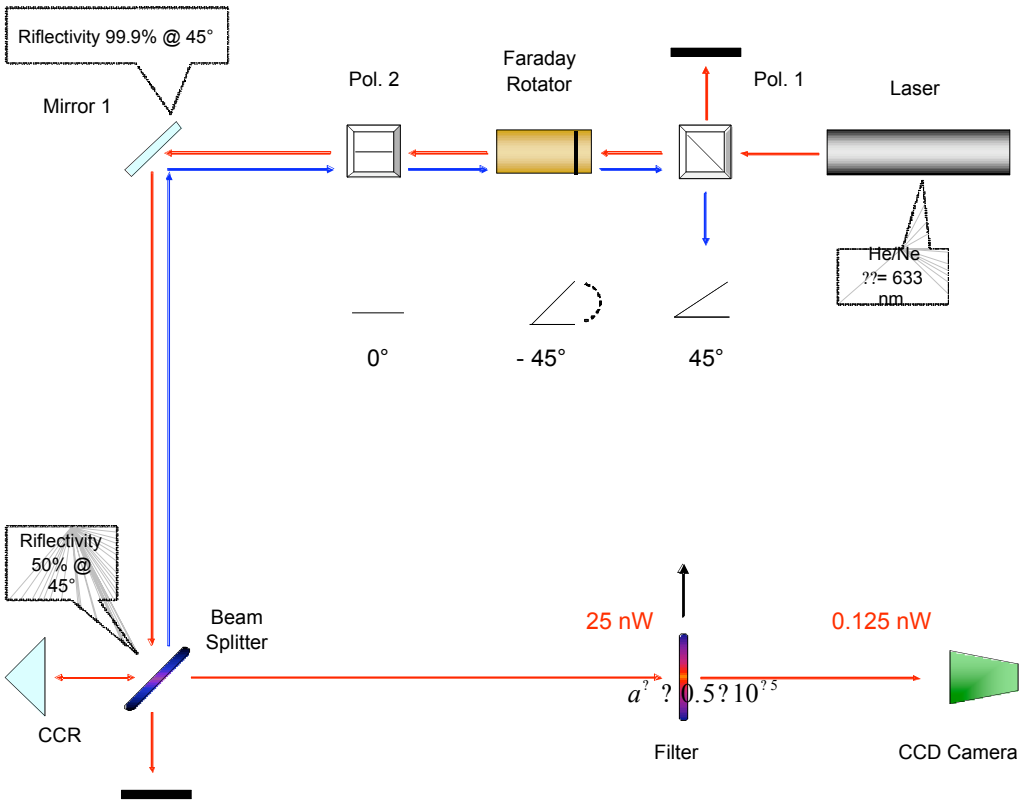

Figure 4.2 – Optical axis scheme-

The laser creates theoretically a beam with constant polarization (however introducing a Faraday rotator, hypothetical fluctuations will be removed): the beam goes through the first polarizer which allows only the 45° component with respect to the horizontal.

Therefore it is possible to adjust the beam intensity by simply rotating the laser body around its longitudinal axis: for CCD sensor safety the laser will be rotated until only 10% of full power will pass through the first polarizer.
After the first polarizer the Faraday rotator will rotate the beam by -45° bringing the polarization to 0°. The second polarizer allows only the horizontal (0°) component to get through and therefore, in this case, all the power available after the Faraday rotator. This part of the circuit is necessary to avoid laser beam coming back to the source: in fact any light coming back will be rotated by the Faraday rotator by -45°. Thus the polarization at this point is -45°. This polarization does not allow getting through the first polarizer, and consequently reaching the laser, since it is orthogonal to the polarization of this polarizer.
Mirror 1 is necessary only to optimize the space on the table. Then the beam splitter (semi-reflecting mirror) splits the beam in 2 parts; one of these will be reflected from the CCR and will reach the CCD sensor for image acquisition, while the other will be dissipated on a second blackboard.
Since now the circuit is working without lenses and objectives, thus the laser beam remains point-like. When the beam cross-section is narrow compared to the CCR, as in this case, if you want to observe the FFDP you must ensure that the beam hits CCR at the center (at the 3 corners intersection): in fact only in this way the beam hits simultaneously the 3 faces of the retro-reflector producing interference and then the FFDP. If the spot hits only one of the 3 faces interference will not occur and, furthermore, the retro-reflected beam will be translated by a quantity equal to the distance between the incidence point and the center of CCR, compromising the search for the optical axis.
In a second phase a flat mirror will be used, in place of the CCR, in order to obtain a reference pattern to be used to normalize the pattern of the CCR. Even though it would be more logical to obtain, since the beginning, the FFDP from the flat mirror, in practice, it turns out to be more comfortable to use a CCR in the alignment phase because, it is not sensitive to any misalignment. In fact no matter the beam incidence angle with respect to the front face of the CCR, the reflecting beam will always (at least for angles not too large) go back in the same direction. Finally, before the CCD camera sensor, the beam will be attenuated by a filter to reduce the power in order to avoid possible damage to the CCD.

4.1.2 The Complete Circuit

Once defined the optical axis, it is much simpler to introduce the beam expander and beam reducer in the circuit. These are formed by a lens-objective system which have the purpose to increase

(from 0.8 to 4 mm) the beam diameter in the first part of the circuit, so that it completely intersect the CCR, and later to reduce it in order to use at best the active CCD sensor surface.

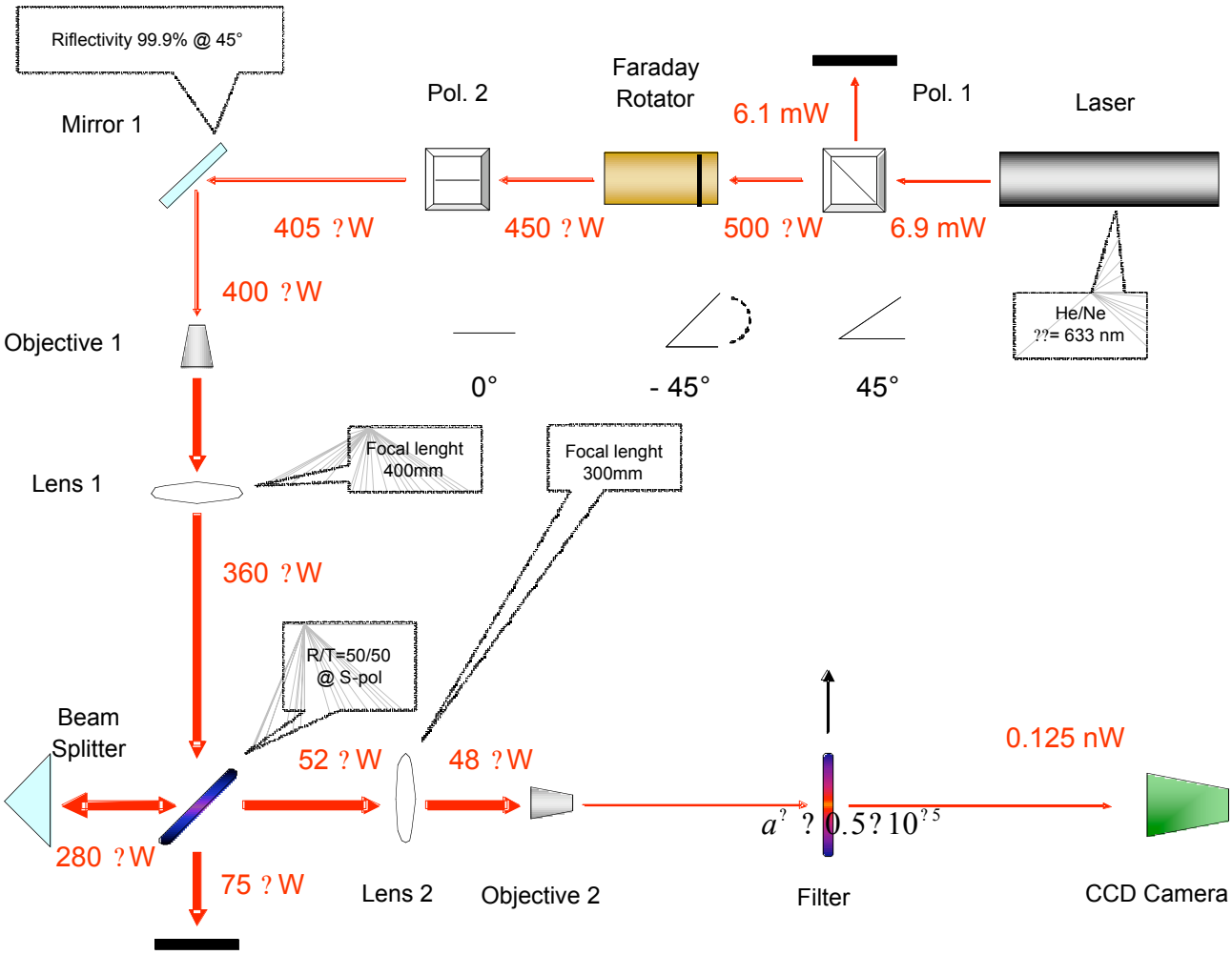

Figure 4.3 – Optical circuit scheme -

First of all we introduce the two lenses, one at a time, to be able to adjust the supports on which these are mounted so that their presence does not modify the optical axis. We can now introduce the 2 objectives; these must be introduced, unlike the lenses, simultaneously, since their function is to expand the beam cylindrically and as a consequence the optical axis is no longer traceable.
Concerning the alignment, these components are the most critical: in fact, as mentioned, they have to be simultaneously positioned and therefore, for this reason, we do not know to which of the two objective attribute any possible misalignment; furthermore they have to be positioned at a precise distance from the lenses to which they are coupled, so that the 2 focuses superimpose perfectly. This is the condition to have the beam expanded and collimated.

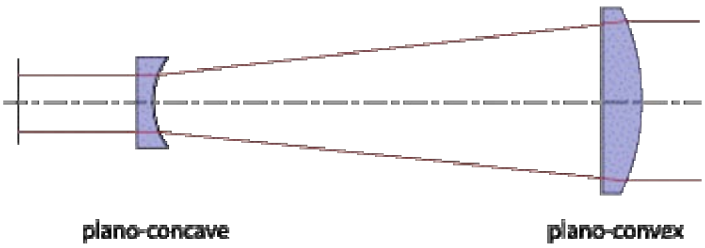

Figure 4.4 - Galilean beam expander scheme -

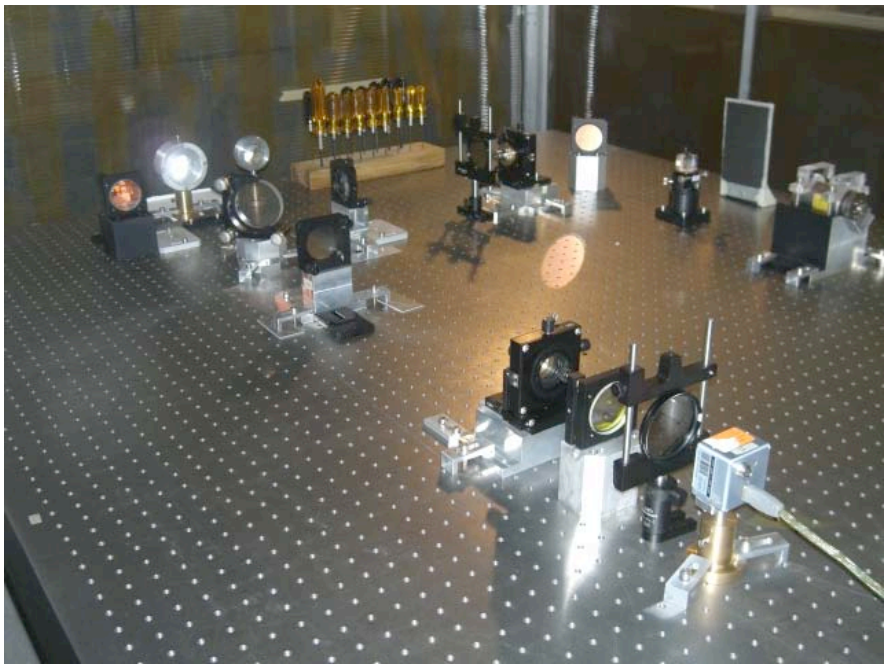

Figure 4.5 - Galilean beam expander –

Before inserting the objectives it turns out useful to replace the CCR with a flat mirror so that it is possible to verify the beam "cleaningness" and to better monitor its divergence. In fact the flat mirror has a well known pattern, of gaussian type, with which is much simpler, compared to pattern of the CCR, to note any possible variation introduced by the lens-objective systems.

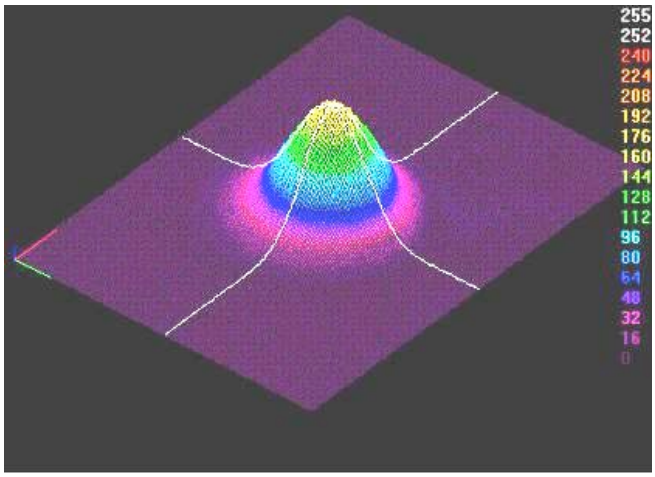

Figure 4.6 – Gaussian beam profile -

Also in this case, upon the replacement of the CCR in place of the flat mirror, we will have to adjust the latter so that to get back the optical axis. Once optimized the position of lenses and objectives it is possible to replace the flat mirror with the CCR and to obtain the first FFDP images.

4.1.3 Optical Axis Definition

Set up goals:

1. Install hardware (CCD camera and pc connected to it) and image acquisition software.
2. Design and manufacturing of the holding devices for CCRs, CCD camera and fixing clamps.
3. Measure the laser beam intensity and create an intensity laser beam map of the circuit.
4. Calculate the attenuation factor of the beam for image acquisition.
5. Confirm the previous calculation by experimental measurements and choose the right filter to position in front of the CCD camera.
6. Acquire the first FFDP images (of the flat mirror and CCR) from CCD camera.

Hardware and software installation

The CCD camera (fig.4.6) is connected to the computer which is positioned outside the room where the optical table is situated. The connection between the CCD camera and the computer is obtained by fire wire (FW) connection.

Two are the CCD camera available; one is positioned at the end of the optical circuit in order to acquire the FFDP of CCR while, the second one, will be positioned from time to time, during the alignment phase, in several parts of the circuit with the purpose to monitor the beam: this procedure allows to verify the right positioning and the right use of every single component present on optical circuit.

Figure 4.7 - CCD camera -

The mounts

Supports have to be designed and manufactured to be fixed on the optical bench so that all the optics mounted on them such as the CCR and CCD camera, have their optical axis at the same distance form the table (10 cm approximately). In particular they should have one to two degrees of freedom: this requirement will turn out to be fundamental in the laser beam alignment phase.

Once realized the supports, also the clamps have to be manufactured in order to fix the supports to the optical table: these are "L" shaped having a hole on the longest side, inside which the fixing screw will be accommodated to the table.

Another requirement for the supports is to have a surface as opaque as possible, to avoid laser beam reflections that, above all in the set up phase, could be potentially dangerous for the operator's eyes.

.

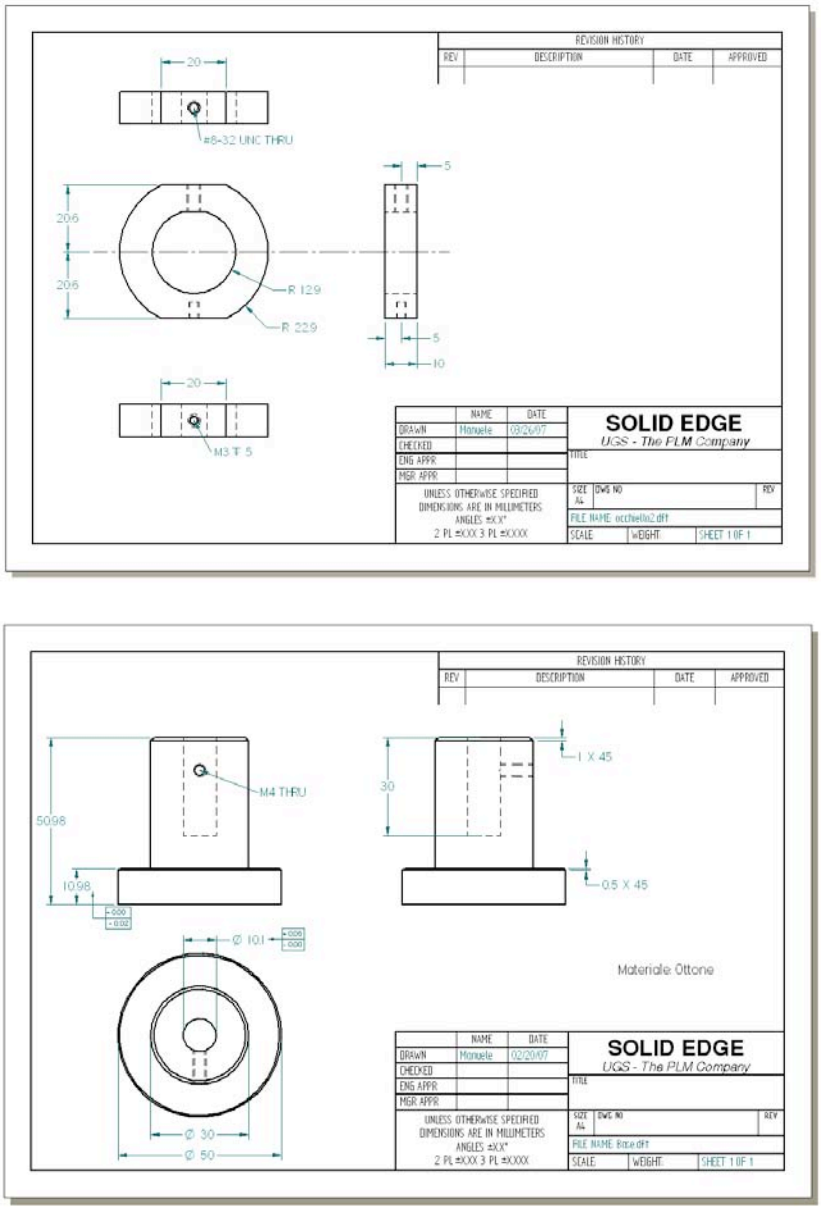

Figure 4.8 – Mounts for optical components -

Laser beam intensity

The laser is a He/Ne CW (continuous wave) with low power (5mW) with wavelength equal to 633 nm.

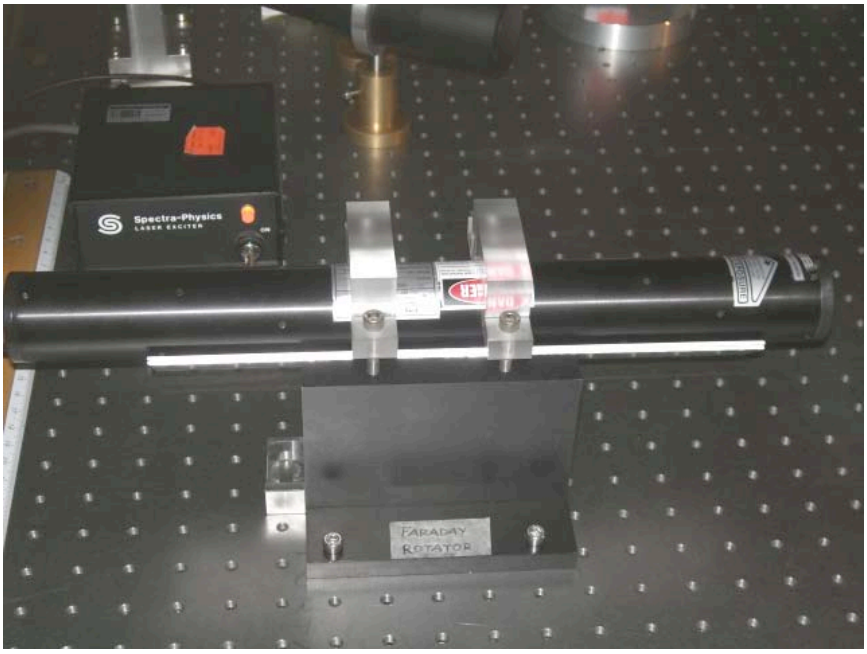

Figure 4.9 - Laser He/Ne –

This laser has a linear polarization: this feature allows adjusting the power by simply rotating the body of the laser and exploiting the first polarizer, placed after the laser.

In fact the first polarizer allows only the component at 45° (with respect to the horizontal) to go through.

In order to measure the real power exiting from the first polarizer it is necessary to use a laser power meter. The power will vary in a range between 0 and 5 mW.

Attenuation factors

The He/Ne laser available in this phase has 5 mW power. Such power, even if relatively low, could be too high for the sensor of the CCD camera and consequently could damage it. For this reason the laser power has to be compared with the acceptable one from the sensor. Such power is not available on the sensor datasheet and therefore the comparison must be made by indirect way. Having the "full well capacity" (i.e., the max number of photon that is acceptable by the sensor) of the sensor (from datasheet), we know the maximum number of electrons that can be stored by each individual pixel; this will be compared with the number of electrons that really appear on the sensor

when the beam's photons hits the CCD. To be able to calculate the number of photons that hit each individual pixel, it is necessary to know the real area of the sensor that will be reached by the laser beam.

The CCD area that we want to be hit by the laser beam must a fraction of the entire CCD active surface. In fact when mirror or an unspoiled CCR will be substituted by a CCR with spoiled dihedral angle the FFDP can extend outside the original area. Also by supposing that the entire laser energy falls on a smaller spot on the CCD is a conservative assumption for the CCD safety. For this reason our conservative calculation assume an area of 3.8 mm^2 that corresponds to approximately 1/10 of the total sensor surface:

$$N_\gamma = \frac{E_{laser}}{E_\gamma} = \frac{P_{laser} \cdot \Delta T}{h \cdot \frac{c}{\lambda}} \cong 1 \times 10^{15}$$

where

$N_\gamma \rightarrow$ numbers of photons;

$E_{laser} \rightarrow$ laser energy;

$E_\gamma \rightarrow$ single photon energy;

$P_{laser} \rightarrow$ laser power (5 mW);

$\Delta T \rightarrow$ integration time (70 ms);

$h \rightarrow$ Plank constant ($6.6 \cdot 10^{-34}$ J·s);

$c \rightarrow$ light speed in vacuum ($3 \cdot 10^8$ m·s^{-1})

$\lambda \rightarrow$ wavelength laser (633 nm)

As mentioned, this energy will be concentrated on 3.8 mm^2 that corresponds to 0.196 Mpixel. Dividing N_γ by the number of pixel in 3.8 mm^2 we obtain the number of photons per pixel $N^{\forall}_\gamma = 5 \times 10^9$ photons that corresponds, being the quantum efficiency near unity, to as many electrons for every pixel. By taking the ratio

$$\frac{5 \cdot 10^9}{1 \cdot 10^4} = 5 \times 10^5$$

or its inverse that we call attenuation factor of laser beam $a^-_{tot} = 2 \times 10^{-6}$.

Practically how we do to reduce of such factor the beam?

Every component of the optical circuit has its own attenuation factor; in particular the first polarizer has an attenuation factor of $1 \cdot 10^{-1}$ while the beam splitter (that in our case is a semi-reflective mirror rather than a cubic polarizer) has an attenuation factor that is a function of the angle of incidence of the impinging light. All we know is the attenuation when the beam is perpendicular to the surface, i.e. approximately $1 \cdot 10^{-1}$ at 45°, that is our case, we need to measure the attenuation using the power meter. Anyway assuming the value $1 \cdot 10^{-1}$ the reduction due to the components of the circuit is therefore equal to $1 \cdot 10^{-2}$. We have therefore

$$N^{\forall}{}_{\gamma} = 5 \times 10^{9} \cdot a^{-}{}_{pol} \cdot a^{-}{}_{bs} = 5 \times 10^{9} \cdot 1 \times 10^{-1} \cdot 1 \times 10^{-1} = 5 \times 10^{7}$$

So the filter to put before the CCD camera must have an attenuation factor $a^{-}{}_{filter} = 2 \times 10^{-4}$ so that $a^{-}_{tot} = a^{-}{}_{pol} \cdot a^{-}{}_{bs} \cdot a^{-}{}_{filter} = 2 \times 10^{-6}$.

In terms of power, if the beam has an intensity of 5mW, once reduced of a factor 2×10^{-6} (polarizer, beam splitter and filter), on the sensor surface should arrive a beam with power about of 10 nW; this power is absolute and conservatively calculated ; in terms of specific power we have:

$$\overline{P}_{tolerate} = \frac{10}{3{,}8} = 2.63 \ \ nW / mm^{2}$$

As saying, the calculation has been made in way as much as possible conservative, to be able have a security margin on the attenuation factor. In fact every single circuit component has, even if little, an its attenuation factor (a^{-}) what goes from 0.95 for the lenses and the objectives to 0.9 for faraday rotator, while for the mirrors one has factor of 0.99 approximately.

Furthermore also the quantum efficiency has a value lightly lower than the unity ($\varepsilon \cong 0.95$) and therefore not all the photons striking upon the sensor will contribute to have it saturated.

At last the choice to consider a tenth of the total sensor area does not turn out especially conservative cause the special form of Airy pattern: in fact, expanding the beam peak further on the 3.8 mm^{2}, we would risk that the part with smaller energy of FFDP can go out outside the sensor area (this area is of remarkable importance for our study).

Attenuation factor validation through experimental measurement

Unlike the nominal value, the outgoing power is equal to 6.8 mW. Therefore the laser will be rotated outgoing from the first polarizer obtaining 0.5 mW according to the theoretical calculations.

In this way, will continue in the circuit the 7% of its full power; this shows that the first polarizer attenuation factor is not exactly 0.1 but 0.07.

As regards lenses and objectives an attenuation of 10% ($a \cong 0.9$) is measured while for beam splitter an attenuation factor about 0.15 $\Rightarrow a_{B.S.} = 1{,}5 \times 10^{-1}$ (considering the double beam passage).

For mirror 1 we measure a tiny attenuation (1%), while for the mirror flat, being impossible get a direct measurement, we will follow the provided value of 1%.

At last the intensity value is measured immediately before the point where the filter will be positioned, obtaining a value of $48\mu W$ that is in according to theoretical calculated value ($50\mu W$).

Right filter choice

In order to have on sensor surface 10 nW it is necessary to use a filter with attenuation factor of $a^{-}_{filter} = 2 \times 10^{-4}$ ($50\mu W \longrightarrow 10nW$).

The used filter is a semi-reflective mirror with $\bar{a}_{filter} = 10^{-3}$: in this way the beam power passes from $50\mu W$ to $50nW$. A further power reduction it can be obtained opportunely regulating the integration time (shutter time) on acquisition software: this allows to have a wide security margin on the incoming power, having it a range that goes from a 0.01 ms minimum to a 130 ms. maximum.

First images acquisition

For this purpose we will use the same acquisition software employed for the theoretical calculation (Shutter Time = 70 *ms*) so that the first images be useful for validate the calculations carried out.

We note from the figures 1 and 2 that the sensor is saturated; in fact since the objectives are no longer in the circuit, the peak of the beam arrives on the CCD camera with a diameter of 0.2 *mm* that is equivalent to 0.125 mm^2 and therefore with a specific power of 100 nW/mm^2.

Since the sensor tolerates a specific power of 2.63 nW/mm^2, reducing of a factor 50 (from 70ms to 1.4ms) the Shutter Time, the sensor would not saturate anymore: in fact, with a small error margin, we observe alone saturation for Shutter times superior to 1.2 ms (figures 3 and 4).

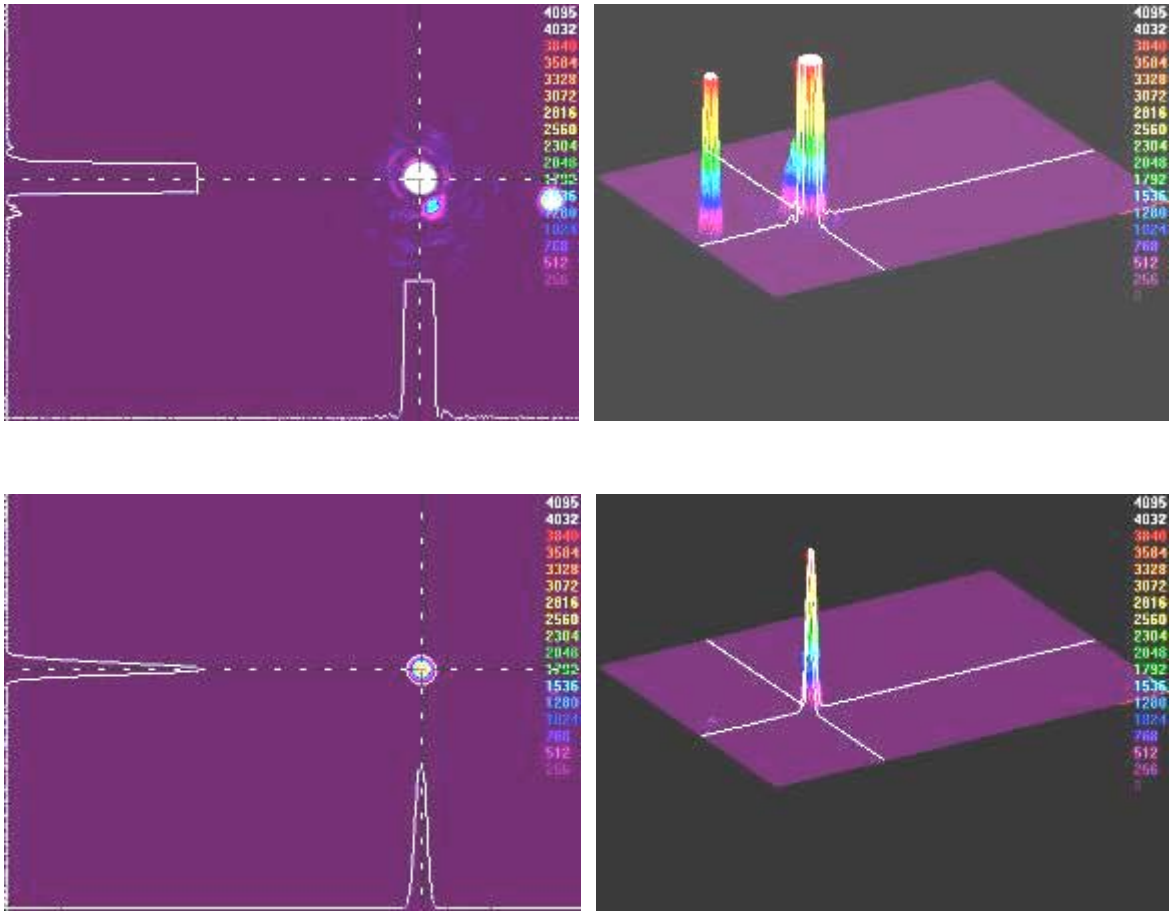

Figure 4.10 – First image from CCD -

4.1.4 The Optical Components and Features

The complete optical circuit is composed by the following components:

- 1 laser He/Ne low power (7mW approximately)
- 2 beam polarizer
- 1 Faraday rotator
- 1 mirror with incidence at 45°
- 2 microscope objective 5x
- 2 lenses
- 1 CCR
- 1 beam splitter
- 1 filter
- 1 CCD camera

Afterwards it's described the working and the features of the main devices which constitute the optical circuit:

Optical isolator

The Faraday rotator together with the two polarizers, placed before and after it, form the optical isolator. This device allows the laser beam passage in a single direction not allowing the return towards the source. In case the laser has a relatively low power, any beam return could cause a measurement trouble, while when the laser has a high power, the damaging of the laser could be caused.

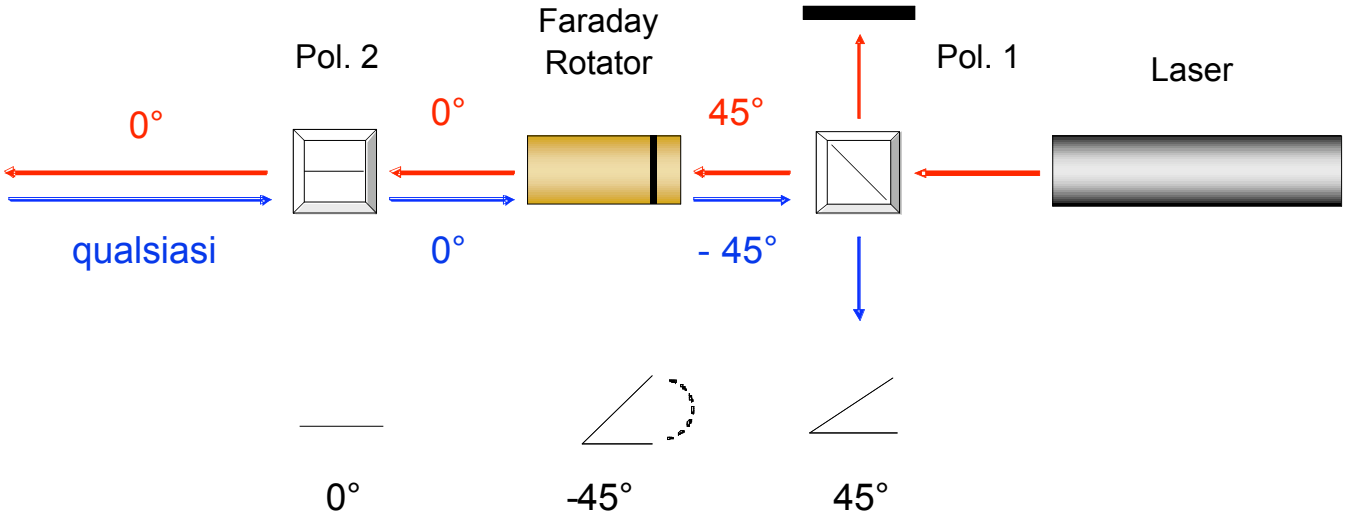

Figure 4.11 – Optical isolator scheme -

Referring to the figure 4.10, the outgoing beam has a linear polarization with a definite corner. This comes through the first polarizer which allows the 45° component passage with respect to the reference plane (parallel to the surface of the optical bench); then it is possible to regulate the power of the beam rotating the body of the laser around its axis opportunely. In this way, outgoing from the first polarizer the beam has a 45 degree polarization; now the laser meets Faraday rotator which rotate 45° the electrical field vector (and magnetic). The Faraday rotator is a magnetic cylinder with a vitreous core inside in which the laser beam comes in the direction of the magnetic induction lines. The rotation θ of the electrical field vector is proportional to the magnetic field value **B** and to the crossed thickness by C (Verdet constant) which is medium function:

$$\theta = C \cdot B \cdot t$$

Figure 4.12 – Optical isolator -

At this point, in the circuit, a second 45° inclined polarizer (respect to the first) allows the 45° component passage with respect to the table and then if the FR it is right aligned, the beam power must only lower of FR and polarizer attenuation factor.

Otherwise, the FR rotates the electrical field vector of a greater or lower angle of 45° and the out of plane component would be stopped from the polarizer with consequent beam power reduction.

Then, measuring the second polarizer outgoing power, is possible to align correctly the Faraday rotator (rotating its body).

Differently combining the polarizer and Faraday rotator position is possible to select the polarization of the electrical field vector outgoing from the second polarizer. In practice this operation will be made with a linear polarizer

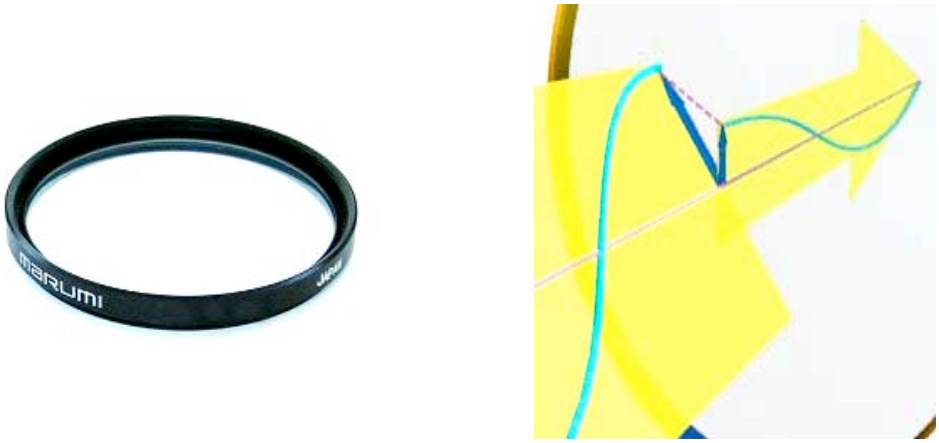

Figure 4.13 – Linear polarizer -

Beam expander/reducer

In order to obtain a beam expander/reducer two different devices will be used:

- Independent lens-objective system
- Telescope system

In both devices the work principle is the same: the incoming beam is expanded by the objective and then collimated by the lens. Switching the lens-objective relative position we obtain a device working reversed (as a reducer).

The objective has 5x expansion factor, so that the beam diameter arrives to 40 mm in order to cover all the surface of CCR. About the lenses, we have 2 types: one with 300mm and the other with 400mm. The first is mounted in beam reducer while the second one in beam expander. This difference does not change the device expansion (reduction) factor.

Figure 4.14 – Telescope beam expander -

Beam splitter

Material	UV grade fused silica
Diameter	76.2 mm
Thickness	12.45 mm
Diameter Tolerance	+0/-0.13 mm
Thickness Tolerance	±0.38 mm
Wedge	30 ±15 arc min
Beamsplitter S_1 Coating	R_S= 50% ±5%, $R_p \leq R_S$ at 45° over the specified wavelength range
Antireflection S_2 Coating	Multilayer coating, $R_{avg} \leq 0.75\%$ at 45° over the specified wavelength range

	over the specified wavelength range
Cleaning	Non-abrasive method, acetone or isopropyl alcohol on lens tissue

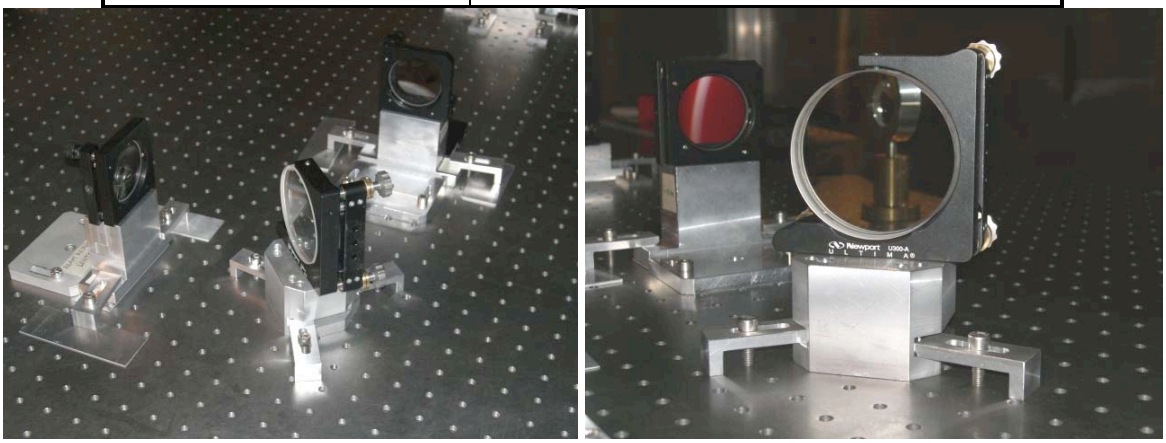

Figure 4.15 – Beam splitter –

The back surface is antireflection coated to prevent ghosting. A slight wedge in the substrate virtually eliminates internal fringes. S-polarized (orthogonal to the reference plane) beams will be equally split with R/T = 50/50 at 45° incidence.

A P-polarized (parallel to the reference plane) beam yields a split of R/T = 30/70.

In unpolarized light, the performance is typically R/T = 40/60.

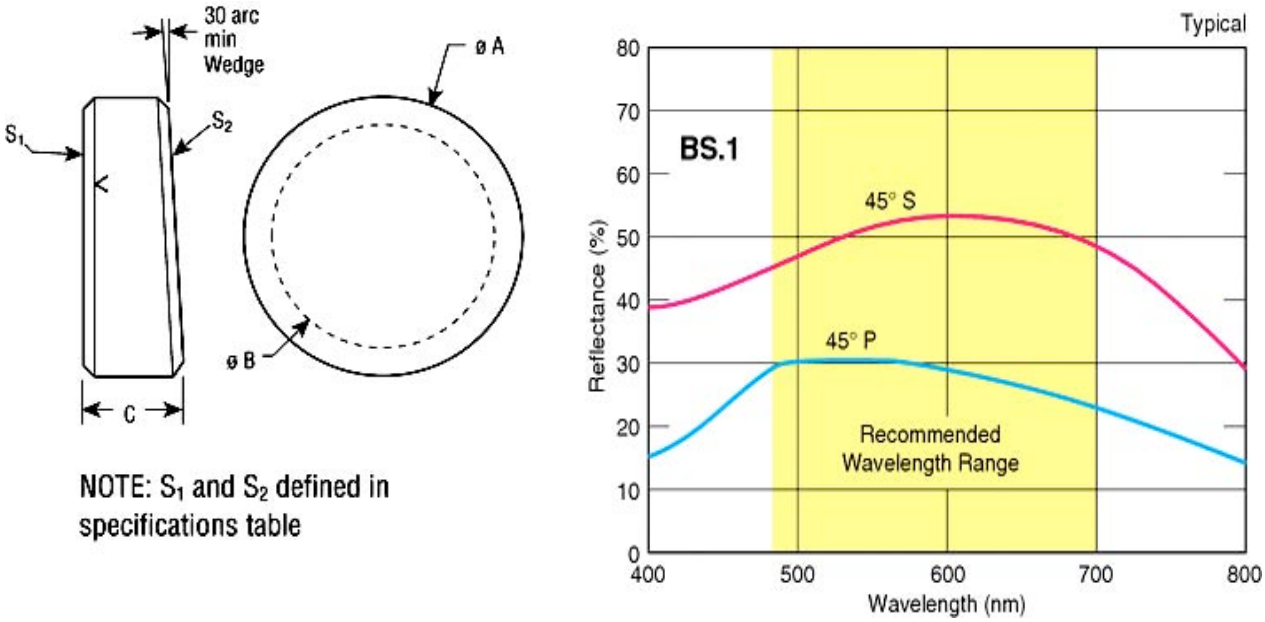

Figure 4.16 – Wedge angle; Wavelength range –

4.1.5 Alignment Procedure

The beam is defined aligned when the laser optical way, which hits the CCR, superimposes himself on what gets back to the source through the beam splitter (referring us to the figure 4.2, red way superimposed to the blue) and the altitude remains constant for all the optical way. In practice we want the laser beam path to remain on a plane assumed as a reference: the plane parallel to the optical bench but at 10 cm altitude. So that the beam keeps himself on this plane, we must verify that on every circuit component the incident and reflected beam is at constant altitude; in other words the reflection plane must be always superimposed on the reference one.

The beam must be aligned both to be able to define the optical axis and to realize the circuit equipped with beam expander and reducer.

The most critical components which needs micrometric regulations are the first mirror, beam expander/reducer and beam splitter: in particular the latter, having a wedge angle, thus the last circuit arm is not exactly parallel to the first with consequent misalignment of CCD camera, with respect to the ideal position.

The wedge angle involves that beam splitter has a univocal positioning on his mount in order to not introducing out plane components of the beam propagation vector.

In this phase turns out comfortable monitoring, by the second CCD camera, the beam outgoing from every component both to check the form and verify that the altitude remains constant for all the optical path, especially the beam splitter outgoing beam in order to assure his exact positioning on the mount.

We can summarize the alignment procedure as following:

1) Define horizontal optical axis with:

    - laser + faraday rotator + polarizers
    - 45deg mirror
    - Beam Splitter
        i. Due to wedge angle the beam transmitted is not parallel to the incident beam.
        ii. It must be positioned in such a way that the incident beam and the reflected have the same altitude (10 cm).
        iii. The side with the wedge angle (anti-reflective) must be turned outward the circuit.
    - CCR, as orthogonal to the beam as possible, NOT the flat mirror.
    - Reference (i.e. fixed and repeatable) position of the CCD
        iv. The beam from Splitter to CCD is NOT parallel to first circuit arm.
        v. This reference position is needed to check the alignment of the flat mirror when this is substituted in place of the CCR
    - Check that the reflected beam enters the faraday rotator backwards

- All the above is done with the diffraction pattern of the CCR, which can be have a geometry much less simple than the Gaussian shape of the narrow laser beam.
- For this reason, at the end of this step, replace the CCR with the flat mirror.

2) Alignment of the lens (we work with the flat mirror diffraction pattern now):

   - The lens of the expander arm is positioned so that the laser spot on the CCD does not move, checking for the spot still enters the faraday rotator backwards.
   - Same as above for the lens of the reducer arm.

3) Alignment of the microscope objective of the expander arm:

   - Position the focus of the objective in the focus of the lens such that:
     i. the expanded beam is collimated and parallel (check with a mirror)
     ii. the beam position on the CCD does not move

4) Alignment of the microscope objective of the reducer arm:

   - Same as above
     i. the reduced beam is collimated and parallel (check with a mirror)
     ii. same as above

4.2 The CCD as Laser Beam Profile Detector

4.2.1 Data Acquisition Software

The acquisition software is a LBA (Laser Beam Analyzer) provided from Spiricon Inc. model LBA-FW-SCOR http://www.spiricon.com/ . It provides all the essential features needed for laser beam analysis. Some of these features are:

- High-speed high-resolution false color beam intensity profile displays in 2D and 3D.
- Numerical beam profile analysis employing advanced patented calibration algorithms.
- User selectable choices for making beam width measurement
- Pass/fail testing available on most measured parameters.
- Both Whole beam and Linear Gaussian fits to beam data.
- Top Hat measurements based on the beam profile or a user defined area or line.
- Signal-to-noise ratio improvement through averaging and background subtraction.
- Frame summing for cumulative effect analysis.
- Statistical Analysis of all measured parameters.
- Beam Stability analysis.

- Histogram display and results.
- Post processing capabilities.
- Both Drawn and Auto Aperture for isolating beam data.
- Both Results and Data logging capabilities.
- Flexible printing options for hard copy generation.
- Two Divergence measurement techniques.

Exporting image to a disk file:

Exporting is an operation that is designed to take data and images out of the LBA-FW-SCOR and use them in other applications. Exports are a bad choice for data storage because there is no way to reload exported data into the LBA-FW-SCOR! Bitmaps for example, are one of the exporting options. Bitmaps (.bmp) are simply pictures of the beam image and do not represent a viable data source for numerical analysis. If the user desires to do some external computations on exported data, ASCII formats have been provided and are the only viable method for doing so.

Bitmap images will appear just as the current beam display window image appears. The two ASCII file types are .cma and .spa. The .cma type uses Comma delimited entries. The .spa type uses Space delimited entries. Spreadsheet programs like Excel and Lotus 123 typically use comma delimited data entries. Math programs like Mathcad typically use space-delimited formats. Consult your application program to determine which style to use.

We can also save 1D beam display images that are defined by the location of the Horizontal and Vertical Cursors. Cursor files are designated with a .cur file type. Cursor files are ASCII files that use Comma delimited entries.

The Cursor image is organized 21 Horizontal data first, left to right, followed by a carriage return, and then the Vertical data, top to bottom.

We can also save a Column and Row summed beam image that is defined by the total of all pixel values summed in both the Horizontal and the Vertical direction. Column/Row summed files are designated with a .sum file type. Summed files are ASCII files that use Comma delimited entries. The Summed image is organized Horizontal data first, left to right, followed by a carriage return, and then the Vertical data, top to bottom.

4.2.2 Power Meter Calibration

The available power meters are 3 with double full-scale of 100 μW e 1 mW. These are equipped with a sensor which receives in input the spot providing in output a tension which can be shown on

the display of the connected voltmeter. Performing the calibration operations is possible to transpose the tension signal in power values (Watt) through a linear type relation obtained considering some average values for the 3 power meters:

$$y = 19x \quad \text{(full-scale 100 } \mu\text{W)}$$

$$y = 180x \quad \text{(full-scale 1 mW)}$$

The first is equipped with a band-pass filter in order to stop the environment light (max 1 μW).

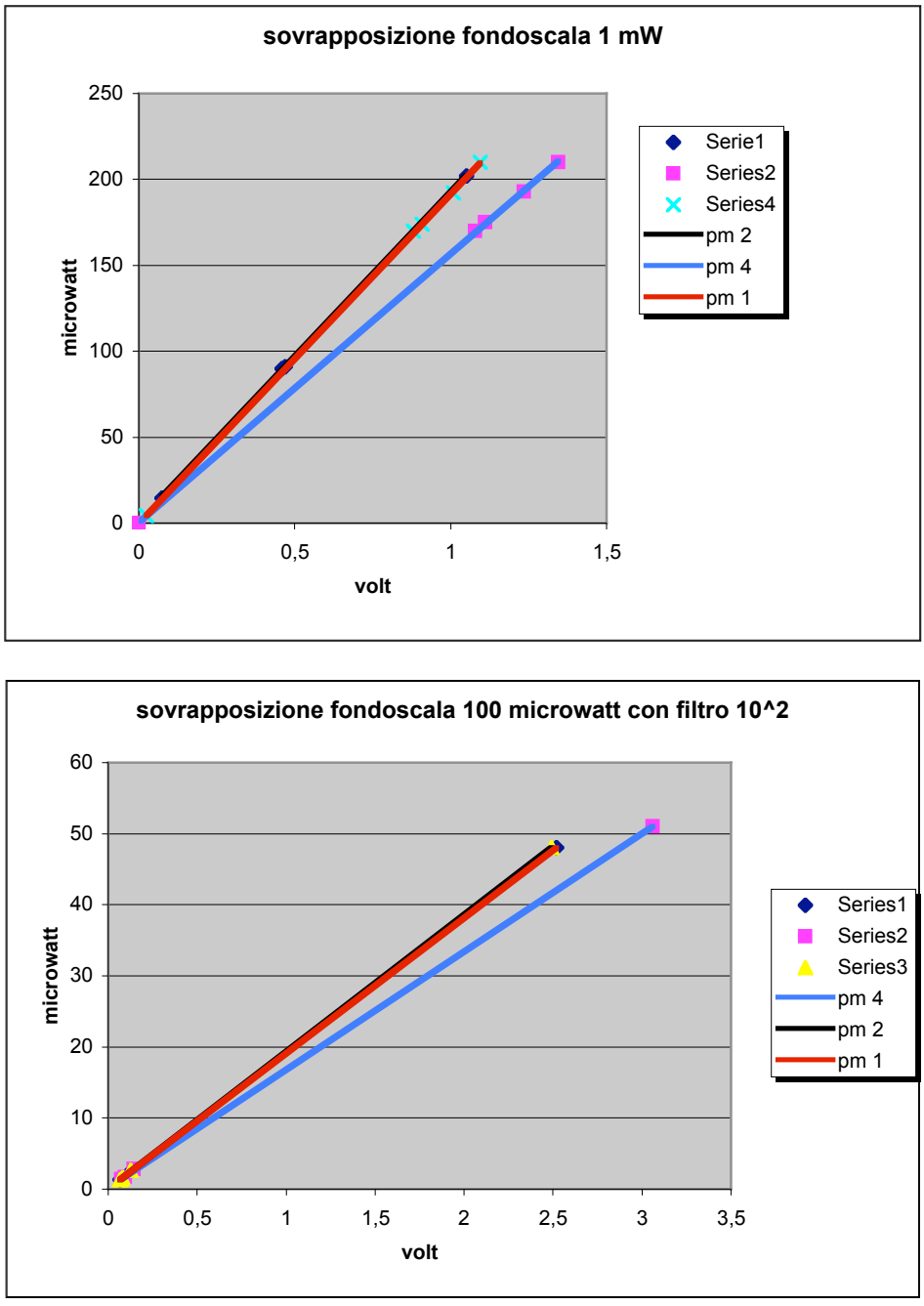

Figure 4.17 – Power meter calibration.

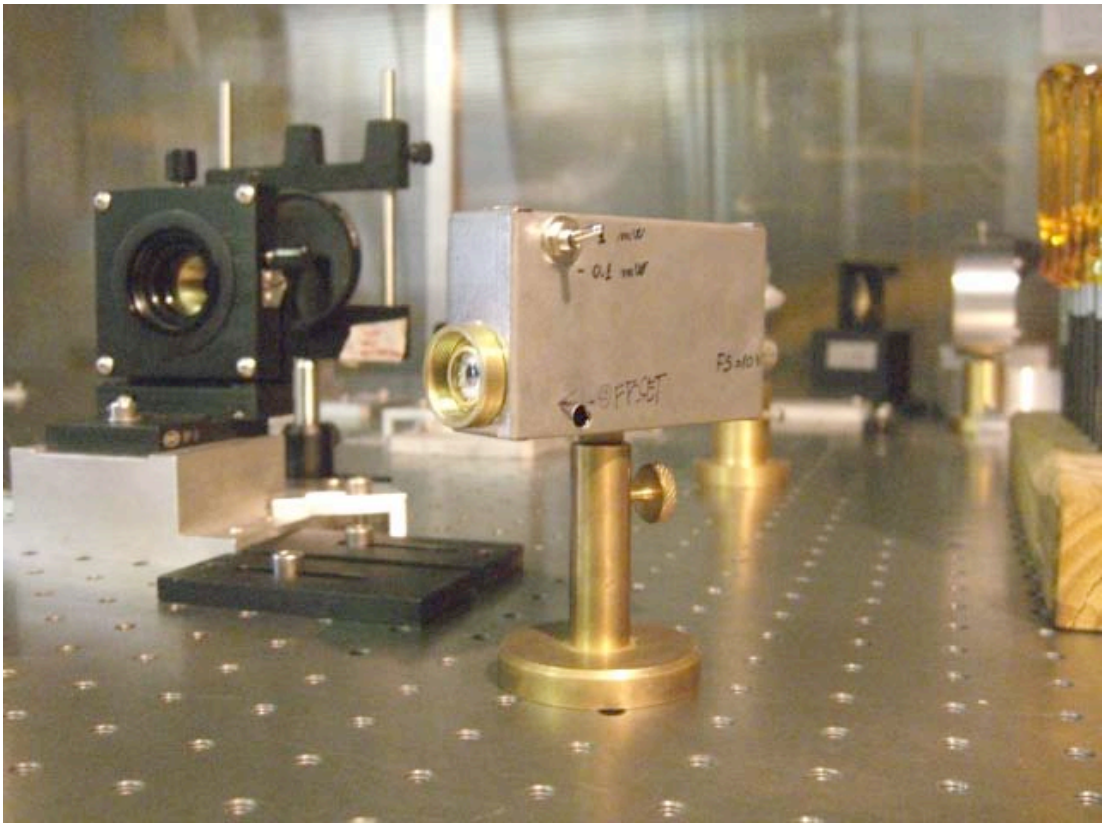

Figure 4.18 – Power meters -

4.3 Experimental Results

4.3.1 Shape of CCR Far Field Diffraction Pattern

With no dihedral angle offset the shape of CCR has an intensity central peak with six secondary spots around. Introducing the angle offset the energy shifts from the main lobe to the secondary ones, and the FFDP, increases its size changing shape.

This behavior allow receiving station to compensate the velocity aberration and to receive the satellite retro-reflected signal: the main goal is to move most of the energy in a ring equal to velocity aberration.

The velocity aberration grows with the satellite orbital velocity: the lower the satellite altitude the larger the necessary offset angle (see chap.3)

The velocity aberration of LAGEOS (h=6000 km) is about 36 μrad, corresponding to 200 m to the ground. In order to compensate the velocity aberration the angle offset is about 1.25 arcsec. The manufacturing accuracy is typically 0.5 arcsec.

Instead, for LARES (h=1200 km), we will use a larger angle offset of 46 μrad, corresponding to 54 m on the ground.

In the optical bench we use CCRs similar to the LAGEOS ones but with higher than usual angle offset tolerance: 1.25 +/- 2.

In principle, after the angular calibration is completed, will be possible to establish what part of the CCD sensor will contain most of the FFDP (specific to a given CCR) and then, from the comparison with the simulations, we can identify the angle offset of a given CCR.

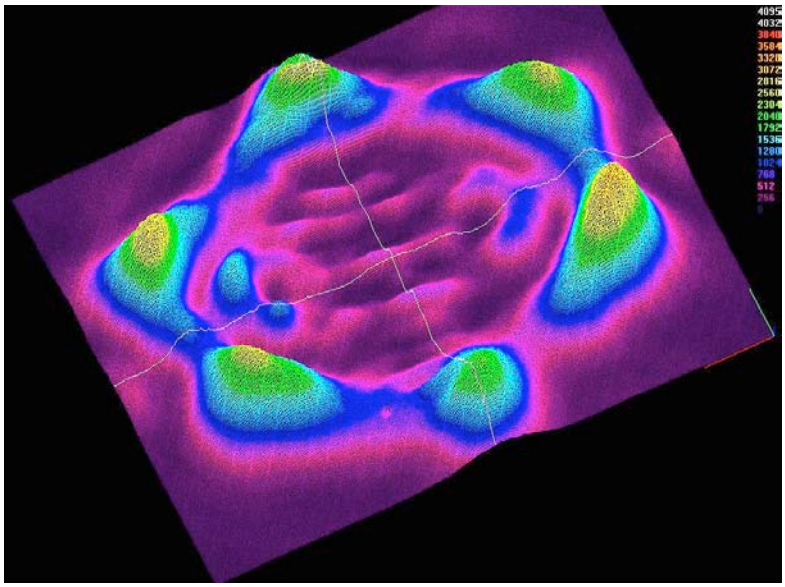

Figure 4.19 – FFDP of CCR (3D zoom) -

4.3.2 Flat Mirror Normalization

The absolute cross section of a cube corner can be measured in the laboratory by comparison with a reference mirror. If the reference mirror has high optical quality and known reflectivity its absolute cross section can be computed theoretically. For example, the diffraction pattern of a circular optically flat mirror is the well known Airy pattern.

The absolute cross section of a cube corner can be determined by measuring the diffraction pattern of both the mirror and the cube corner without changing any of the settings in the measuring equipment. The ratio of the signal from the cube corner to the signal from the reference mirror gives the absolute cross section of the cube corner.

The absolute cross section of a retroreflector can be determined by comparison with a circular reference mirror of known diameter and reflectivity. Dielectric mirrors have a reflectivity close to 100 percent. In order to compare the intensity of the cube corner and reference mirror the two images should be taken at the same intensity scale.

The cross section *c* at the center of the diffraction pattern of a perfect reflector (flat phase front) in standard units is:

$$c = 4\pi \cdot \left(\frac{A}{\lambda}\right)^2$$

where *A* is the area of the reflector and is the wavelength. The area of a circle of diameter .0271 meters is .0005768 sq meters. With = 532 nm the cross section at the center of the diffraction pattern is 14.77 million sq meters with no reflection losses.

For a solid fused silica cube corner with index of refraction 1.46 the Fresnel reflection losses at the front face on entering and leaving the front face reduce the intensity by about a factor of .93.

For the uncoated LAGEOS cubes there are no reflection losses because they operate by total internal reflection. For the LAGEOS cube corners the diameter is 38 millimeters (1.5 inches). The area is .00113 sq meters. With = 532 nm the cross section at the center of the diffraction pattern is 57.1 million sq meters with no reflection losses and no polarization effects.

For an uncoated cube corner the intensity of the central peak is reduced by about a factor of 4 relative to the Airy peak because of polarization effect on total internal reflection. This brings the peak down to about 57.1/4 = 14 million sq meters.

Dihedral angle offsets further reduce the energy of the central peak. These patterns are normalized to unity at the center of the Airy pattern. In other words they are in units of equation 1. After each diffraction pattern there is a line listing the maximum intensity of each polarization component

(Ymax and Zmax) and the maximum intensity of the total energy (Fmax); Fmax is not necessarily Ymax + Zmax since the maximums of the two polarization components can occur in different places in the pattern. In the last pattern below for a LAGEOS cube corner with a 1.25 arcsecond dihedral angle offset the intensity is .05 times the Airy peak. Since the Airy peak is 57.1 million sq meters this is 2.9 million sq meters for an ideal CCR with three angle offsets of exactly 1.25 arcsec [14].

Uncoated, 1.25 arcsec dihedral angle offset, Liner vertical polarization

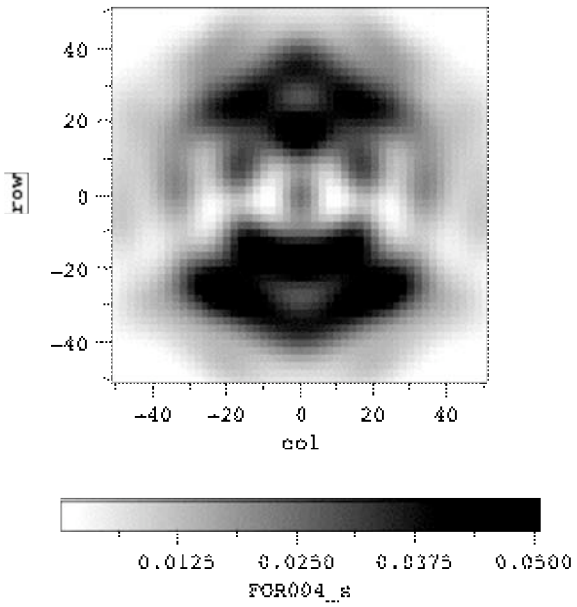

Figure 4.20 – Linear vertical polarization -

Ymax (vert): 0.05028194

Zmax (hor): 0.02842546

Fmax : 0.05059002

4.3.3 Angular Calibration

The size of the "raw "experimental CCR pattern and of its detailed geometric features is given as numbers of CCD physical pixel with laser energy above a certain threshold. In order to compare the size of the pattern with the expected value of the velocity aberration angle needed for LARES (~ 46 μrad), we have to perform a calibration which relates the intrinsic angular divergence of the CCR diffraction pattern with the physical pixel distance of well defined and separated optical signals on the CCD.

For this purpose we can use 2 slits between the beam splitter and the beam reducer in order to create an interference pattern with well-known divergence angle.

The diffraction phenomena is due to obstacles along the wave front path: when such obstacles are endowed with aperture, generally with different shapes but smaller than beam cross-section, the wave fronts pass through them becoming limited in space generating a particular intensity distribution.

In scientific literature exist two models to describe the behavior of this phenomenon:

- Fresnel's diffraction
- Fraunhofer's diffraction

The Fresnel model is characteristic of those situations in which the source and the observation screen are at finite distance from obstacle. The mathematic treatment of this problem is rather complex.

Generally it is very interesting, for the applications in optic equipment and particularly in our case, when we can consider infinite the source-obstacle distance compared to the obstacle-observation plane one. In this way the obstacle is invested from waves plains: this is a Fraunhofer diffraction.

To explain the phenomenon of the diffraction we do reference to the following figure, where it is present a slit of width *d* and supposed infinitely long in the sheet perpendicular direction:

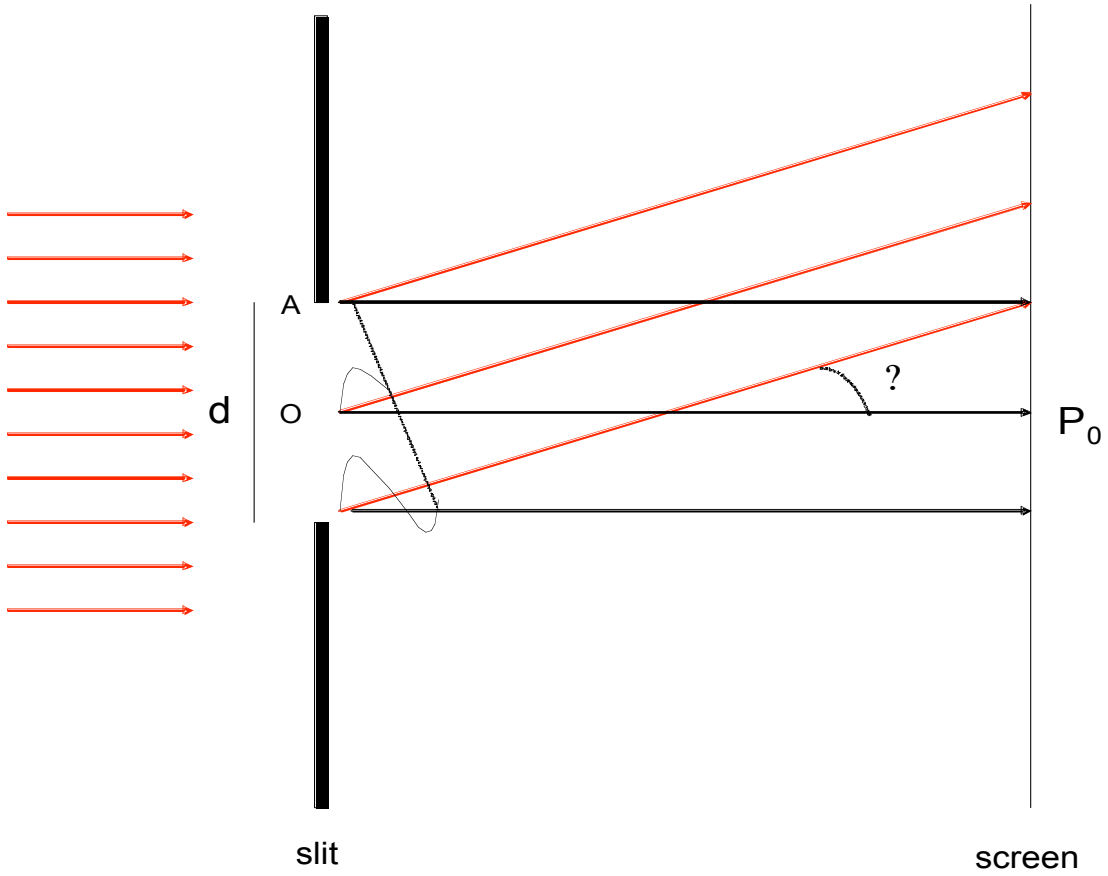

Figure 4.21 – Diffraction generation -

All the waves starting from slits are emitted in phase, and since they travel the same distance, they arrive in P_0 in phase. In this case the interference is constructive and the intensity is greatest.

In P_1 the ray coming from A and O are in phase opposition giving worthless contribution; the same happens for the rays coming from couples points of the slits that are in the same distance from the point above mentioned. We conclude that the interference of all the waves coming from all the points of the slit arriving in P_1 is zero. The same happens for all the points on the screen having parallels rays on coming and direction such as the path difference between the rays coming from the extreme of the slit is equal to a multiple integer of λ (wave length).

Therefore we have an alternating pattern given by destructive, constructive and intermediate values (different values from $n\lambda$) of interference.

The intensity is given by:

$$J(\alpha) = J_0 \frac{sen^2\alpha}{\alpha^2} \quad \text{with} \quad \alpha = \frac{\pi \cdot d}{\lambda} sen\theta$$

Graphically:

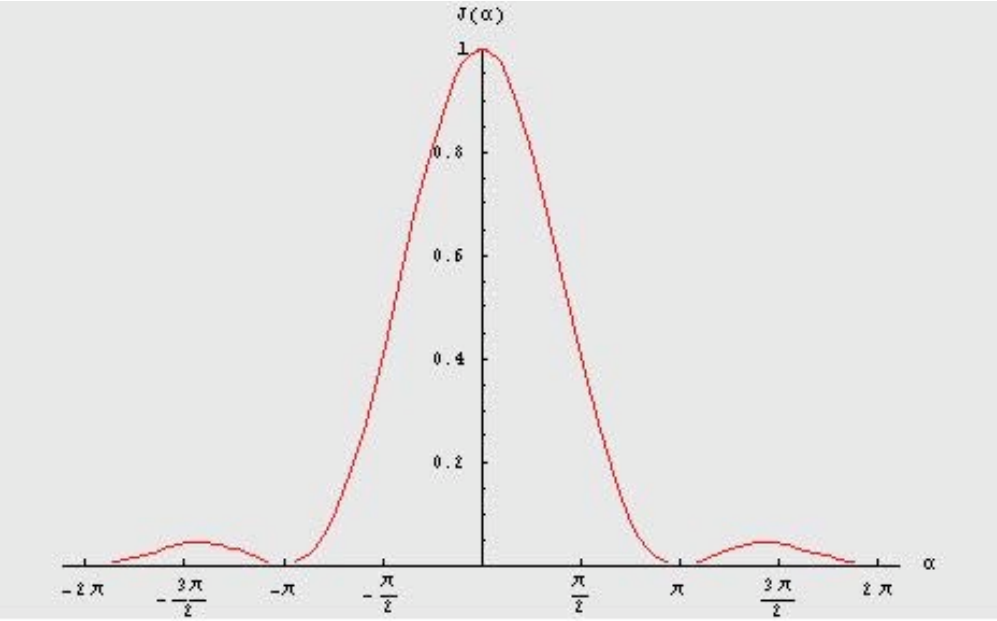

Figure 4.22 – Diffraction profile -

We have the maximum intensity for $\alpha = 0$ (in P_0 on the screen). For this particular value, we have ($sen\alpha / \alpha) = 1$ and therefore $J = J_0$.

Close to the central fringe there are symmetrically ones with quickly decreasing intensity: we have disruption zero for $\alpha = n\pi$, while the secondary points of maximum do not coincide exactly with $\frac{3}{2}\pi + k\pi$ but they are moved towards the ordinates axis, that is to say towards the central fringe (*1.43π, 2.46π, 3.47π,...*):

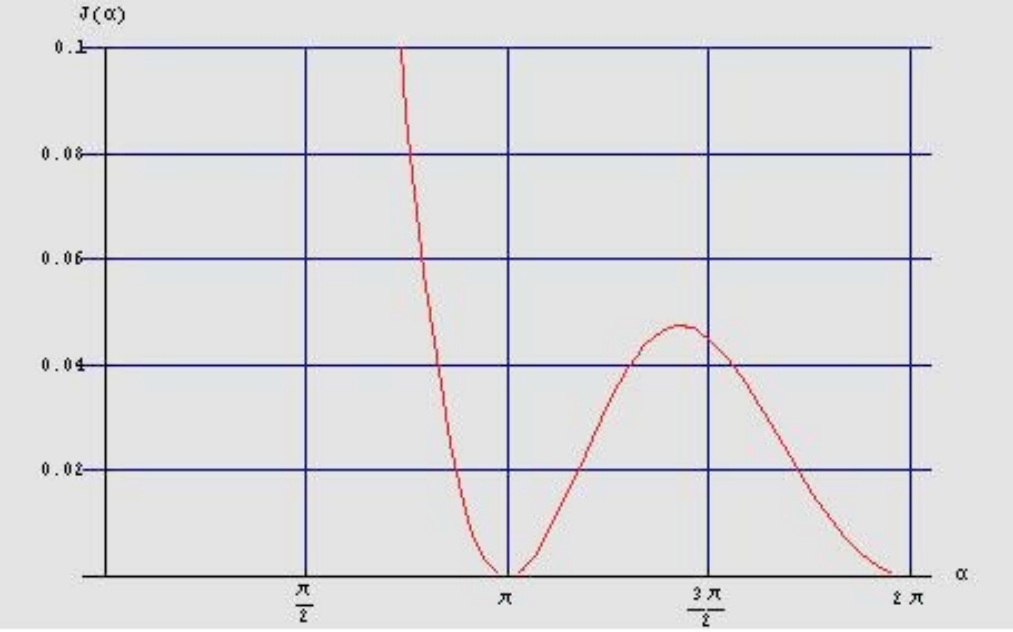

Figure 4.23 – Diffraction profile detail -

it is well to note that the straight line directions joining the slits center with the points on the screen where we have the first minimum form with axis of the disposition an angle:

$$\theta = \frac{\lambda}{d}$$

For our purpose we want the diffraction figure main lobe to be contained in CCD sensor:

$$\Delta x = \theta \cdot a = \frac{\lambda}{d} a$$

$$\Rightarrow d = \frac{\lambda}{\Delta x} \cdot a$$

where a is the distance between slits and CCD sensor.

If we assume $\Delta x = 3\text{mm}$ and $d = 500\text{mm} \Rightarrow d = 100\ \mu\text{m}$.

In the case of double slit we have a different course of intensity respect to the previous case:

$$J(\alpha) = 4J_0 \frac{sen^2\alpha}{\alpha^2} \cdot \cos\beta \qquad \text{with} \qquad \beta = \frac{\pi \cdot e}{\lambda} sen\vartheta^{INT}$$

Where e is the distance between the slits and ϑ^{INT} the interference divergence.

The intensity distribution is represented by two factors that commonly are indicated as *diffraction factor* and *interference factor*.

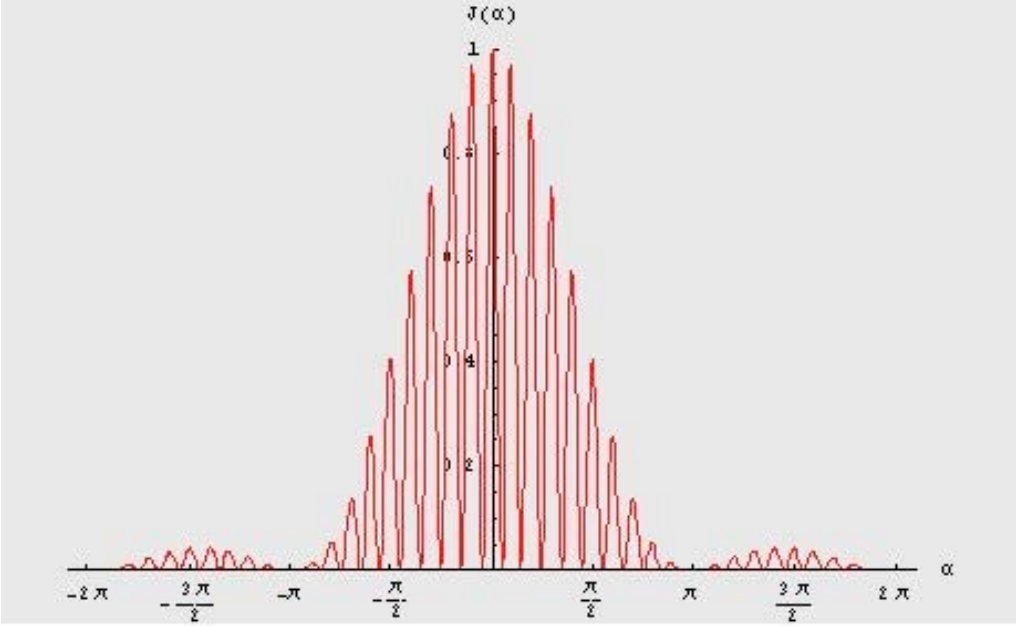

Figure 4.24 – Diffraction and interference profile with $d = d_1$ -

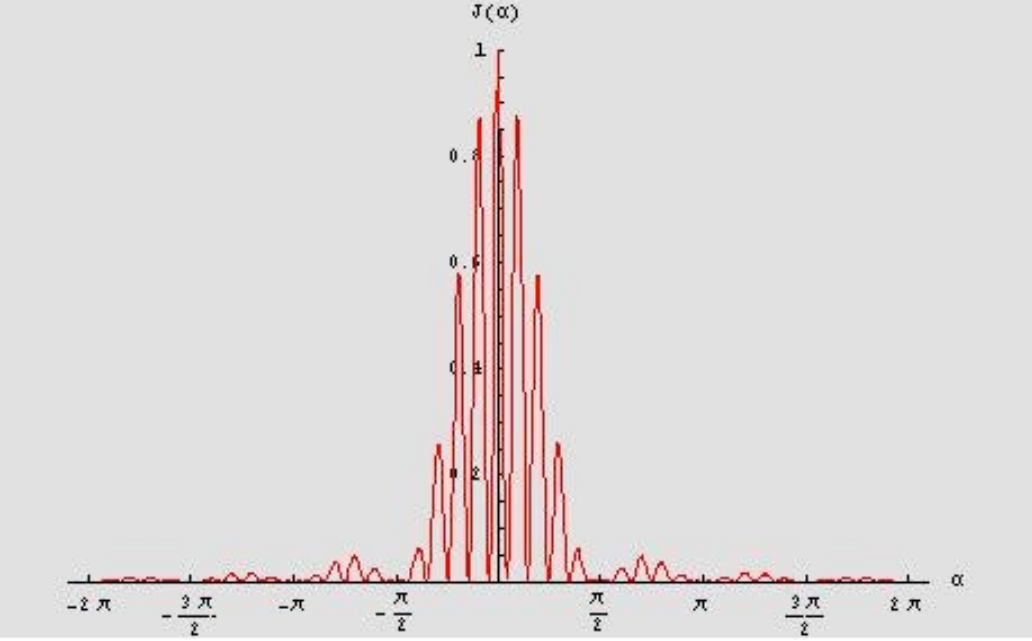

Figure 4.25 – Diffraction and interference profile with $d = d_2$ -

The 2 figures above refer to 2 couples of slits that differ in dimensions ($d_1 < d_2$) but not in distance. The zero position point, and therefore the fringes one, depends (aside by λ) exclusively from *e* and therefore it does not change with slits thickness (*d*) remaining *e* constant.

The thickness (*d)* have influence only on diffraction factor.

Now we want the interference to be visible from the sensor, so the fringes distance must be at least some pixels (i.e. 100 pixels). In this case we have:

$$\Delta x_{pixel} = \vartheta^{INT} \cdot a = \frac{\lambda}{e} a$$

$$\Rightarrow e = \frac{\lambda}{\Delta x_{pixel}} \cdot a$$

$$\Rightarrow e = 0.5mm$$

At present, the calibration has not been realized yet because the chosen vendor did not deliver the necessary 2 slit mask.

4.3.3 FFDP Dependence on Laser Polarization

We have seen that using an angle offset it is possible to put energy at a larger radius than the six spots, but the diffraction pattern becomes complicated and not very regular. It will be different for each input polarization state.

If the dihedral angle is greater than 90°, the energy for linear polarization will be mostly aligned with the electric polarization vector in an uncoated cube. Instead, if the dihedral angle is less than 90°, the energy will be mostly perpendicular to the polarization vector.

In our case the dihedral angle offset is always greater than 90°, so the energy will follow the polarization vector.

In the optical circuit the polarizer vector is parallel to reference plane (at his time parallel to optical bench). We could rotate the polarization vector using the first and second polarizer but is more comfortable rotate the CCR starting to well-known position.

Conventionally, we assume 0° when the edge of CCR is perpendicular to the optical bench as shown in the following figure:

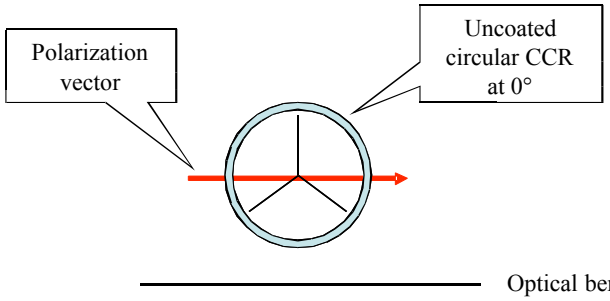

Figure 4.26 - Polarization-CCR relative position -

The experimental result that following shown as the FFDP shape changing with the polarization state starting from $\phi = 0°$ and arriving to $\phi = 315°$ with 45° steps in anticlockwise direction:

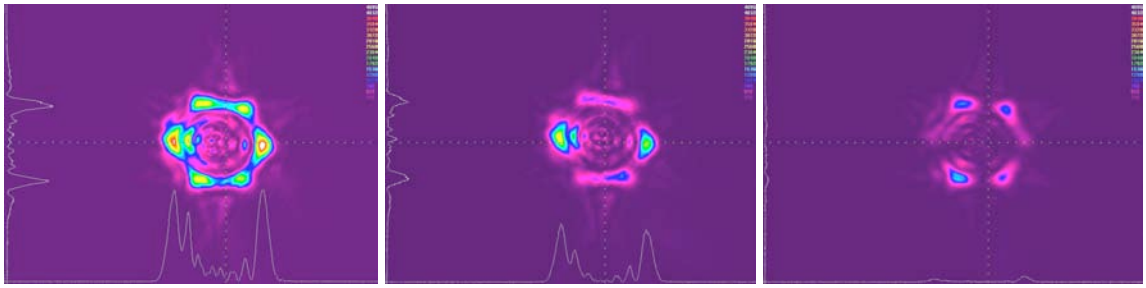

ϕ =0° tot *ϕ =0° hor* *ϕ =0° ver*

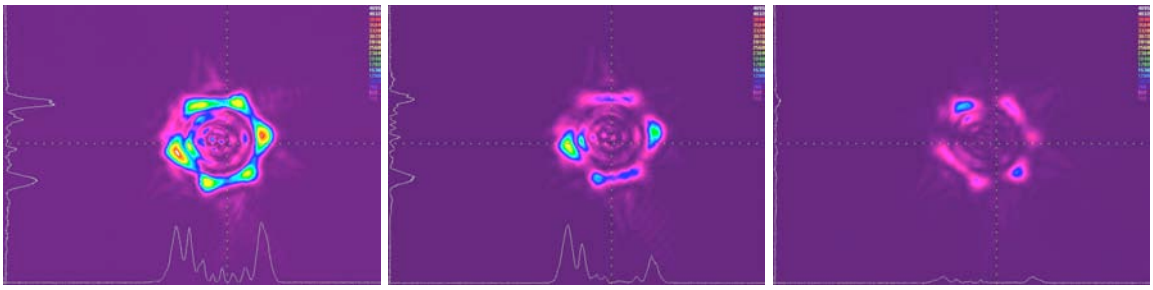

ϕ =45° tot *ϕ =45° hor* *ϕ =45° ver*

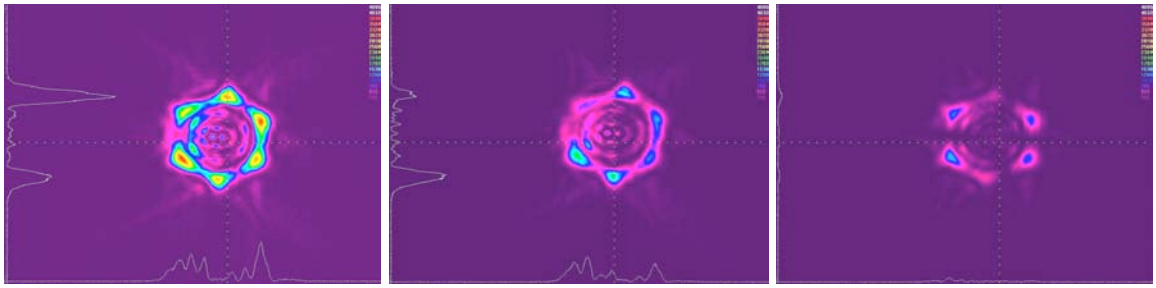

ϕ =90° tot *ϕ =90° hor* *ϕ =90° ver*

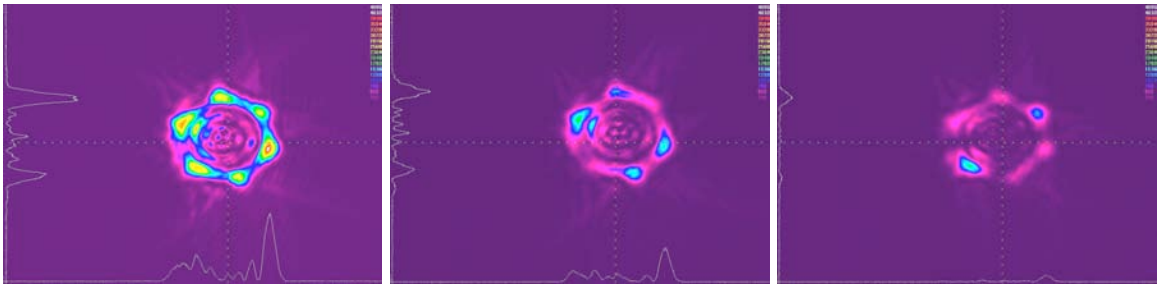

ϕ =135° tot *ϕ =135° hor* *ϕ =135° ver*

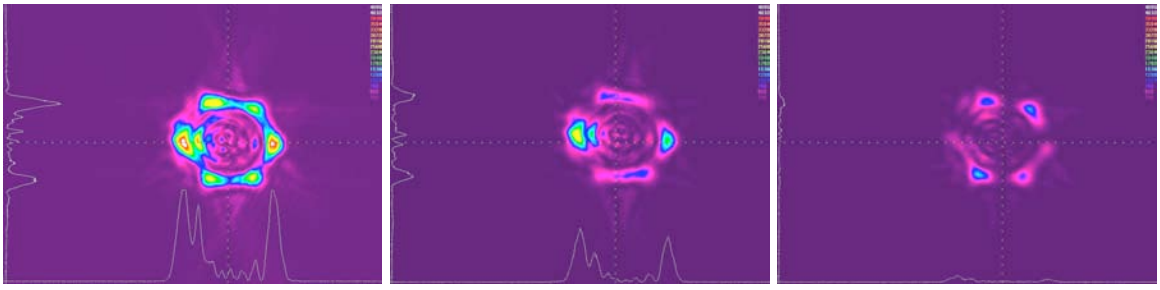

ϕ =180° tot *ϕ =180° hor* *ϕ =180° ver*

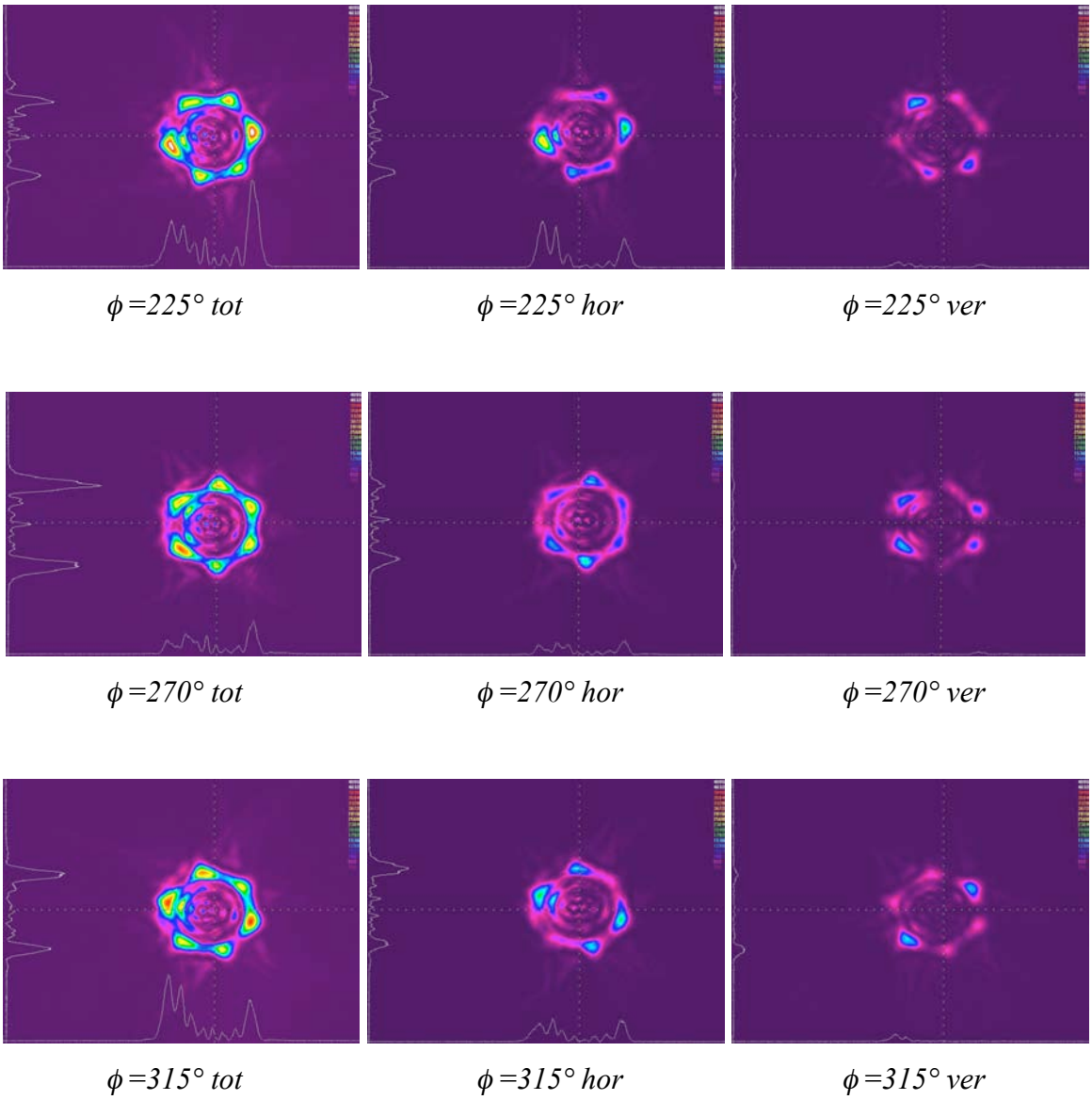

Figure 4.27 – Dependence on polarization –

We observe that the rotation of polarization confirm the theory and the simulation.

4.3.5 FFDP Dependence on Laser Incidence Angle

As mentioned, the CCRs reflecting reflect an incoming light beam back in the direction it came from: this is true only if the spotlight entry with a certain incidence angle range.

This range depends from how the CCR is struck; in fact, being an asymmetric object, it has an asymmetric behaviour changing its position with respect to a fixed incident angle.

Theoretically, if it turn approaching one of the edge to the light source we have retro-reflection, and then total internal reflection, if the incident angle is smaller than 17°, instead if one of the edge drift away from the source we can arrive thin to 50°.

Because of the mechanical characteristic of the CCR mount, the starting position of the CCR in this experimental measurements is $\phi = 90°$ and we turn away one of the edges from laser beam by steps of $\eta = 5°$ or 10°.

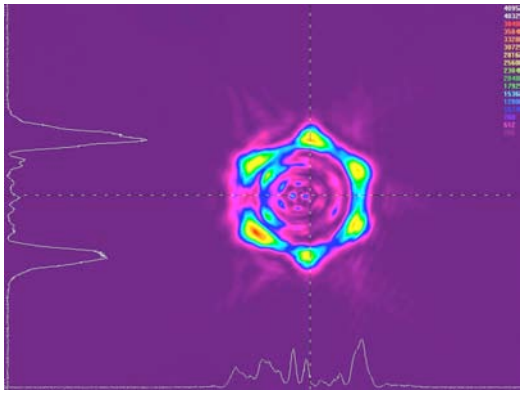

η= 0°

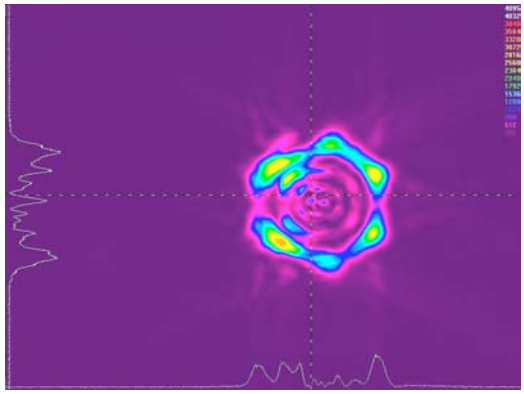

η=-10°

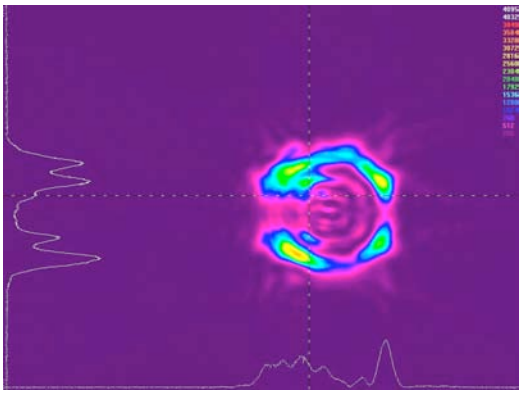

η= -20°

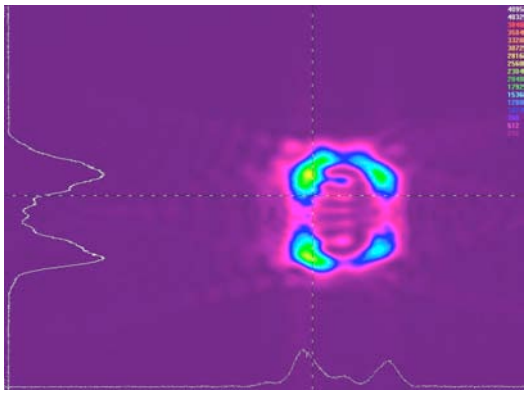

η= -30°

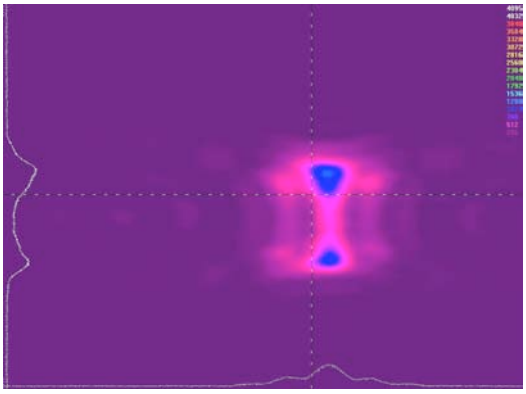

η= -40°

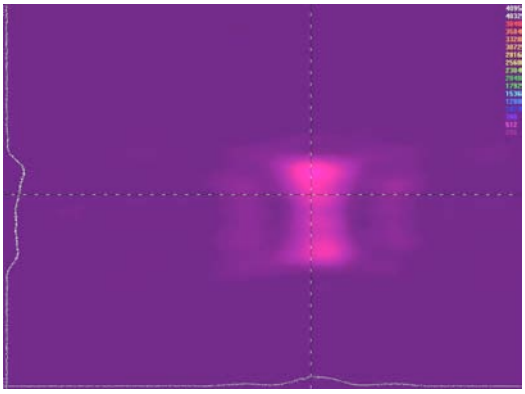

η= -42.5°

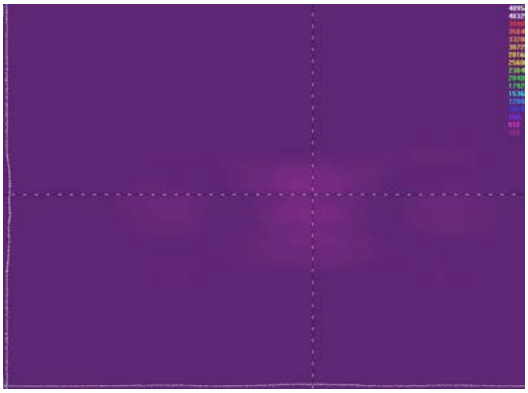

η= -45°

In the other direction, approaching the edge to the laser beam, but in others conditions (filters and objective):

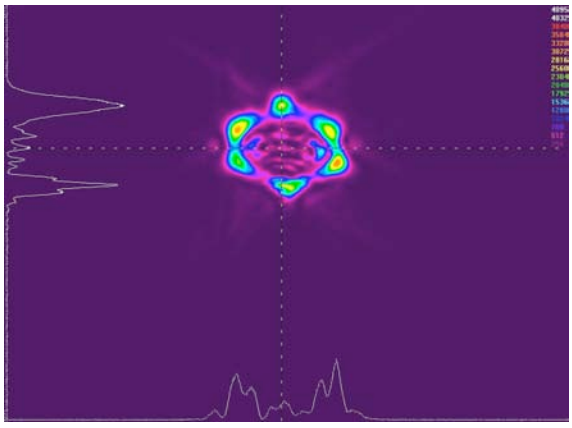

η= 5°

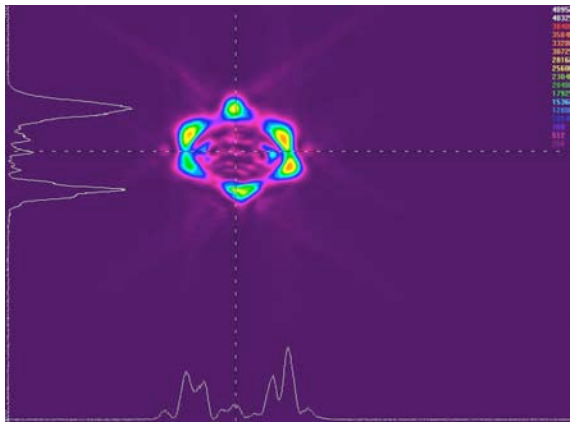

η=10°

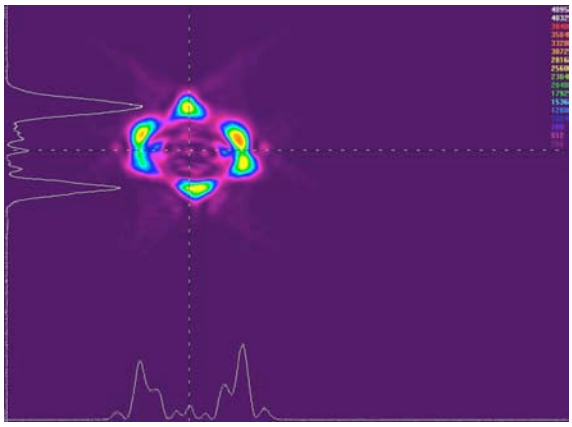

η= 15°

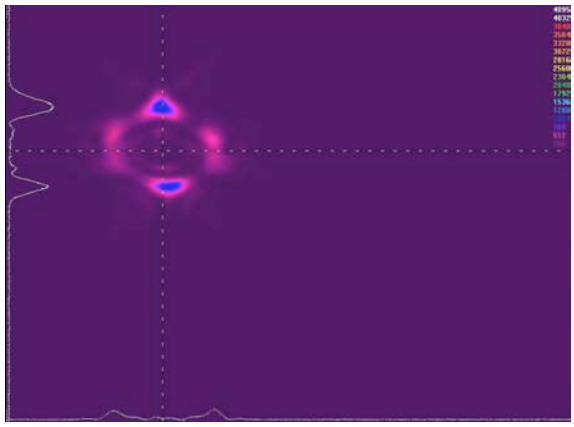

η=20°

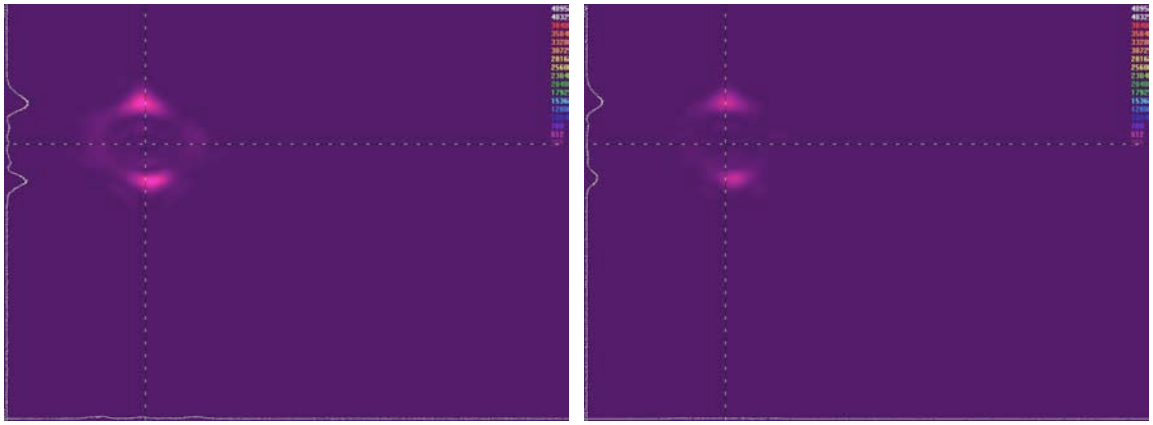

η= 25° η=30°

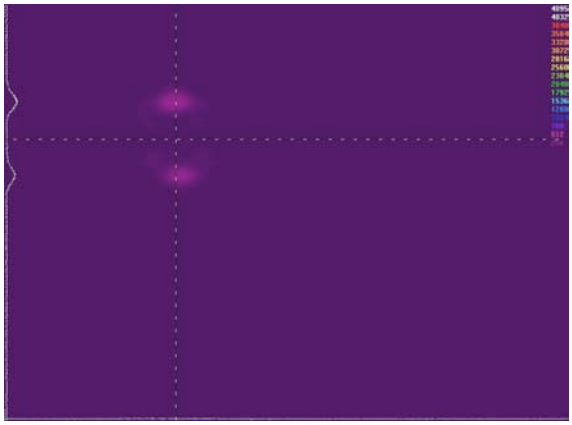

η= 35°

Figure 4.28 – Dependence on incidence angle –

The experimental behaviour is not the theoretical same one. In fact when the edge approaching to the source we have reflection until 35° (theoretically 17°), while in other direction until to 45° (theoretically 50°).

Probably this depends from the misalignment or from surface low quality near the CCR border. Besides also in theory is predicted a small reflection beyond the total internal reflection, faint Fresnel reflection (4 %). However, is not very easy to understand where total internal reflection (TIR) finishes and the Fresnel reflection begins.

4.4 Comparison of Simulations and Experimental Measurements

The CCRs tested on the optic circuit have a angle offset tolerance quite high. The reason is only financial: this CCR has been realized to be able to make thermal measurements in the space climatic facility (SCF) and for these the offset tolerance is not a critical parameter (see chap.5). On the

optical circuit we have tested 9 such CCR, whose optic behaviour turned out not to be the same. To compare the experimental measurements with the numerical simulations the CCR with features less distant from nominal ones has been chosen. Waiting for the angular calibration we can make only qualitative comparisons, because we don't know the size of the experimental FFDP in μrad. We can only deduce it from the shape comparison with simulation. From qualitative comparison with the Code V simulations, we can assign to the tested CCR an angle offset of 2.25 arcsec. This value is compatible with the expected tolerance and it would have the 66 μrad divergence velocity aberration angle in Code V. This value is twice the value of LAGEOS velocity aberration.

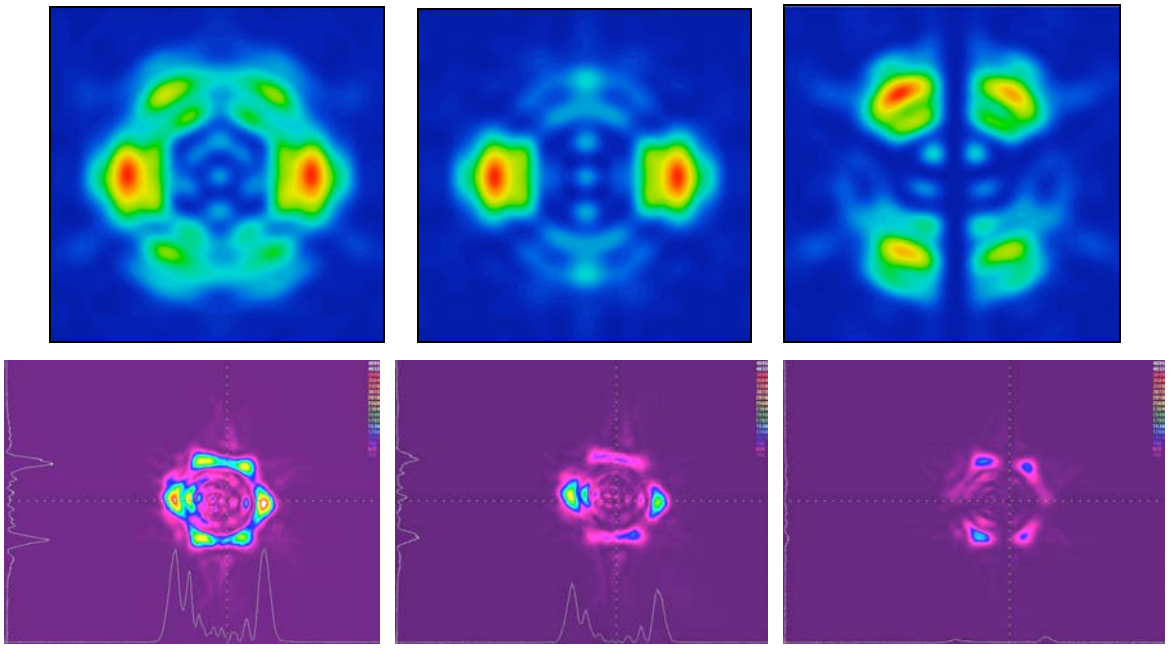

Figure 4.29 – Comparison simulated and experimental pattern –

In the simulated pattern we have 2.25 arcsec dihedral offset and horizontal polarization (like on the optical circuit) and the grid dimension of ± 150 μrad. The differences between the experimental and simulated pattern is due to two principal reason: first, the three CCR offset can be different whereas the numerical simulation have no tolerance. Second, the optical circuit can bring some imperfection to the pattern due to residual misalignments and "near field" effect.

4.4.1 Consideration about LARES

With an altitude of 1200 km, LARES will have a velocity aberration about 46 μrad. From numerical simulations obtained with Code V we deduce that the angle offset necessary to correct for the velocity aberration is about 1.5 / 1.75 arcsec.

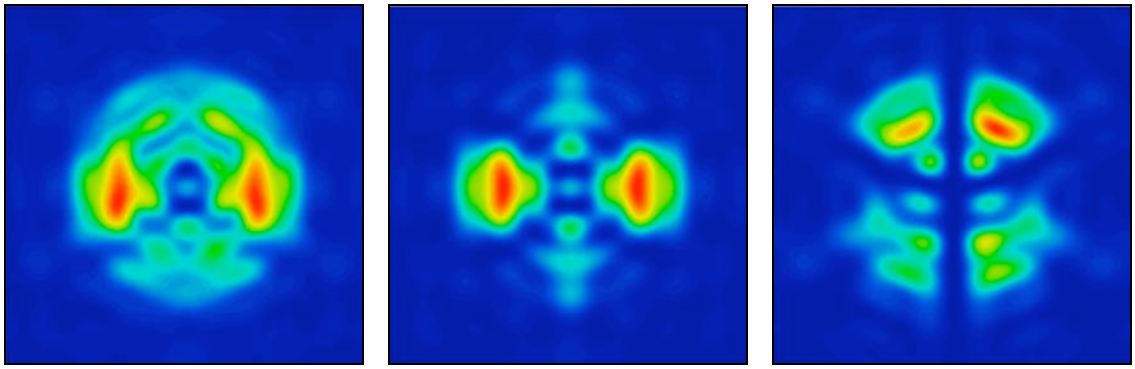

Total Energy Parallel component Orthogonal component

Figure 4.30 – CCR with 1.75 angle offset -

This choice of the exact value is very critical for many reasons:

The offset can be chosen in different ways depending on what criterion is used.

For example, when a satellite is at culmination is has the maximum velocity aberration because the satellite and station velocity vector are parallel. However the pattern on ground is larger so we can have larger offset angle. Instead, when the satellite is on the horizon the velocity aberration is smaller so it would be comfortable to have a larger angle offset. If the objective is to have the largest cross section when the distance is greatest it might be better to have a lower beam spread. The other factor is the geometry of the array. The cross section has to be computed for the whole array. The cube corners at larger incidence angles have a wider beam spread than those at normal incidence; thus we can have a lower offset because the CCR at larger incident contribute to widen the pattern.

For LAGEOS the optimum angle is between 1.25 and 1.50 arcsec. The value of 1.25 was chosen to keep the offset on the low side. Generally for low earth orbit the optimum angle is around 1.75 arcsec. Therefore the best angle for LARES is going to be between 1.5 and 1.75 arcsec and should probably be closer to 1.5 arcsec. Since the manufacturing tolerance is +/- 0.50 arcsec there is going to be a spread of values regardless of what specification is used. Fig. 4.30 summarize the values of the velocity aberration for LAGEOS, LARES, and the experimental qualitative measurement.

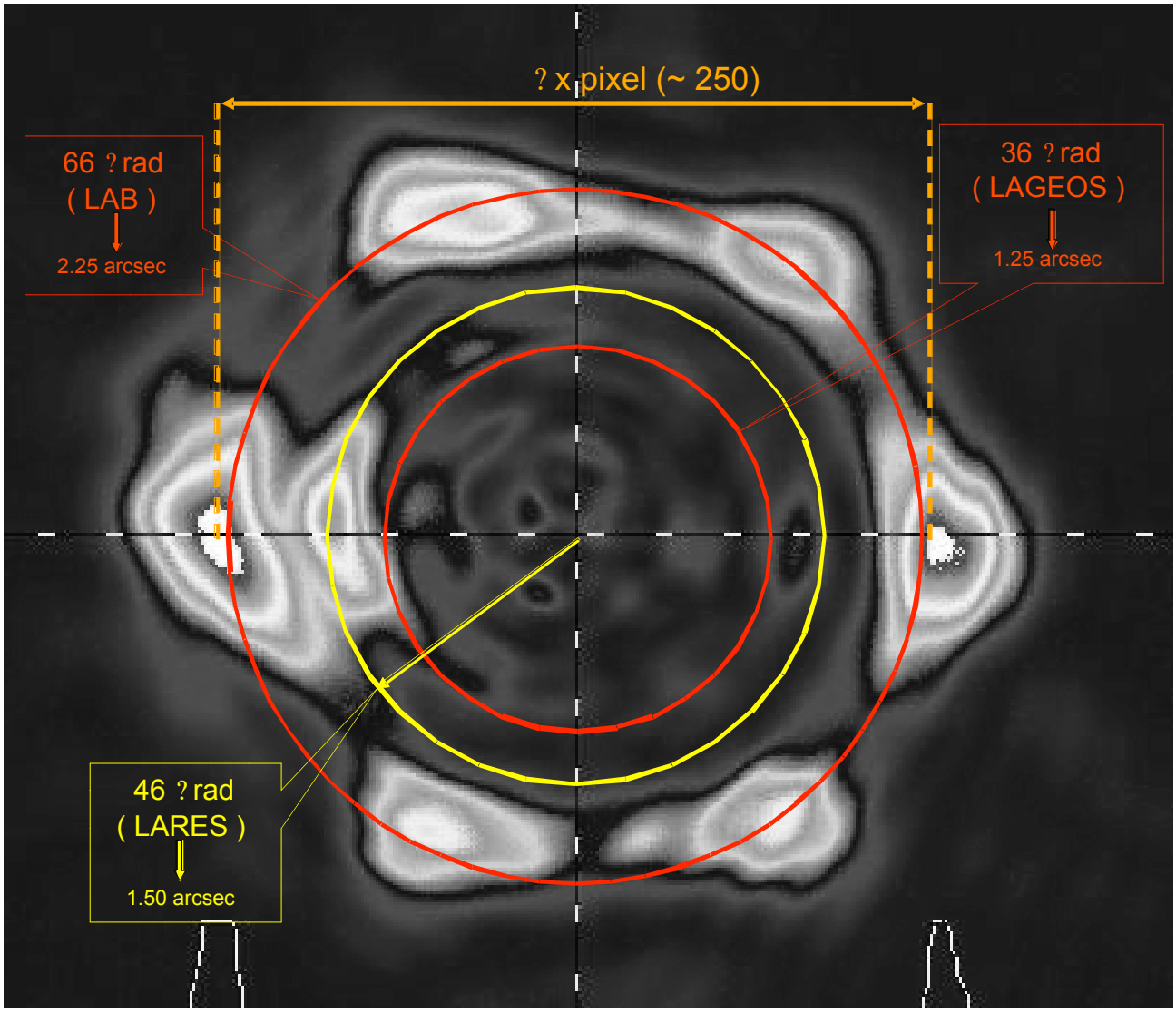

Figure 4.31 – Velocity aberration comparison on experimental pattern –

4.5 Importance of FFDPs in the LARES Acceptance Tests

When the LARES CCRs will be realized, we will test them on the optical bench, in order to evaluate:

- that their calibrated angle offset is compatible with the nominal value (1.50 arcsec) within the 0.5 arcsec tolerance. We will measure the pattern for the total energy, for the vertical and horizontal polarization components. The accepted CCR will have a FFDP with six spot positioned at a radius of 46 μrad (see fig. 4.30).
- the absolute value of the FFDP intensity, Ymax, Zmax, Fmax, in order to verify that the intensity to ground ILRS stations is correct.

4.5.1 Irradiation test of Tungsten and LARES retro-reflectors

The new LARES design consists of a full-tungsten body and the LAGEOS-type retro-reflectors with a larger dihedral angle offset, 1.5 ± 0.5 arcsec (instead of 1.25 ± 0.50 arcsec sued for LAGEOS).

A priori, the most severe source of potential radiation damage of LAGEOS and LARES comes from primary hadron showers originated by protons and nuclei from the Solar Wind (SW), the Van Allen Belts (VAB) and from Galactic Cosmic Rays (GCR). Another potential such source is secondary neutrons from the primary protons and nuclei showering on the outermost layers of the atmosphere. The spatial development of hadron showers is driven by the interaction length (λ_I), which describes statistically the exponential decay of the energy of the incident proton or nuclei.

In this section we discuss the potential effect of radiation on the laser-ranging performance of LARES, based on the operational experience of LAGEOS.

The operational experience with LAGEOS teaches us that no significant DIRECT radiation damage on its CCRs occurred in 30 years of intensive laser ranging. This is no surprise since the chosen material (Suprasil T19) was radiation resistant. The LAGEOS choice followed the choice of the Apollo Lunar CCRs, which are completely exposed to the SW (more than LAGEOS, which is shielded from the SW in part by the VABs). Suprasil T19 was not damaged by the SW+GSRs on the Moon; neither it did on LAGEOS, by a differently weighted combination of SW, VABs and GCRs. Therefore, there is not reason to worry about DIRECT radiation damage of the LARES CCRs. This is mainly due to the long λ_I (SiO_2) ~ 215 cm of fused quartz, compared to other materials with higher densities and larger Atomic Mass numbers.

LAGEOS also shows that INDIRECT radiation damage of the CCRs due to hadron showers on the external Aluminum hemispheres and on the inner Brass core is of no concern. This is natural for the aluminim given its relatively long λ_I(Al) ~ 39 cm. The brass core has a much shorter λ_I(Brass) ~ 15 cm, which is to be compared to the size of the inner core, ~ 35 x 25 cm^2. But even the hadron showers produced in the brass do not induce any damage on the LAGEOS CCRs.

The new LARES design has some differences compared to LAGEOS.

1. Unique λ_I(W) ~ 10 cm, compared to λ_I(Brass) ~ 15 cm. However, the difference is not very large.
2. CCRs are now surrounded by W and not by Al. Hadron showers develop very weekly inside Al and cause little secondary nuclear or hadron activity hitting the CCRs. With a good approximation, we can consider that the Aluminum is sort of transparent to showers.
    a. In LAGEOS the Brass core is a cylinder, it does not surround the CCRs.

b. In LARES the tungsten surrounds completely the CCRs (except for the front face). One of the new design options to decrease Surface/Mass, foresees conical cavities in place of the LAGEOS cylindrical cavities, increasing this difference with LAGEOS.

In order to test potential effects on the optical performance of the CCRs we will measure the FFDP of a reference CCRs mounted in their LARES tungsten cavity, before and after irradiation with nuclear and neutron beams equivalent to the expected energy released on LARES for an orbit time 10 years (at the VEGA altitude of h ~ 1200 Km and inclination i ~ 78^{o}). The nuclear beams will be provided by one of the INFN National Laboratories in Catania (LNS) or Legnaro (LNL). The candidate neutron irradiation facility is the ENEA Center "Casaccia" in Rome. For check and normalizations purposes, a second CCR will be tested in the same configuration, mounted in an Al cavity: in this case we must find a null result; it will be done to check that there is no fault in the experiment.

5 Conclusions and Future Work

This thesis is an experimental work for the LARES space mission, that was performed during a period of about one year at the experimental facilities of the Laboratori Nazionali di Frascati (LNF) of the Italian National Institute for Nuclear Physics (INFN). The work consisted of optical measurements at the LNF optical table, of participation in the design and setup of the optical circuit and of participation in the optical simulations done with the Code V software licensed to LNF.
The work on FFDP measurements, the calibrations of the laser intensity, the calibration of the three laser power-meters, the circuit alignment, the definition of the procedures for the angle offset calibration and for the calibration of the absolute FFDP intensity, are the original part of the thesis.
The FFDP circuit setup will be used for the important acceptance tests of LARES retro-reflectors. It will be also used to check the results of the tungsten irradiation tests to make sure that the new full-tungsten LARES design will NOT spoil the CCR optical performance, as expected.

5.1 Experimental Characterization at the INFN-LNF "Space Climatic Facility" (SCF)

INFN has built and started the operation of a Space Climatic Facility (SCF) for Near Earth Orbits at LNF 2006 [15]. Its initial purpose was to perform the full space-climatic, thermo-vacuum characterization of LAGEOS-type CCRs to study the asymmetric thermal thrusts (TTs) acting on LAGEOS due to the varying environmental conditions. The planned characterization has never been done before. It has become necessary because TTs are the most significant NGPs limiting Gravitation and Space Geodesy measurements done with LAGEOS and in the future also with LARES.
The laser ranging performance, including FFDPs, is affected by space climatic changes. The latter include transitions of the satellite between the Sun illumination and the Earth shadow (and vice versa). In order to perform integrated and concurrent space-climatic and laser-ranging tests on LARES and other LRR arrays, in 2007 the SCF has been significantly upgraded with laser test equipment and with optical analysis software capabilities [16].

5.2 The SCF Apparatus

A schematic view of the SCF is shown in Fig.5.1. The size of the steel cryostat is approximately 2 m length by 0.9 m diameter. The inner copper shield is painted with the Aeroglaze Z306 black paint (0.95 emissivity and low out-gassing properties) and is kept at T = 77 K with liquid nitrogen. When the SCF is cold, the vacuum is typically in the 10^{-6}-10^{-5} mbar range. The SCF includes both a Sun and Earth simulator. The Sun simulator (from www.ts-space.co.uk) provides a 40 cm diameter beam with close spectral match to the AM0 standard of 1 Sun in space (1366.1 W/m^2), with a uniformity better than ±5\% over an area of 35 cm diameter.

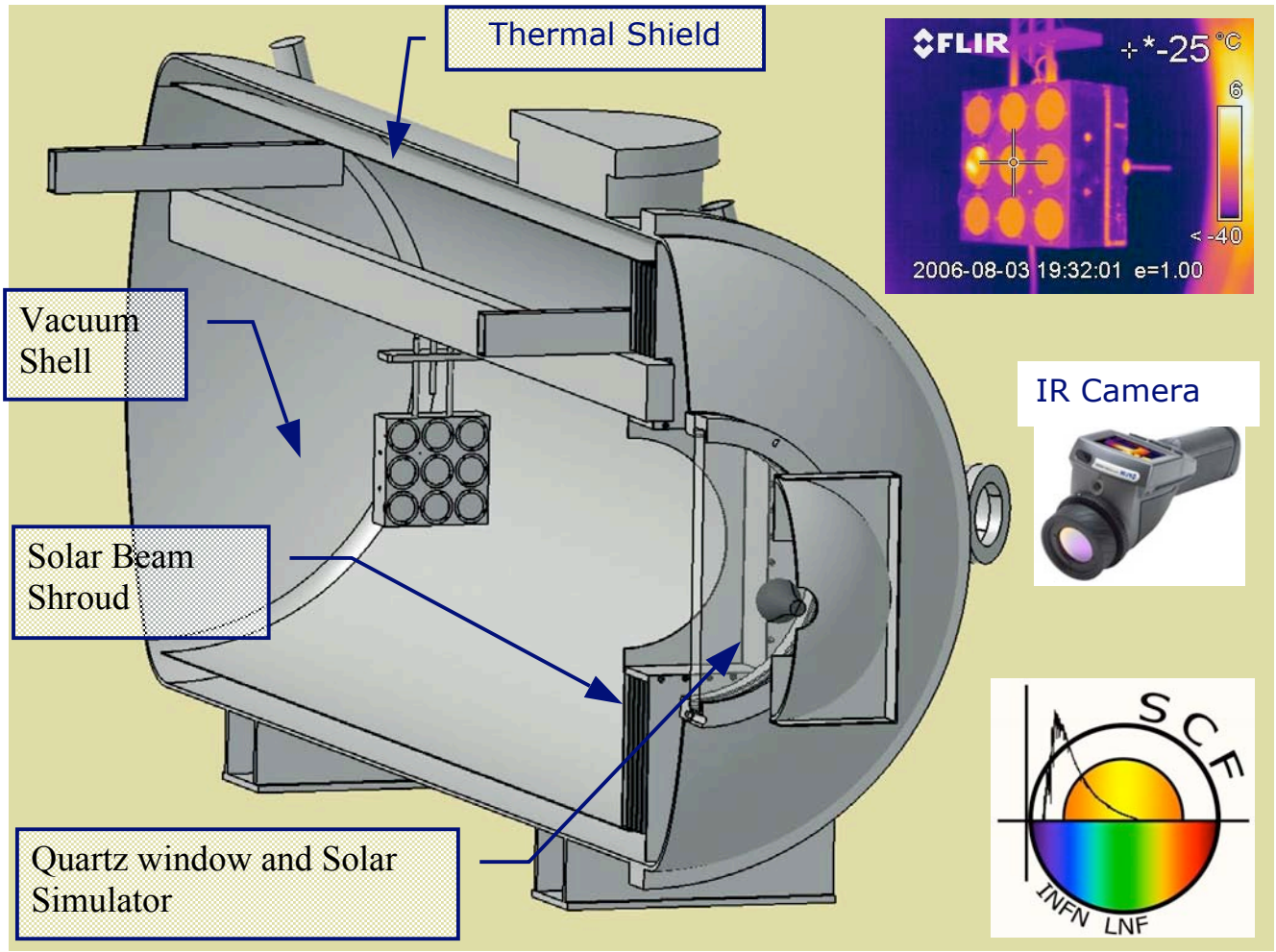

Figure 5.1. The SCF with the "matrix" 3x3 array of LAGEOS CCRs built at LNF. The top right inset figure is a temperature photo taken with the IR camera (shown in the right middle inset), through the side tunnel of the cryostat. Bottom right is the SCF logo.

The upgraded SCF is shown in fig. 5.4: the existing left Ge window for the IR camera, the new central window for FFDP measurements and the new right spare window. The Sun AM0 beam enters from the left through the quartz window. The specs of the central window are: fused silica material; 150 mm diameter, 36 mm thickness; deformations of the transmitted wavefront < λ/20, surface quality 10-5 scratch/dig, anti-reflective coating on both sides, reflectivity = 0.2% both for λ = 532 nm and 628 nm.

Each CCR will be first exposed to the Sun and Earth simulators and its thermogram taken. Then, the CCR will be rotated in front of the *central* window to take its FFPD. Fig.5.5 shows the "matrix" prototype viewed from the AM0 window and the FFDP windows.

The FFDP tests are currently done in STP conditions, but final tests will be performed with the CCR array in the SCF, both for LARES and other CCR prototypes. In other words, the FFDP circuit used for this thesis can be either moved to the optical table shown in fig. 5.3 or duplicated in order to perform measurements in parallel, as needed.

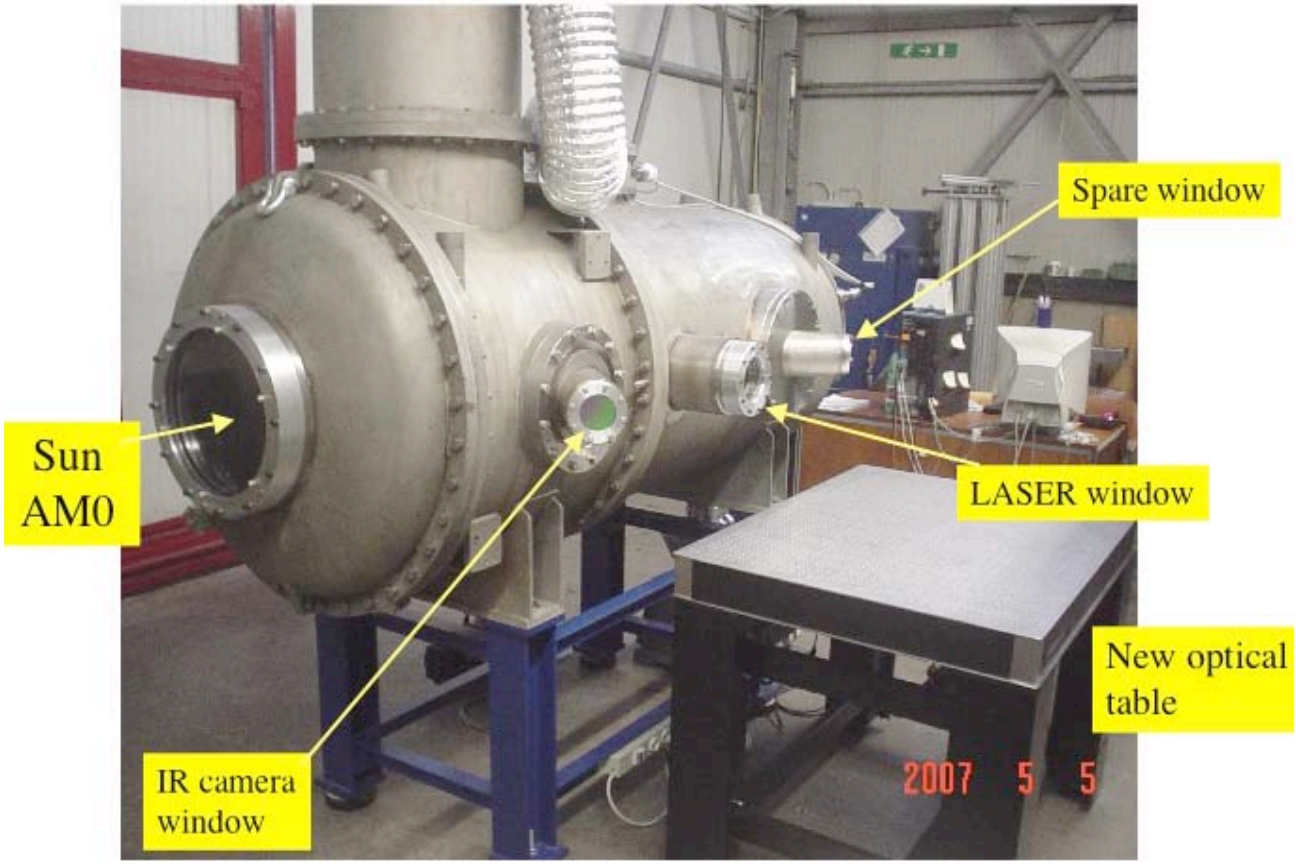

Figure 5.2 - The SCF upgraded for optical tests –

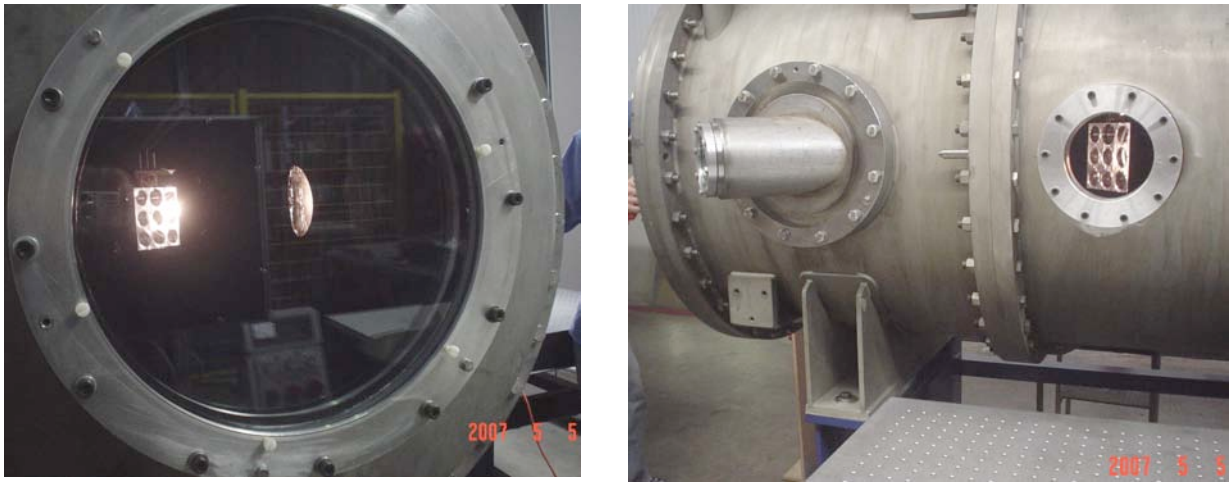

Figure 5.3 - LAGEOS matrix prototype viewed from the AMO and laser FFDP windows -

Figure 5.5 shows the mechanical system used rotate and tilt the LARES satellite inside the SCF to alternate between Sun illumination, thermography and laser measurements (FFDPs). The combination of rotation and tilt will allow for the measurement of the FFDO of each single CCR. The first measurements will be performed with the LNF matrix LAGEOS prototype. The maximum accepted radius (shown in fig. 5.5) for LARES is 220 mm. For the full-tungsten design of LARES, this maximum radius corresponds to a weight of ~750 Kg. This positioning system and the SCF itself can both stand the 220 mm maximal radius and the 750 Kg maximal weight.

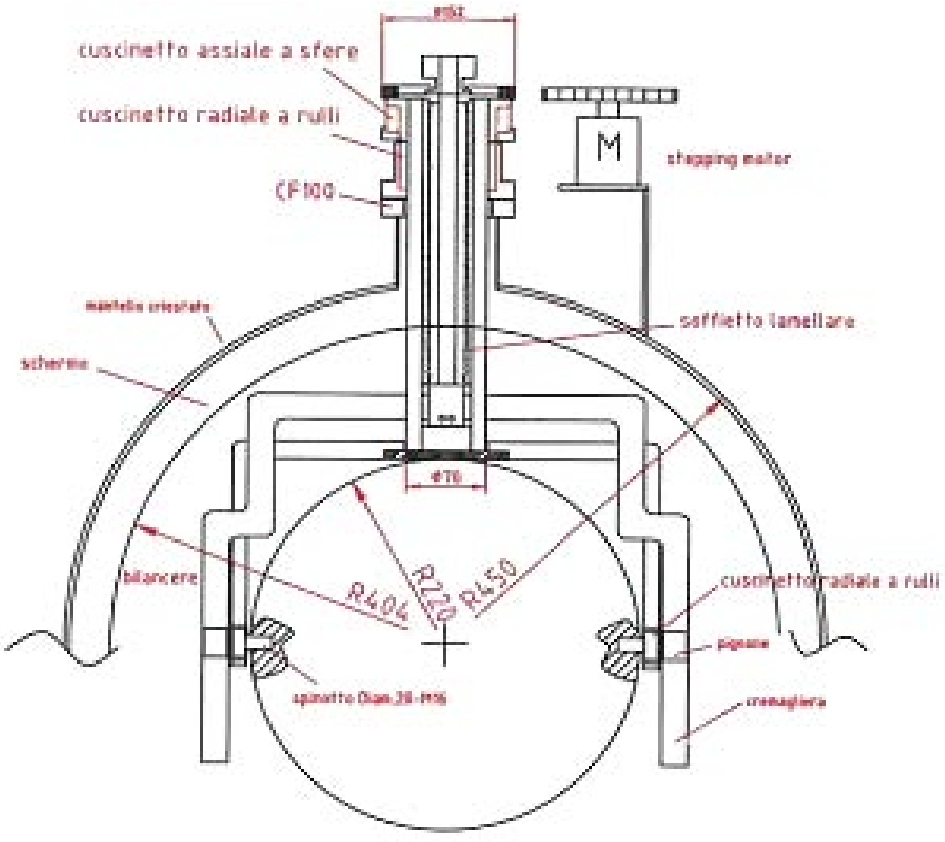

Figure 5.4 - Mechanical system to move (rotate and tilt) the LARES inside the SCF.

Acknowledgments

I wish to warmly thank:

D. Arnold (NASA-GSFC), for help with theoretical prediction of FFDP and velocity aberrations.

D. G. Currie (Univ. of Maryland), for advise on experimental work and optical calibrations

G. Giordano (INFN-LNF), for use of his optical table and numerous optical accessories.

M. Caponero, for use of his optical accessories.

A. Paolozzi (SIA) and S. Dell'Agnello (INFN-LNF), for supervising this thesis work.

I also enjoyed very much sharing the company and the work with M. Martini, A. Boni, N. Intaglietta, G. Bisogni , G. Delle Monache, S. Berardi, M. Garattini and C. Cantone, during an entire year spent at LNF.

References

1. I. Ciufolini, *Physical Rewiew Letters* 56, 278-281 (1986)
2. I. Ciufolini, E.C. Pavlis, F.Chieppa, E. Fernandes-Vieira, J.Perez-Mercader, *Science* 279, 27 March 1998
3. I. Ciufolini, E.C. Pavlis, *Nature* 431, 21 October 2004
4. I. Ciufolini, E.C. Pavlis, R. Peron *New Astronomy* 11, 572-550 (2006)
5. NASA *fact Gravity Probe-B*, Feb 2005
6. V.J. Slabinski *Cel. Mech. Dyn. Astr*. 66, 131-179 (1997)
7. *"Probing Gravity in Neo with High-Accuracy Laser-Ranging Test Masses", Internetional Journal fo Modern Physics,* 16 August 2006
8. Arnold D., *Cross section of the APOLLO Lunar retroreflectors arrays*
9. Arnold D., G. Appleby, "*Lageos' Asymmetric Reflectivity*", 14th International Laser Ranging Workshop, San Fernando, Spain, June 7-11, 2004.
10. Sette D., Bertolotti M., *Lezioni di F*isica [*Volume 2] Elettromagnetismo, Ottica*
11. *http://www.mocroscopy.fsu.edu/primer/anatomy/imageformationhome.html*
12. Minott, P., Zagwodzki, T., Varghese, T., Seldon, M., *"Prelaunch Optical Characterization of the Laser Geodynamic Satellite (LAGEOS 2)"*, NASA Technical Paper 3400, 1993.
13. Arnold D., private communication, *Range Correction*
14. Arnold D., private communication, *Reference mirror*
15. G. Bellettini *et al., LNF 2005 Annual Report*, 74-76 (2005)
16. *ETRUSCO: Extra Terrestial ranging to Unified Satellite Constellation*, LNF SIS Publication, March 2007